

The Pennsylvania State University
The Graduate School
Intercollege Program in Materials Science and Engineering

**SYNTHESIS AND CHARACTERIZATION OF HYBRID ELECTROLYTES WITH
TETHERED IONIC LIQUID FOR LITHIUM ION BATTERIES**

A Dissertation in
Materials Science and Engineering

by
Guang Yang

© 2018 Guang Yang

Submitted in Partial Fulfillment
of the Requirements
for the Degree of

Doctor of Philosophy

May 2018

The dissertation of Guang Yang was reviewed and approved* by the following:

Qing Wang
Professor of Materials Science and Engineering
Dissertation Advisor
Chair of Committee

Robert Hickey
Assistant Professor Materials Science and Engineering

Enrique Gomez
Associate Professor of Chemical Engineering

Jian Yang
Professor of Biomedical Engineering

Suzanne Mohny
Professor of Materials Science and Engineering and Electrical Engineering
Chair, Intercollege Graduate Degree Program in Materials Science and Engineering

*Signatures are on file in the Graduate School

ABSTRACT

Rechargeable lithium ion batteries are revolutionary energy storage systems widely used in portable electronic devices (e.g., mobile phones, laptops) and more recently electrical vehicles. The conventional liquid electrolytes in the lithium ion battery brought about safety problems such as fire and explosion. Related safety accidents (e.g., cell phone explosion, laptop fire, plane smoldering, etc.) have been reported many times. This also eliminates the possibility of using lithium metal as anode material which has much higher theoretical specific capacity in comparison with commercial graphite electrode because of the growth of uncontrolled lithium dendrites can lead to short circuit and other serious accidents. Solid polymer electrolytes have many advantages over conventional liquid electrolytes. They are light-weighted, non-volatile and have much better safety features than liquid electrolyte. Meanwhile, they are also better than the ceramic electrolyte in terms of their excellent flexibility and processability. Currently, low ionic conductivity of solid polymer electrolytes (e.g., polyethylene oxide (PEO)) at ambient temperature still hinders their practical application. Ionic liquids (ILs) are non-flammable and have negligible volatility. Its ionic conductive nature, excellent chemical stability, and good electrochemical stability enable them to be regarded as useful components for next generation battery electrolytes. In this thesis work, focus will be placed on synthesis and characterization of ionic liquid tethered organic/inorganic hybrid polymer electrolyte with high room temperature ionic conductivity. Moreover, their electrochemical properties and prototype battery performances were also looked into.

The use of highly conductive solid-state electrolytes to replace conventional liquid organic electrolytes enables radical improvements in reliability, safety and performance of lithium batteries. Here in chapter 2, we report the synthesis and characterization of a new class of nonflammable solid electrolytes based on the grafting of ionic liquids onto octa-silsesquioxane.

The electrolyte exhibits outstanding room-temperature ionic conductivity ($\sim 4.8 \times 10^{-4}$ S/cm), excellent electrochemical stability (up to 5 V relative to Li^+/Li) and high thermal stability. All-solid-state Li metal batteries using the prepared electrolyte membrane are successfully cycled with high coulombic efficiencies at ambient temperature. Good cycling stability of the electrolyte against lithium has been demonstrated. This work provides a new platform of solid polymer electrolyte for the application of room-temperature lithium batteries.

In chapter 3, an organic-inorganic hybrid solid electrolyte with ionic liquid moieties tethered onto dumbbell-shaped octasilsesquioxanes through oligo(ethylene glycol) spacers was synthesized. The hybrid electrolyte is featured by its high room-temperature ionic conductivity (1.2×10^{-4} S/cm at 20 °C with LiTFSI salt), excellent electrochemical stability (4.6 V vs Li^+/Li), and great thermal stability. Excellent capability of the hybrid electrolyte to mediate electrochemical deposition and dissolution of lithium has been demonstrated in the symmetrical lithium cells. No short circuit has been observed after more than 500 hrs in the polarization tests. Decent charge/discharge performance has been obtained in the prepared electrolyte based all-solid-state lithium battery cells at ambient temperature.

In chapter 4, hybrid polymer electrolyte network (XPOSS-IL) synthesized by crosslinking the individual dendritic POSS-IL was investigated. To be specific, after grafting mono-brominated hexaethylene glycol to the POSS cage, 1-vinyl imidazole was adopted for the subsequent quaternization reaction. Then the chain end double bonds underwent free radical crosslinking process to produce XPOSS-IL. The ionic conductivity of LiTFSI dissolved XPOSS-IL is 5.4×10^{-5} S/cm at 30 °C. By adding a small fraction of ionic liquid 1-ethyl-3-methylimidazolium bis(trifluoromethylsulfonyl)imide (EMITFSI), the ionic conductivity increases to 1.4×10^{-4} S/cm at room temperature. It is also found that EMITFSI will enhance the anodic stability of XPOSS-

IL. The Li/LTO and Li/LFP cell assembled with X-POSS-IL-LiTFSI/EMITFSI demonstrates capability of delivering high specific capacities at room temperature and elevated temperature.

TABLE OF CONTENTS

List of Figures.....	ix
List of Tables.....	xiv
List of Schemes.....	xv
List of Abbreviations.....	xvi
Acknowledgements.....	xviii
Chapter 1 Background and Introduction	1
1.1 General concepts of lithium ion batteries.....	1
1.1.1 Introduction of lithium ion battery.....	1
1.1.2 Electrochemical characterization methods	7
1.1.2.1 Impedance spectroscopy.....	7
1.1.2.2 Potential sweep method.....	9
1.2 Lithium ion battery electrolytes.....	9
1.3 Polymer Electrolyte.....	14
1.3.1 Gel polymer electrolytes.....	16
1.3.1.1 PEO based GPE.....	16
1.3.1.2 PVDF-HFP based GPE.....	17
1.3.2 Composite polymer electrolytes.....	18
1.3.3 Single ion polymer electrolytes.....	20
1.3.4 Solid polymer electrolytes	23
1.3.4.1 PEO-based SPEs	23
1.3.4.2 Non PEO-based SPEs.....	27
1.3.5 Ionic liquid based polymer electrolytes	29
1.3.5.1 Ionic liquids (ILs).....	29
1.3.5.2 Polymers/ILs electrolytes	30
1.3.5.3 Poly(IL)s.....	32
Chapter 2 Organic-Inorganic Hybrid Electrolytes from Ionic Liquid-Functionalized Octasilsesquioxane for Lithium Metal Batteries	36
2.1 Introduction.....	36
2.2 Experimental	38
2.2.1 Materials	38
2.2.2 Synthesis of 17-bromo-3,6,9,12,15-pentaoxaheptadecan-1-ol (2)	38
2.2.3 Synthesis of vinyl tris(17-bromo-3,6,9,12,15-pentaoxaheptadecan-1-ol silane (3)	39
2.2.4 Synthesis of POSS-IL (6)	39
2.2.5 Characterization Instrument.....	40
2.3 Result and discussion.....	44
2.3.1 Chemical synthesis and characterization	44
2.3.2 Thermal properties	50

2.3.3 Microstructure Characterization.....	50
2.3.4 Mechanical Properties.....	51
2.3.5 Ionic conductivity and electrochemical properties.....	52
2.3.5 Flammability test.....	70
2.4 Conclusion	71
Chapter 3 Dumbbell-Shaped Octasilsesquioxane Functionalized with Ionic Liquids as Hybrid Electrolytes for Lithium Metal Batteries	72
3.1 Introduction.....	72
3.2 Experimental	74
3.2.1 Materials.....	74
3.2.2 Synthesis of CPOSS	75
3.2.3 Synthesis of 17-bromo-3,6,9,12,15-pentaoxaheptadecan-1-ol	75
3.2.4 Synthesis of vinyl tris17-bromo-3,6,9,12,15-pentaoxaheptadecan-1-ol silane (1)	76
3.2.5 Synthesis of 2.....	76
3.2.6 Synthesis of CPOSS-PEO.....	77
3.2.7 Synthesis of CPOSS-IL	77
3.2.8 Characterization Methods.....	77
3.3 Result and discussion.....	80
3.3.1 Synthesis.....	80
3.3.2 Thermal properties	86
3.3.3 Microstructural Characterization	87
3.3.4 Ionic conductivity.....	88
3.3.5 Electrochemical properties.	89
3.3.6 Battery Performance.....	95
3.4 Conclusion	99
Chapter 4 Network of Ionic Liquid/Octasilsesquioxane Hybrid Electrolyte Plasticized by Ionic Liquid for Lithium Ion Batteries	100
4.1 Introduction.....	100
4.2 Experimental.....	102
4.2.1 Materials.....	102
4.2.2 Synthesis of 17-bromo-3,6,9,12,15-pentaoxaheptadecan-1-ol	103
4.2.3 Synthesis of vinyl tris (17-bromo-3,6,9,12,15-pentaoxaheptadecan-1-ol) silane (Vtris(PEO-Br)).....	103
4.2.4 Synthesis of 1-vinyl imidazole grafted POSS (POSS-Vim).....	104
4.2.5 Synthesis of X-POSS-IL and preparation electrolyte precursor solution	104
4.2.6 Characterization	105
4.3 Result and discussion.....	107
4.3.1 Synthesis.....	107
4.3.2 Thermal properties	109
4.3.3 Microstructural characterization	110
4.3.4 Ionic conductivity.....	111
4.3.5 Electrochemical properties	113
4.3.6 Battery Performance.....	115
4.4 Conclusion	118

Chapter 5 Summary and Suggestions for Future Work	119
5.1 Summary.....	119
5.2 Suggestion for future work.....	120
References	122

LIST OF FIGURES

Figure 1-1 Redox potential of electrode materials and electrochemical stability windows of aqueous electrolytes.	4
Figure 1-2 Schematic illustration of a common “rocking chair” lithium ion battery and the reactions on the cathode and anode.	5
Figure 1-3 Typical cell polarization curve.	6
Figure 1-4 Nyquist plot with impedance vector.	8
Figure 1-5 (a) potential sweep, (b) cyclic voltammogram.	9
Figure 1-6 (A) cyclic voltammetry of cathode (LiCoO ₂), anode (graphite), and electrolyte with Super P carbon as counter electrode in a lithium ion battery. (B) Potential operation range of LiCoO ₂ /C battery with common liquid carbonate electrolyte.	11
Figure 1-7 Ion transport in PEO.	15
Figure 1-8 (a) Mechanical properties of PVDF-HFP and Semi-IPN membrane. (b) The charge/discharge profile for the initial and 50 th cycle.	18
Figure 1-9 Ionic conductivity as a function of conducting phase ϕ_c	25
Figure 1-10 Chemical structure of POSS-PEG ₈ , POSS-benzyl ₇ Li ₃ and POSS-benzyl ₇ (BF ₃ Li).	27
Figure 1-11 Ionic conductivity-temperature relationship of SN-based solid electrolyte, PVA-CN/SN solid electrolyte, 1 M LiPF ₆ -EC/EMC/DMC liquid electrolyte, PVA-CN/SN solid electrolyte with commercial separator, SEN, and liquid electrolyte with commercial separator. Solid lines are VTF fitted curves.	28
Figure 1-12 Common cations and anions of ionic liquids.	30
Figure 1-13 Representative structures of poly(ILs).	33
Figure 1-14 Synthesis and preparation of PSiP/IL solid electrolyte.	35
Figure 2-1 Picture of POSS powder and compound 2 (left) and POSS-IL (right).	45
Figure 2-2 ¹ H NMR spectrum of POSS.	46
Figure 2-3 ¹ H NMR of compound 2.	47
Figure 2-4 ¹ H NMR spectrum of compound 3.	47
Figure 2-5 ¹ H NMR spectrum of POSS-IL.	47
Figure 2-6 FTIR spectra of POSS and POSS-IL.	48

Figure 2-7 X-ray photoelectron spectroscopy N 1s spectrum of POSS-IL.	49
Figure 2-8 X-ray photoelectron spectroscopy C 1s spectrum of POSS-IL.	49
Figure 2-9 DSC and TGA curves of POSS-IL and POSS-IL-LiTFSI.	50
Figure 2-10 XRD patterns of POSS-IL and POSS-PEO.	51
Figure 2-11 The dynamic shear moduli (G' , G'') and tan delta of POSS-IL as a function of applied strain at 25 °C.	52
Figure 2-12 Temperature dependence of ionic conductivity of POSS-IL-LiTFSI and POSS-PEO-LiTFSI.	54
Figure 2-13 Raman Spectra for TFSI ⁻ anion vibration of POSS-IL-LiTFSI at 25 °C in the range of 720-760 cm ⁻¹	55
Figure 2-14 Raman Spectra for TFSI ⁻ anion vibration of POSS-PEO-LiTFSI at 25 °C in the range of 720-760 cm ⁻¹	55
Figure 2-15 Raman spectra of TFSI ⁻ anion vibration of POSS-IL-LiTFSI (black), POSS-PEO-LiTFSI (red), and subtracting of POSS-PEO-LiTFSI from POSS-IL-LiTFSI (blue) at 25 °C in the range of 720-760 cm ⁻¹	56
Figure 2-16 FTIR spectra of POSS-IL-LiPF ₆ with different LiPF ₆ concentrations.	56
Figure 2-17 FTIR spectra of POSS-PEO-LiPF ₆ with different LiPF ₆ concentrations.	57
Figure 2-18 a) Nyquist plot of Li/POSS-IL-LiTFSI/Li symmetrical cell at different storage times. b) Evolution of R_{int} and R_b as a function of storage time.	58
Figure 2-19 Chronoamperometry profile of Li/POSS-IL-LiTFSI/Li cell and inset nyquist plot at 25 °C.	59
Figure 2-20 Linear sweep voltammetry of POSS-IL-LiTFSI (1 mV/s) at 25 °C.	60
Figure 2-21 Cyclic voltammetry profiles of Li/POSS-IL-LiTFSI/Li symmetrical cell (1 mV/s) at 25 °C.	60
Figure 2-22 Selected galvanostatic stripping/plating cycles of Li/Li symmetrical cells with POSS-IL-LiTFSI at a current density of 0.05 mA/cm ² . (each cycle includes 1 h stripping and 1 h plating).	61
Figure 2-23 Selected galvanostatic stripping/plating cycles of Li/Li symmetrical cells with 1 M LiTFSI in EC/DMC (1:1, v/v) at a current density of 0.05 mA/cm ² . (each cycle includes 1 h stripping and 1 h plating).	62

Figure 2-24 The surface morphology of the lithium foil after stripping/plating test characterized by SEM. Left) POSS-IL group after 440-h cycling. right) 1 M LiTFSI in EC/DMC (1:1, v/v) group after 40-h cycling.....	62
Figure 2-25 Galvanostatic polarization of Li/POSS-IL-LiTFSI/Li cells at current density of 0.05 mA/cm ²	63
Figure 2-26 Galvanostatic polarization of Li/1 M LiTFSI-EC/DMC/Li cells at current density of 0.05 mA/cm ²	63
Figure 2-27 Voltage vs Specific capacity profile of a galvanostatic charge-discharge cycling of Li/LTO cell at 0.1 C rate, 60 °C (17 mA/g).....	65
Figure 2-28 Cycling stability of Li/LTO cell at 0.1 C, 60 °C.....	66
Figure 2-29 Rate capability of Li/POSS-IL-LiTFSI/LTO cell at 60 °C (inset graph: charge/discharge curve at different rates).....	66
Figure 2-30 a) Typical voltage vs Specific Capacity profile of a galvanostatic charge-discharge cycling of Li/POSS-IL-LiTFSI/LTO cell at 0.1 C. b) Rate capability of Li/POSS-IL-LiTFSI/LTO cell. c) Cycling stability test of Li/POSS-IL-LiTFSI/LTO cell at 0.1 C. All tests were under 25 °C.....	67
Figure 2-31 Battery performance of Li/POSS-IL-LiTFSI/LiFePO ₄ cell at 25 °C. a) charge and discharge voltage profiles at 0.1 C. b) cycling stability at 0.1 C. c) rate capability test.....	69
Figure 2-32 Cycling stability test of Li/POSS-PEO-LiTFSI/LFP at 60 °C, 0.1 C.....	69
Figure 2-33 Flammability test of left) POSS-IL. right) 1 M LiTFSI in EC/DMC.....	71
Figure 3-1 ¹ H NMR of VPOSS-OH.....	81
Figure 3-2 ¹ H NMR of CPOSS.....	81
Figure 3-3 ¹³ C NMR of CPOSS.....	82
Figure 3-4 ¹ H NMR spectrum of 2.....	82
Figure 3-5 ¹³ C NMR spectrum of 2.....	83
Figure 3-6 ¹ H NMR spectrum of CPOSS-PEO.....	83
Figure 3-7 ¹ H NMR spectrum of CPOSS-IL.....	84
Figure 3-8 FTIR spectra of MDI, VPOSS-OH, and CPOSS.....	85
Figure 3-9 FTIR spectra of CPOSS-IL before and after ion exchange.....	85

Figure 3-10 DSC curve of CPOSS-IL-LiTFSI	86
Figure 3-11 TGA curve of CPOSS-IL-LiTFSI, HEG, and OVPOSS.....	87
Figure 3-12 XRD pattern of CPOSS-IL-LiTFSI	87
Figure 3-13 Ionic conductivity change with inverse temperature for CPOSS-IL-LiTFSI and CPOSS-PEO-LiTFSI	89
Figure 3-14 Cyclic voltammogram of CPOSS-IL-LiTFSI at 25 °C.	90
Figure 3-15 LSV curve of CPOSS-IL-LiTFSI at 25 °C.....	90
Figure 3-16 The Nyquist plots of Li symmetrical cell with CPOSS-IL-LiTFSI electrolyte at different storage time.....	91
Figure 3-17 The fitted resistance value of R_b and R_{int} as a function of time.	92
Figure 3-18 Chronoamperometry profile of Li/CPOSS-IL-LiTFSI/Li cell and inset nyquist plots at 25 °C.....	93
Figure 3-19 Selected galvanostatic stripping/plating cycles of Li/CPOSS-IL-LiTFSI/Li symmetrical cells with current density of a) 0.05 mA/cm ² , b) 0.075 mA/cm ² , and c) 0.1 mA/cm ² . each cycle includes 1 h stripping and 1 h plating. d) Li/1 M LiTFSI EC-DEC-DMC/Li cell at 0.075 mA/cm ²	95
Figure 3-20 Cycling stability test of Li/CPOSS-IL-LiTFSI/LFP cell at 0.1 C. All tests were done at 25 °C.....	95
Figure 3-21 Charge-discharge curves of Li/LFP cell assembled with CPOSS-IL-LiTFSI operating at 25 °C, 0.1C.....	96
Figure 3-22 Nyquist plot of Li/CPOSS-IL-LiTFSI/LFP cell after 1, 50, and 100 cycles at 0.1 C, 25 °C, measured at half discharge state.	96
Figure 3-23 Light-emitting diodes with different color could be lighted up be Li/CPOSS- IL-LiTFSI/Li cell at room temperature.....	98
Figure 4-1 ¹ H NMR of POSS-VIM.....	108
Figure 4-2 FTIR spectrum of X-POSS-IL.....	109
Figure 4-3 DSC curve of XPOSS-IL-LiTFSI.....	110
Figure 4-4 TGA curve of XPOSS-IL-LiTFSI	110
Figure 4-5 X-ray diffraction pattern of XPOSS-IL-LiTFSI	111

Figure 4-6 Comparison of ionic conductivity of XPOSS-IL, XPOSS-IL-LiTFSI, and XPOSS-IL-LiTFSI with different amount of added EMITFSI.	112
Figure 4-7 Photo image and schematic illustration of XPOSS-IL-LiTFSI/EMITFSI.	113
Figure 4-8 Chronoamperometry profile of Li/X-POSS-IL-LiTFSI/11/Li cell and inset nyquist plots before and after the polarization at 25°C.....	113
Figure 4-9 Anodic scan of XPOSS-IL-LiTFSI with different percentage of added ionic liquid.....	114
Figure 4-10 Cathodic scan of XPOSS-IL-LiTFSI with different percentage of added ionic liquid.....	115
Figure 4-11 Rate performance of Li/LTO cell running at 60°C, 0.1C.	116
Figure 4-12 Charge/discharge curve of Li/LFP cell assembled with XPOSS-IL/15 operating at 25 °C, 0.1C.....	117
Figure 4-13 Cycling stability of Li/LFP cell assembled with XPOSS-IL/11 operating at 25 °C, 0.1C.....	117
Figure 4-14 Nyquist plot of Li/XPOSS-IL/11/LFP cell after 15 and 30 cycles at 0.1 C, 25 °C, measured at half discharge state.	118

LIST OF TABLES

Table 1-1 Common electrical-circuit components and impedance expression.....	8
Table 1-2 Common Lithium salts and properties.	10
Table 2-1 Ionic conductivity values at room temperature and fitting parameters.	54
Table 2-2 Properties of solvent-free polymer electrolyte reported in literature.	69
Table 3-1 VTF parameters and ionic conductivity.	89
Table 4-1 Summary of X-POSS-IL/ionic liquid composition and ionic conductivity at 30 °C.	105

LIST OF SCHEMES

Scheme 2-1 Synthetic route of POSS-IL.....	45
Scheme 3-1 Synthetic route of CPOSS-IL.....	79
Scheme 4-1 Synthetic route of XPOSS-IL.....	107

LIST OF ABBREVIATIONS**Abbreviations**

AC	alternating current
C	graphite/carbon
CV	cyclic voltammetry
DEC	diethyl carbonate
DMC	dimethyl carbonate
DMF	dimethylformamide
DMSO	dimethyl sulfoxide
DSC	differential scanning calorimetry
EC	ethylene carbonate
EMI	1-ethyl-3-methyl imidazolium
HOMO	highest occupied molecular orbital
IL	ionic liquid
LFP	lithium ion phosphate
Li	lithium
LiAlCl ₄	lithium tetrachloroaluminate
LiAsF ₆	lithium hexafluoroarsenate
LiBF ₄	lithium tetrafluoroborate
LiClO ₄	lithium perchlorate
LiCoO ₂	lithium cobalt oxide
LiFePO ₄	lithium iron phosphate
LiMn ₂ O ₄	lithium manganese oxide
LiPF ₆	lithium hexafluorophosphate
LSV	linear sweep voltammetry
LiTf	lithium trifluoromethanesulfonate

LiTFSI	lithium bis(trifluoromethane sulfonyl)imide
LTO	lithium titanate
LUMO	lowest unoccupied molecular orbital
NMP	N-methyl-2-pyrrolidone
PC	propylene carbonate
PEG	polyethylene glycol
PEO	polyethylene oxide
POSS	polyhedral oligomeric silsesquioxane
PP	polypropylene
PVDF	polyvinylidene fluoride
SEI	solid electrolyte interphase
SPE	solid polymer electrolyte
VTF	Volger-Tamman-Fulcher

ACKNOWLEDGEMENTS

I would like to take this opportunity to express my deep gratitude to my thesis advisor, Professor Qing Wang for his unlimited support and encouragement for my graduate study. Dr. Wang not only taught me invaluable knowledge of materials science especially polymer science, but also gave me much freedom to explore and become a truly reliable, independent researcher. I also want to thank Dr. Wang for his help during my most difficult days in my graduate period. Without his support, I will not be able to come to this final stage of my Ph.D. degree. I want to thank Professors in my Ph.D. committee (Prof. Enrique Gomez, Prof. Jian Yang, and Prof. Robert Hickey) for their time and effort in participating my comprehensive exam and final oral defense as well as their insightful questions and suggestions in improving my dissertation quality.

I also want to acknowledge my group colleague Dr. Hyukkeun Oh, who was always ready to help me when I had no idea of lithium ion battery several years ago. I will thank my other wonderful group members Dr. Mathew Gardinski, Dr. Chalathorn Chanthad, Dr. Qi Li, Dr. Guangzu Zhang, Dr. Yang Liu, Baoyan Fan, Feihua Liu, Lixin Xing, Xiaoshan Zhang, Wuttichai Reainthippayasakakul, Ismail Alperen Ayhan, Yash Thakur and other groupmates for their help in my research work and graduate life. Outside the group, I will thank all my fellow MATSE friends and other friends who spent so much fun time with me at State College and I will never forget those colorful moments.

I am proud of being part of the MATSE Intercollege Graduate Program and I thank all the faculty members I met and all the staffs in the department.

I will thank Chiang Chen Industry Charity Foundation to financially support me for the first year of graduate study at Penn State University. I also thank Ms. Tammy Gibbons who did me a great favor in my early days at Penn State.

In the end, I will thank my parents who always unconditionally understand me and support me for the past 31 years. I also thank my cousins and other family members who are always there to support me.

Chapter 1

Background and Introduction

1.1 General concepts of lithium ion batteries

1.1.1 Introduction of lithium ion battery

Our current energy economy is still dominated by fossil fuels consumption and our demand for energy is constantly increasing. However, the fossil fuels resources are limited and non-renewable. Meanwhile, the emission of carbon dioxide leads to the rising of the temperature worldwide. This urges scientists to seek new clean, renewable, and efficient energy sources.

Batteries are electrochemical devices that are able to store and convert chemical energy to electrical energy. The energy conversion process is accompanied by oxidation and reduction reactions taking place at the electrodes. Cell is the basic electrochemical unit and a battery could be composed of more than one cell. Primary battery is non-rechargeable and secondary battery can be recharged after discharging and cycled for hundred or even thousand times. When the battery is discharging, the oxidation reaction happens at the anode and the reduction reaction happens at the cathode. The electrolyte mediates the ion transport within the cell. The electrons will travel through the external circuit from anode to cathode. When the battery is being charged, it could be regarded as an electrolytic cell. The electron flow and ions flow direction will reverse. The insulative separator preventing the two electrodes from contacting each other is permeable to ion species. The driving force for the battery to deliver electrical energy is the change of free energy ΔG° for the cell reaction. ΔG° is equal to total electrical work $-zFE^\circ$. (z is number of moles of electrons exchanged in the reaction, F is Faraday's constant, and E° is standard potential

difference). Under non-standard condition, $\Delta G = \Delta G^\circ + RT \ln Q$. R is the gas constant, T is the absolute temperature, Q is the reaction quotient. Substituting the $\Delta G = -zFE$ and $\Delta G^\circ = -zFE^\circ$. Equation $-zFE = -zFE^\circ + RT \ln Q$ is obtained. After both sides of the equation were divided by $-zF$, Nernst Equation was obtained as follows:

$$E = E^\circ - \frac{RT}{zF} \ln Q$$

Lithium was considered to be an excellent battery electrode candidate because it is the lightest metal (6.94 of atomic weight, 0.534 g/cm³ of density) and it has high electrochemical equivalence (3.86 Ah/g).^{1,2} Meanwhile, lithium has the lowest standard potential among metals (-3.05 V vs standard hydrogen electrode) allowing high cell voltage when combined with cathode. In 1970s, lithium primary battery was released to the market. Lithium ion battery (or lithium secondary battery, lithium rechargeable battery), are considered as a reliable rechargeable battery option since their appearance in market from Sony Corporation in 1991.^{3,4} These non-gaseous emission devices have already proved to be able to power portable electronic devices such as cell phones and cameras. In recent, lithium ion batteries are increasingly used in hybrid electric vehicles (HEV) and electric vehicles (EV) due to their high working voltage (at the order of 4 V) that is three times of rechargeable Ni-Cd batteries, no memory effect, reasonable energy density (100-150 Wh kg⁻¹) and cycle life (over 1000 times).⁵⁻⁷

For rechargeable lithium ion battery to work, the chemical reactions at both cathode and anode should be reversible. Intercalation compounds such as layered transition metal sulfide and transition metal oxides have been chosen as cathode material (e.g., TiS₂, lithium cobalt oxide (LiCoO₂), lithium manganese oxide (LiMn₂O₄), lithium ion phosphate (LiFePO₄, LFP), and lithium nickel manganese cobalt oxide (NMC)). In these cathode materials, the guest such as lithium can be inserted into their structures and then extracted out in the recharging process without changing the lattice structures of the host cathodes. The intercalation involves three steps:

1, Solvated Li^+ ions diffusion. 2, Li^+ ions desolvation and injection to vacancy. 3, Li^+ ions diffusion to host structure.⁸ LFP, with ordered olivine structure, is an attractive cathode material because: a, it has high capacity around $170 \text{ mA}\cdot\text{h/g}$ with excellent cycling stability; b, flat voltage plateaus indicate the two-phase insertion/disinsertion electrochemical process; c, the strong P-O bond in LFP greatly improves the battery safety because the probability of oxygen release was significantly suppressed. Its electronic conductivity need to be improved to facilitate higher charge/discharge rate.^{5,6} On the anode side, layered graphite carbon materials (graphite is able to hold large amounts of lithium, maximum $\text{Li}:\text{C}=1:6$, the theoretical capacity of LiC_6 is $372 \text{ mA}\cdot\text{h/g}$) that could intercalate lithium reversibly are mostly used for the electronic devices.⁴ Other intercalation anode materials include nitrides, phosphides, silicon based compounds, oxides (e.g. lithium titanium oxide, $\text{Li}_4\text{Ti}_5\text{O}_{12}$ (LTO)), and so on.⁹ LTO has theoretical capacity of $175 \text{ mA}\cdot\text{h/g}$ with lithium intercalation/disintercalation voltage of 1.55 V . Almost no volume change of LTO is detected during lithium insertion/disinsertion process. Its electronic conductivity (10^{-8} to $10^{-13} \text{ S}\cdot\text{cm}^{-1}$) needs to be enhanced to improve battery rate performance.¹⁰ LTO can be used as either anode or cathode. Figure 1-1 shows the redox potential of some electrode materials and also the electrochemical stability windows of aqueous electrolytes.

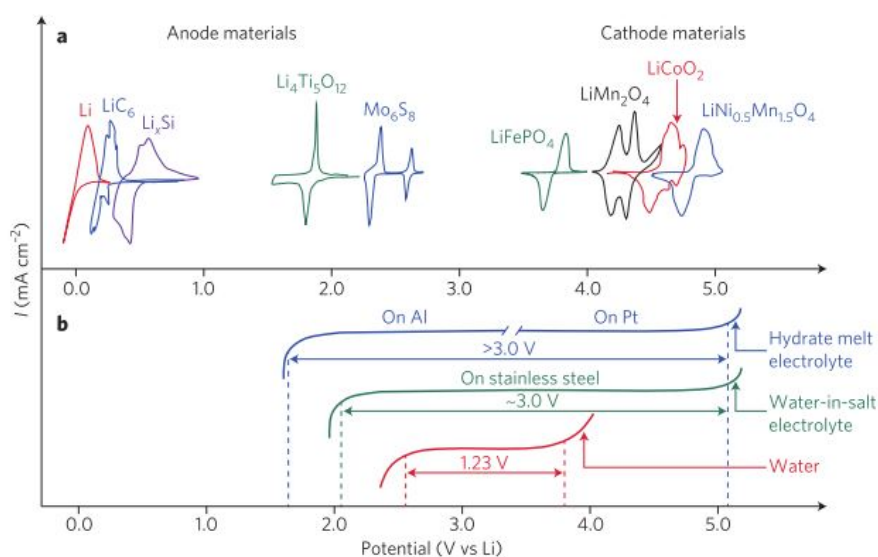


Figure 1-1 Redox potential of electrode materials and electrochemical stability windows of aqueous electrolytes.¹¹

Figure (1-2 c) represents typical configuration of a “rocking chair” type lithium ion battery in which the Li^+ ions are rocked back and forth between the LiCoO_2 cathode and graphite anode, the electrochemical reactions are also shown below. During the process of charging or discharging, the voltage of batteries can be simply described as $V = V_{oc} \pm IR_b$, where V_{oc} is open circuit voltage and R_b is internal resistance. R_b is contributed by several factors and can be written as $R_b = R_{el} + R_{in}(A) + R_{in}(C) + R_c(A) + R_c(C)$. R_{el} is the electrolyte resistance, $R_{in}(A)$ is the interfacial resistance at the anode side, $R_{in}(C)$ is the interfacial resistance at the cathode side, $R_c(A)$ and $R_c(C)$ are the resistances of current collectors at both sides, respectively.¹²

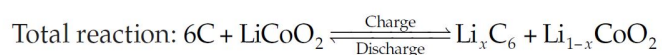
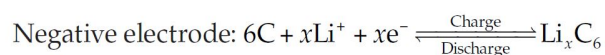
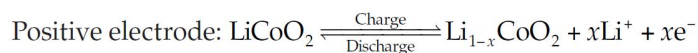
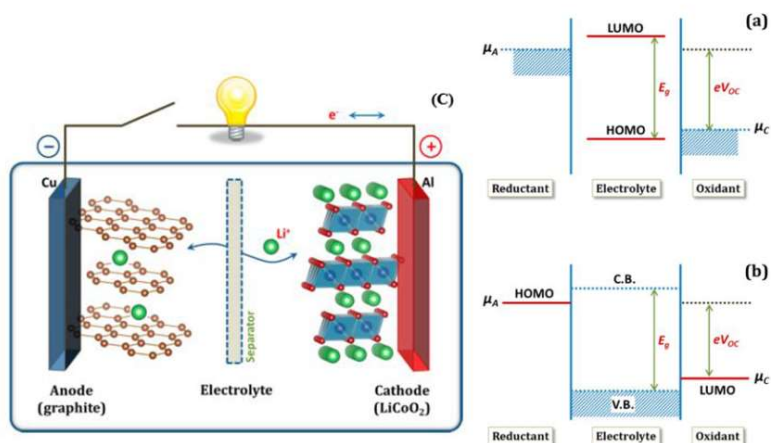


Figure 1-2 Schematic illustration of a common “rocking chair” lithium ion battery and the reactions on the cathode and anode.⁵

The difference of electrochemical potentials of anode and cathode and the energy gap in electrolyte are important parameters influencing electrode-electrolyte compatibility (Figure 1-2 a and b).^{12, 13} In general, the electrochemical potential of cathode, μ_A , and electrochemical potential of anode, μ_c , must lie within the HOMO (highest occupied molecular orbital)-LUMO (lowest unoccupied molecular orbital) energy gap (E_g) of liquid electrolyte or the energy gap between conduction band and valence band of solid electrolyte. In another words, the open-circuit voltage (V_{oc}) needs to be narrower than the electrolyte’s voltage window.

$$V_{oc} = (\mu_A - \mu_c) / e \leq E_g$$

If μ_A is above the LUMO of the electrolyte, the electrolyte will be reduced unless a passivation SEI layer is formed to block the electrode/electrolyte reaction. If μ_c is below the HOMO of the electrolyte, the electrolyte will be oxidized unless the SEI layer blocks the oxidation reaction.

The total energy stored in the electrode material could only be partially converted to useful electrical energy. Three main factors are affecting the performance or rate capability of the battery: a, activation polarization which leads to charge-transfer overpotential at the electrode. b, concentration polarization. c, the internal resistance of the battery. This will cause the voltage drop of the battery this IR drop is usually named ohmic polarization. The electrolyte resistance, the resistance of the electrodes, the current collector resistance, and the contact resistance between the electrode material and current collector are the main sources of internal resistance. The cell voltage after connecting to an external load is expressed as follows:

$$E = E_0 - [(\eta_{ct})_a + (\eta_c)_a] - [(\eta_{ct})_c + (\eta_c)_c] - iR_i$$

- E_0 is the open-circuit potential of the cell

- η_{ct} is charge transfer overpotential, η_c is the concentration polarization, a is anode, c is cathode
- R_i is the internal resistance
- i is the operating current

Figure 1-3 shows the relationship between the battery voltage and the applied current (polarization curve).

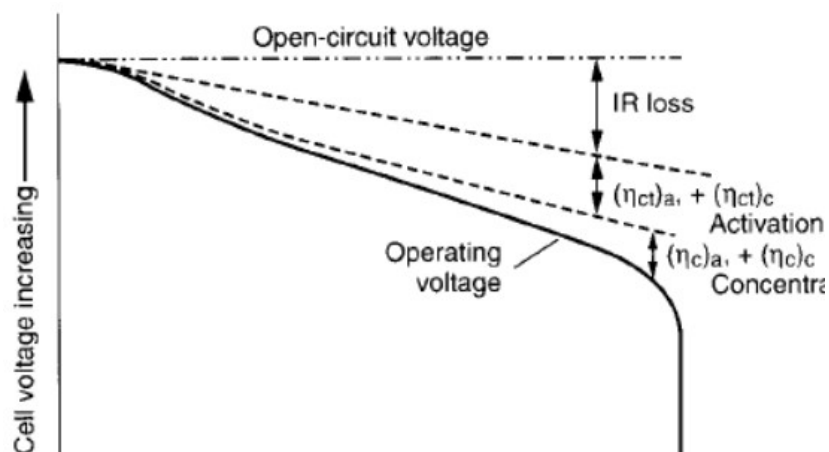


Figure 1-3 Typical cell polarization curve.⁸

Pure lithium metal has much higher specific capacity, but there are still many knotty issues before its commercialization in secondary batteries. For example, lithium can react with liquid electrolyte and the surface of the lithium will be passivated by lithium alkyl carbonate compounds. During the cycling process, uncontrolled, uneven deposition of lithium, in a mossy form, will decrease the amount of electroactive lithium. Meanwhile, lithium is also consumed during the cycling period because every time lithium is stripped or deposited, new lithium surface is exposed to the electrolyte. The worst situation is the growth of the uneven lithium deposition, also called

lithium dendrite, will penetrate the separator and touch the cathode causing the internal short circuit of the battery.¹⁴ The safety problems are the main reasons inhibiting the commercialization of lithium anode.^{15, 16} It should be mentioned that in 1980s, a small amount of rechargeable lithium batteries with lithium anode were produced and released to the market. Unfortunately however, they were withdrawn because of the safety problem. This is also the reason why the lithium ion batteries that dominated the market subsequently do not have metallic lithium anodes.

1.1.2 Electrochemical characterization methods

1.1.2.1 Impedance spectroscopy

Electrochemical Impedance Spectroscopy (EIS) is an important tool for the electrochemical analysis. It was first initiated in the 1880s by Oliver Heaviside. It can be used to study the dynamic properties of charge in the bulk or interfacial area in any type of liquid or solid material. Basically, a small sinusoidal voltage ($e=E \cdot \sin \omega t$, e is the potential at time t , E is the amplitude of the voltage signal, $\omega=2\pi f$ is the angular frequency, t is time) was applied on the electrochemical cell, the frequency f is varied (usually spanning from 0.01 Hz to 1 MHz), and the resulting current response which has a phase shift ($i=I \cdot \sin (\omega t+\varphi)$) is recorded and analyzed over the frequency range.¹⁷

According to Ohm's law, $Z=e/i= E \cdot \sin \omega t/I \cdot \sin (\omega t+\varphi)$. With Euler relationship, $\exp(j\varphi)=\cos\varphi+j\sin\varphi$, the potential can be expressed as $e=E \cdot \exp(j\omega t)$, $i=I \cdot \exp(j\omega t-\varphi)$. The complex form of impedance Z can be written as $Z(\omega)=E/I=Z_0 \exp(j\varphi)$ (j is imaginary unit), so $|Z| \exp(j\varphi)=|Z|(\cos\varphi+j\sin\varphi)$. This expression is composed of real part and imaginary part, $Z(\omega)=Z_{re}-jZ_{im}$. Plotting the real part on the X axis and negative imaginary part on the Y axis will produce Nyquist plot (Figure 1-4). The real and imaginary resistance provide information of kinetic, mass

transport, and capacitive properties of a cell.¹⁸ In lithium ion battery, EIS can provide resistance information of the bulk electrolyte, electrodes, the passive films, charge-transfer process, and diffusion process in electrolyte and electrodes.

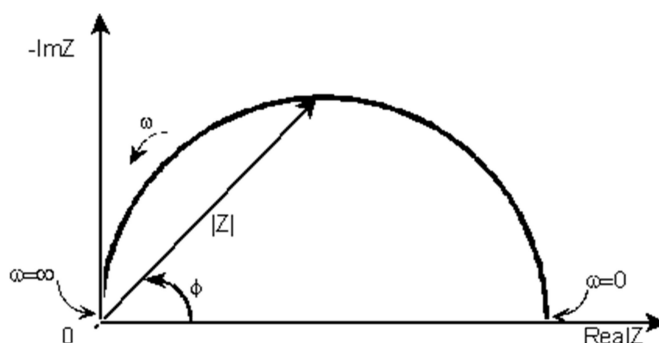


Figure 1-4 Nyquist plot with impedance vector.

The EIS data is usually fitted to an equivalent circuit model with resistors, capacitors, inductors, and other electrical elements. Some elements' current-voltage relationship and impedance expression are shown below. In reality, the rough nature of the surface, the material porosity, grain boundaries will end up with non-uniform distribution of the current and this will lead to the distribution of time constants. Constant phase element (CPE) is then introduced to replace the capacitor in order to support a more accurate fit to a depressed Nyquist semicircle. CPE can be denoted by $Z=A(j\omega)^{-\alpha}$, A is Warburg coefficient. When α is 1, CPE is like a capacitor; when α is 0, CPE is like a resistor; when α is -1, CPE is like an inductor; when α is 0.5, CPE is Warburg impedance related to ion diffusion. Table 1-1 shows electrical-circuit components and their impedance expression.

Table 1-1 Common electrical-circuit components and impedance expression.

Component	current vs. voltage	impedance
resistor	$E=IR$	$Z=R$
capacitor	$I=C \text{ d}E/\text{d}t$	$Z=1/j\omega C$
inductor	$E=L \text{ d}i/\text{d}t$	$Z=j\omega L$

1.1.2.2 Potential sweep method

Cyclic voltammetry (CV) is a popular electrochemical analysis technique. It can obtain useful information of electrochemical reactions such as locating the electroactive species' redox potentials. Basically, an applied potential on the working electrode is changed as a linear function of time and the direction will be reversed when certain potential is reached. The current response is then recorded (Figure 1-5). In linear sweep voltammetry (LSV), the potential is scanned from one value to the other and will not be reversed. The fixed magnitude of potential swept within per unit time is the scan rate.¹⁹ The peak current value is related to the scan rate and the peak position is related to the electrochemical reaction rate constant.

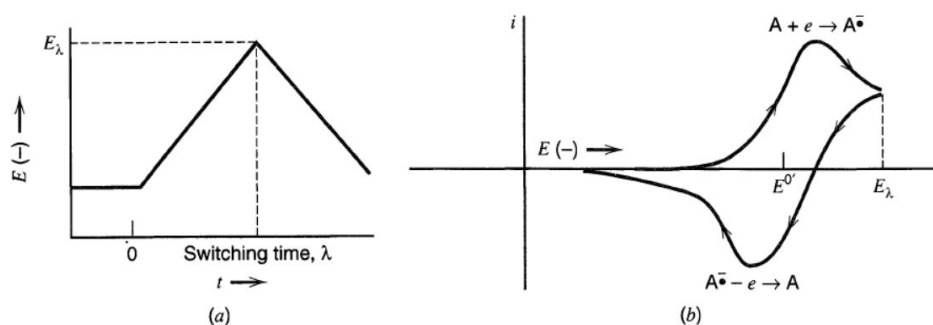


Figure 1-5 (a) potential sweep, (b) cyclic voltammogram.¹⁸

1.2 Lithium ion battery electrolytes

Currently, three main categories of electrolytes are in use or under research, liquid electrolyte, gel electrolyte and solid electrolyte. Almost all the commercialized lithium batteries used liquid organic molecules as the electrolyte because aqueous electrolyte has much narrower electrochemical stability window. Non-aqueous liquid electrolyte contains dissolved lithium salt (for example, LiClO_4 , LiPF_6 , LiBF_4 , LiAlCl_4 , LiAsF_6 , LiTf , LiTFSI) of certain concentration and organic solvent (such as ethylene carbonate (EC), dimethyl carbonate (DMC), diethyl carbonate

(DEC)). There are several requirements for electrolyte to be successfully applied to lithium batteries.

- The ionic conductivity should be high. The ionic conductivity is a reflection of how mobile the ionic species are for the electrochemical process. So high ionic conductivity ensures fast electrochemical reaction rate leading to high power. For liquid electrolytes, high dielectric permittivity solvents (e.g., ethylene carbonate) and low viscosity solvents (e.g., dimethyl carbonate, diethyl carbonate) are always mixed and the conductivity could reach 5-10 mS/cm at room temperature.^{9,20} With these electrolytes, the cell could work in the temperature range from -30 to 60 °C. The anions variation of lithium salts also influences the ionic conductivity of electrolyte. Table 1-2 lists some physical parameters of common lithium salts.

Table 1-2 Common Lithium salts and properties.¹³

Salt	Structure	M. Wt	$T_m / ^\circ\text{C}$	$T_{\text{decomp.}} / ^\circ\text{C}$ in solution	Al-corrosion	$\sigma / \text{mS cm}^{-1}$ (1.0 M, 25 °C)	
						in PC	in EC/DMC
LiBF ₄		93.9	293 (d)	> 100	N	3.4 ^a	4.9 ^c
LiPF ₆		151.9	200 (d)	~ 80 (EC/DMC)	N	5.8 ^a	10.7 ^d
LiAsF ₆		195.9	340	> 100	N	5.7 ^a	11.1 ^e
LiClO ₄		106.4	236	>100	N	5.6 ^a	8.4 ^d
Li Triflate	Li ⁺ CF ₃ SO ₃ ⁻	155.9	>300	>100	Y	1.7 ^a	
Li Imide	Li ⁺ [N(SO ₂ CF ₃) ₂] ⁻	286.9	234 ^b	>100	Y	5.1 ^a	9.0 ^e
Li Beti	Li ⁺ [N(SO ₂ CF ₂ CF ₃) ₂] ⁻				N		

- High lithium transference number (t_{Li^+}). t_{Li^+} is the fraction of the current carried by Li⁺ ions with respect to the total current. In lithium ion battery only Li⁺ ions contribute to the electrochemical reaction at the electrodes. Only the current carried by the Li⁺ ions is

considered to be useful during operation. Usually the electrolyte contains dissolved binary salt with mobile Li^+ cation and anion. The Li^+ cation is solvated by the solvent molecules and moves slower than the anion. The t_{Li^+} is usually less than 0.3 for traditional liquid electrolyte system. Low t_{Li^+} will lead to concentration effect increasing the battery internal resistance and reducing the available output power.²¹ Also, severe concentration polarization will lead to the formation of lithium dendrite on the electrode surface. The dendrite can penetrate the separator causing short circuit and more serious accidents.²²

- Good physical and chemical stability. The battery electrolyte should possess good thermal stability without any decomposition over wide temperature range especially under elevated temperature condition. Meanwhile, the electrolyte should be compatible with the electrode materials, binders, and current collectors without any drastic reaction.
- Good electrochemical stability. The electrolyte should have enough anodic and cathodic stability to form wide electrochemical stability window (up to 4.5 V) in order to avoid the oxidation decomposition or reduction of the electrolyte when the battery is operating. Also, wide electrochemical stability window enables high battery working voltage leading to higher power density.^{6,9}

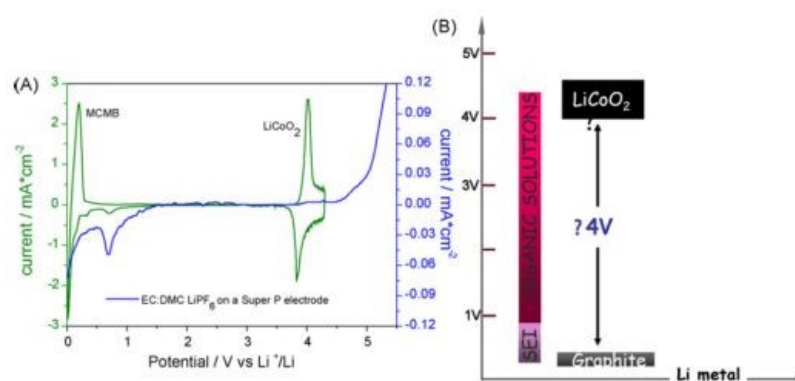
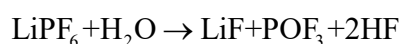


Figure 1-6 (A) cyclic voltammety of cathode (LiCoO_2), anode (graphite), and electrolyte with Super P carbon as counter electrode in a lithium ion battery. (B) Potential operation range of LiCoO_2/C battery with common liquid carbonate electrolyte.⁶

- Good safety and nontoxicity. The popular carbonate solvents are volatile and easy to catch fire with low flash points (for the linear carbonate solvents, flash point <math><30\text{ }^\circ\text{C}</math>).¹³ These factors pose serious safety problems towards scaling-up of the lithium ion batteries. A big challenge today is to formulate a nonflammable electrolyte that can compete with the common organic liquid electrolyte. Using flame retardant additives and polymer electrolytes are the two main alternatives.²³ The polymer electrolyte development will be discussed in detail in the following sections. Nontoxicity is another key parameter for battery materials because batteries are found everywhere in our daily life.
- The ability to form stable passivation layers. Solid electrolyte interphase (SEI) is formed irreversibly at the electrode/electrolyte interface during the first charging process of a cell which was assembled in a discharge state. SEI (The composition of SEI is highly dependent on the electrolyte and lithium salt used, it is usually composed of LiOH, LiF, Li₂CO₃, CH₃OLi, etc.) mainly comes from the reduction of the organic electrolyte because the low electrode potential is usually outside the stability window of the electrolyte causing the electrolyte decomposition.²⁴ The SEI layer is a passive, protecting layer covering the lithium or graphite electrode and inhibiting further dissolution of electrode materials into electrolyte. The formation of stable SEI layer that is electronically insulating but ion conducting (promoting Li⁺ transport with low impedance) is critical for maintaining high charge/discharge capacity.^{3,6} Uncontrolled growth of SEI will bring about problems such as cell capacity and cycling stability decaying.
- Inexpensive. Reducing the cost is always an important factor for the battery to be widely accepted by the public. In terms of battery safety, reducing the cost is also a challenge for alternative electrolyte such as synthetic polymers and ceramics to be commercialized.

For the future applications of lithium batteries in HEVs and EVs, scale-up is crucial. One of the major challenges for scaling up LIBs arises from safety issue. Most of commercial LIBs contain unsafe alkyl carbonate electrolytes composed of volatile and flammable liquid mixtures (e.g., EC, DMC, DEC, PC, EMC, etc.). Lithium salts are dissolved in these liquid electrolytes. Exposure to harsh conditions in terms of thermal and mechanical stress can lead to potential dangers in safety such as fire, electrolyte leakage, and explosion.^{6,25} For example, in case of metal lithium metal as the anode, short-circuits can occur by bridging the two electrodes originated from irregular lithium deposits. In practice, two safety incidents of Boeing 787 Dreamliner were reported in 2013 due to the smoldering of lithium ion batteries.²⁶ In order to address challenges in safety, solvent-free solid polymer electrolytes capable of dissolving the Li salts, dissociating into ions, and transporting Li⁺ ions have been studied.²⁷⁻³⁰ Also, lithium polymer batteries using gel polymer electrolytes are already used in mobile phones, laptop computers and other electronic devices. Some lithium salts that were broadly used in the past already showed their potential safety problems. For LiClO₄, it does not passivate well with Al current collectors and ClO₄⁻ is a strong oxidant that may cause explosion.³¹ Although LiPF₆ takes the largest portion in the lithium battery market because of its high conductivity and ability to form stable SEI with carbonate electrolytes, it is quite sensitive to high temperature and moisture.³² LiPF₆ starts to decompose into LiF and PF₅ at temperature over 80 °C.³³ PF₅ can increase the cell internal pressure. Moreover, the decomposed byproducts can also react with the liquid carbonate solvents to produce toxic compounds such as F(CH₂CH₂)O.³⁴

The hydrolysis of LiPF₆ is described according to the following equation:³⁵



After hydrolysis, the products include low ionic conductive LiF, and corrosive and acidic gas HF. Perfluoroalkyl sulfonic lithium salts such as lithium trifluoromethanesulfonate (LiTf), lithium-bis(fluorosulfonyl) amide (LiFSI), and lithium bis(trifluoromethanesulfonimide)

(LiTFSI), gain more and more attention due to their high ionic conductivity, good thermal and electrochemical stability, and much less sensitivity to H₂O.^{25, 36} The mostly studied LiTFSI (also named LiTFSA, LiNTf₂, LiTF₂N, etc.) has extensive delocalized negative charge because of the strong electronegative fluorine and resonance sulfonyl groups that result in weak association between anions and cations. The dissolution of LiTFSI in polymer electrolytes matrix will greatly increase the polymer amorphous region favoring ion conduction.³⁷

1.3 Polymer Electrolyte

Polymer electrolytes can be defined as any polymers with high ionic conductivity. They can be a system containing salt dissolved polymer matrix with or without plasticizer. They can also be single-ion polymer conductors. P.V. Wright initially discovered the capability of oxygen atoms on poly (ethylene oxide) (PEO) to form complex with alkali metal ions and the motion of cations is related to the dissociation and association among coordination sites in 1973 (Figure 1-7).^{38, 39} In 1978, Micheal Armand pointed out the possible application of PEO/Li salt complex as solid polymer electrolytes for batteries.⁹ After that, much interest was placed on the polyether/salt electrolyte systems. However, the PEO/lithium salt system had a limitation that the ionic conductivity, σ , was only satisfactory above a certain temperature (larger than 10⁻⁴ S/cm when T is higher than 60 °C) due to crystallization of PEO ($\sigma < 10^{-6}$ S/cm at room temperature, the ion conduction happens in the amorphous phase). The σ is highly correlated with polymer chain mobility. Higher chain mobility allows higher σ . However, the mechanical properties become poorer as the chain mobility increases. Therefore, balancing chain mobility in polymer electrolyte is important to achieve the optimum ionic conductivity and mechanical properties. To address the challenge, PEO based derivatives were developed including: a) block copolymers (BCPs) with PEO block providing the conducting pathway and the other block (e.g., polystyrene) improving

the total mechanical strength;⁴⁰ b) copolymers containing grafted PEO side chain;⁴¹ c) crosslinked polymer electrolyte containing PEO segment;⁴² d) star shaped or hyperbranched polymers.⁴³

Besides PEO, other polymer species that are commonly studied as lithium battery electrolytes components include: propylene oxide (PPO),⁴⁴ poly(methyl methacrylate) (PMMA),⁴⁵ poly(vinylidene fluoride-co-hexafluoropropylene) copolymer (PVDF-HFP),²⁹ polystyrene (PS),⁴⁶ poly(acrylonitrile) (PAN),⁴⁷ polyvinylchloride (PVC),⁴⁸ etc.. PPO also has coordination oxygen atoms but the spacing between the coordination atoms is different from PEO and is much weaker solvent for Li^+ ions. Other polymers are not ion conductive by themselves. They need to be associated with liquid electrolytes to promote the ion conduction.

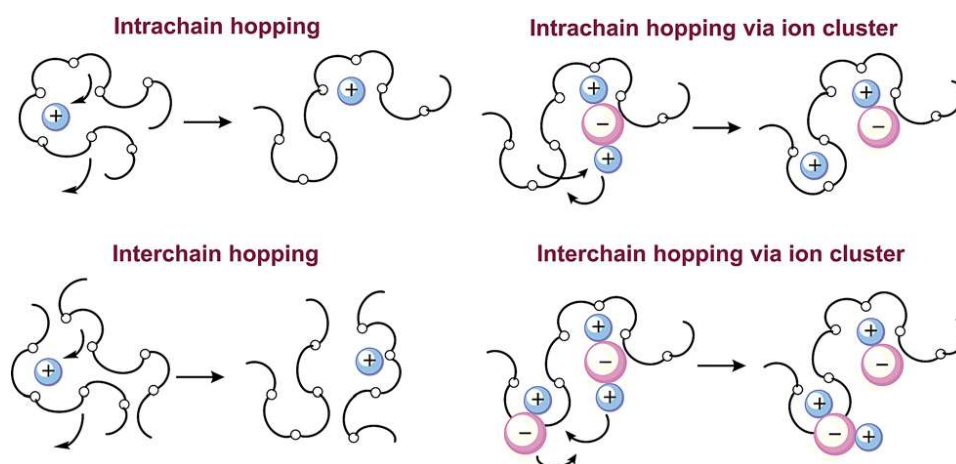


Figure 1-7 Ion transport in PEO.²⁵

As electrolytes of lithium batteries, polymer electrolytes are the ideal options because: 1) they are electronically insulating which is prerequisite for electrolytes in batteries; 2) they are soft materials which enable good contact with electrodes; 3) they can serve as separators; 4) they have good mechanical and electrochemical stability; 5) they enable to use high capacity lithium metal anodes ($3860 \text{ mA}\cdot\text{h/g}$) in the cells instead of traditional graphite electrode ($372 \text{ mA}\cdot\text{h/g}$) because they can mechanically suppress lithium dendrite formation and growth.^{27, 49, 50} The requirements for the polymer electrolytes are ensuring high σ , excellent chemical and electrochemical stability,

good compatibility with electrodes, facile processing, and sufficient mechanical properties.

Different approaches have been studied to meet the requirements such as gel polymer, polymer composite, single ion polymer, solid polymer electrolyte (SPE), and ionic liquid based polymer.

Following sections will describe these polymer electrolyte systems.

1.3.1 Gel polymer electrolytes

Gel polymer electrolytes (GPEs) are mostly formed by immobilizing liquid electrolyte into polymer matrix.⁵¹ They have the mechanical integrity of solid polymers as well as diffusion properties of liquid electrolytes. These materials enhance the safety of the LIBs because the liquid electrolytes related to leakage problem are trapped in the polymers.

1.3.1.1 PEO based GPE

The existence of PEO polymer chains in GPEs is important because PEO can promote the dissolution of Li^+ . Most of the time, PEO was incorporated to copolymer structures to disturb the PEO chain organization and reduce the crystallinity. Also, the introduction of rigid polymer structure such as polystyrene into the copolymer system enhanced the mechanical properties of PEO.⁵² As an example, poly(ethylene oxide)-co-poly(propylene oxide) (P(EO-co-PO)) copolymer electrolyte was incorporated into the matrix of commercial trilayer celgard[®] membrane.⁵³ This composite GPE could immobilize 1 M LiPF_6 EC/DMC/DEC solution as much as three times of the weight of the membrane. The σ of the composite GPE was 2.8×10^{-3} S/cm at room temperature. The battery test of the Li/GPE/ LiFePO_4 cell showed that the discharge capacity of 156 mA·h/g and 135 mA·h/g could be delivered at 0.1 and 1 C rate, respectively. Meanwhile, the composite GPE exhibited high Li^+ transference number (0.5) that could reduce the polarization effect during

charge/discharge process. In another study, copolymers consisting of benzyl methacrylate and oligo (ethylene glycol) methyl ether methacrylate were prepared and soaked in EC/DMC. It had excellent electrochemical stability comparable to liquid electrolyte (anodic limit above 6 V).⁵⁴

1.3.1.2 PVDF-HFP based GPE

PVDF-HFP is an attractive candidate of polymer electrolytes because this polar semi-crystalline polymer can satisfy both requirements in terms of high σ and mechanical properties. The amorphous HFP in the copolymer decreases the crystallinity. The VDF component is mainly responsible for providing the mechanical properties. From structural point of view, the strong electron withdrawing groups (-C-F-) render the PVDF-HFP high dielectric constant (9.4-10.6) so that it can dissociate lithium salt easier.^{55, 56} Zhang et al. fabricated a honeycomb-like porous PVDF-HFP gel polymer membrane. Its high porosity (78 %) allowed to absorb a large amount of liquid electrolyte (86.2 wt%). This membrane showed high σ as well as excellent electrochemical performance in coin cell type batteries.⁵⁷ On the other hand, it has been observed high liquid electrolyte uptake often leads to softness of the membrane, other polymers have been added to enhance the mechanical properties. For example, chemical crosslinking strategy was adopted to fabricate semi-interpenetrating network (semi-IPN) containing PVDF-HFP and crosslinked polyether.⁴² This GPE enhanced mechanical strength and toughness compared with pure PVDF-HFP membrane. Furthermore, after swelling in 1 M LiPF₆ EC/DMC solution, it exhibited high σ (1.49×10^{-3} S/cm) at room temperature and, in result, the excellent charge/discharge behavior of Li/LiFePO₄ cells (Figure 1-8). For other types of GPE using PVDF, microporous GPE membranes of PVDF/PMMA blends were prepared using phase separation technique.⁴⁵ It was found that introducing PMMA to PVDF decreased the crystallinity of PVDF, and increased porosity and electrolyte uptake of the GPE membrane. In galvanostatic cycling test, the

Li/LiFePO₄ cell incorporated with the GPE membrane exhibited almost 100% coulombic efficiency and the discharge capacity stabilized at 135 mA·h/g for at least 50 cycles.

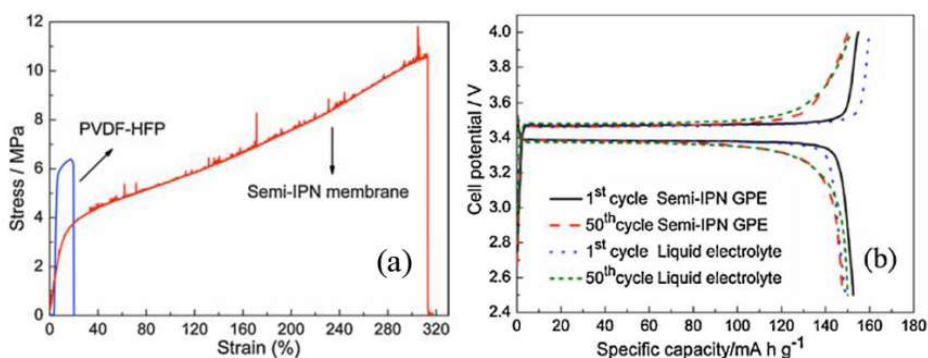


Figure 1-8 (a) Mechanical properties of PVDF-HFP and Semi-IPN membrane. (b) The charge/discharge profile for the initial and 50th cycle.⁴²

1.3.2 Composite polymer electrolytes

It has been discussed above that GPE gains the high σ at the cost of weakening the mechanical properties. In order to improve the mechanical strength with maintaining the σ as well as the electrode/electrolyte contact, polymer composites were utilized as electrolytes. Nano- or micron-sized inorganic fillers have been embedded into the bulk polymer electrolyte.^{58, 59 38, 60-62} The inert fillers (e.g. Al₂O₃, TiO₂, and SiO₂) are not involved in the Li⁺ transport process but they are able to suppress the polymer crystallization. The active fillers (e.g. Li₂N, LiAlO₂, Li_{1.3}Ti_{1.7}Al_{0.3}(PO₄)₃, and Li₇La₃Zr₂O₁₂) can participate in the Li⁺ conduction. In addition, the incorporation of inorganic components can enhance the cation transference number which is important for high power density of LIBs.^{59, 62}

At first, ceramic SiO₂ nanoparticles were introduced into polyacrylonitrile (PAN) film to improve mechanical properties. SiO₂ nanoparticles containing vinyl groups at surface as reactive

functionality were coated on the PAN fiber mat. Liquid carbonate electrolyte containing tri(ethylene glycol) diacrylate (TEGDA) as crosslinker was added into the PAN(SiO₂) composite membrane followed by crosslinking reaction. Compared with polyethylene and neat PAN fiber mat with similar thickness, the crosslinked PAN(SiO₂) exhibited obvious improvements in tensile strength and thermal stability. The graphite/PAN(SiO₂)/LiNi_{0.8}Co_{0.15}Al_{0.05}O₂ pouch cell delivered 190 mA·h/g after 200 cycles at 0.5 C at room temperature with 94.8 % of capacity retention which was superior to the discharging stability of batteries without crosslinked SiO₂.⁴⁷ Tu et al. reported PVDF-HFP/Al₂O₃ laminates with infused propylene carbonate (PC) to combine the mechanical strength of nanoporous Al₂O₃⁵⁸ and advantages in ion transport of PC. The porous γ -Al₂O₃ layer was sandwiched between two PVDF-HFP membranes. It was found that PVDF-HFP/Al₂O₃/PC with dissolved lithium bis(trifluoromethane)sulfonamide (LiTFSI) had not only high σ at room temperature (>1 mS/cm) but also low interfacial resistance which indicated fast transport of Li⁺ both in the bulk of electrolyte and at the electrolyte/electrode interface. Galvanostatic cycling test of Li symmetrical cell showed that the presence of Al₂O₃ impeded the Li dendrite proliferation. In another study, garnet type tetragonal Li₇La₃Zr₂O₁₂ (LLZO) was embedded in a PEO matrix. LLZO itself is known to have high σ (within the order of 10⁴ S/cm).⁶³ After it was introduced to PEO/LiClO₄ system, the optimal σ of 4.4×10⁻⁴ S/cm at 55 °C was achieved at 52.5 wt% of LLZO.⁶⁰

Using ceramic nanowire fillers is another option for polymer composite electrolyte. Nanowires were reported to provide uninterrupted Li⁺ conduction path that significantly decreased the interface junctions prevailing in particle reinforced systems.⁶⁴⁻⁶⁶ For example, Liu et al. prepared Li_{0.33}La_{0.557}TiO₃ (LLZO) nanowires utilizing electrospinning technique and embedded them into PAN matrix. σ value of 0.24 mS/cm could be achieved with addition of 15 wt% of LLZO nanowires into the PAN/LiClO₄ system. This was three orders of magnitude higher than that of PAN/LiClO₄ electrolyte. The reason was inferred that: a) the acidic groups of the

ceramic nanowires had high affinity with ClO_4^- favoring the dissociation of LiClO_4 ; b) the surface of LLZO nanowires contained a large number of vacancies allowing Li^+ hopping between vacant sites; c) the nanowires constructed three-dimensional conduction pathway promoting Li^+ movement.⁶⁵

1.3.3 Single ion polymer electrolytes

Conventional liquid or polymer electrolytes which prevail in prototype or commercial LIBs are conductors for binary Li-salt. Both Li^+ ions and counter ions are transported towards opposite direction in the electrolyte. Moreover, anions move much faster than cations, less than 1/3 of the current of the circuit comes from the cations. The lithium transference number (t_{Li^+}), the fraction of current from Li^+ ions to the total current for polymer electrolyte/binary salt system, is between 0.1 and 0.3.²⁵ Only Li^+ ions participate in the electrochemical reaction at the electrode/electrolyte interface, anions do not. Consequently, anions build up at one electrode interface and diminish at the other electrode interface which causes concentration polarization. Concentration polarization is a negative factor for battery performance. Concentration polarization decreases the overall σ , voltage, cycling rates, and power. It causes other undesirable reactions and lithium dendrite formation.^{22, 67} If the free movement of the anions can be hindered or eliminated, the concentration polarization effect can be avoided. That will allow a single-ion conductor (t_{Li^+} close to unity), in result cell power and stability will be improved accordingly. One of possible approaches is formation of covalent bonds between anions and polymer chains.^{68 69}

Various structures and combinations of polymers have been designed for single-ion polymer electrolytes.^{40, 68, 70-72} For example, single-ion conductors based on mixture of PEO and lithium poly(4-styrenesulfonyl(trifluoromethylsulfonyl)imide) (PSTFSI),⁷³ copolymers consisting of lithium (4-styrenesulfonyl)(trifluoromethanesulfonyl) imide (LiSTFSI) and methoxy-

polyethylene glycol acrylate (MPEGA) monomers,⁷⁴ AB diblock and BAB triblock copolymers where B block was P(STFSILi) and A block was PEO.^{40, 75} For the BAB triblock copolymer, Li was weakly associated with the TFSI anion in the B block enabling the fast cation transport. Meanwhile, the separation of the dissociable TFSI anion phase and the PEO phase indicated that the complexation conformation of Li⁺ was different from that of LiTFSI/PEO blend. The σ could reach 1.3×10^{-5} S/cm at 60 °C which was higher than the LiTFSI/PEO mixture. For the Li/BAB triblock copolymer/LFP battery, at C/2 rate, over 85% of the capacity could be retained and this was superior to other reported dry polymer batteries. This study provided hints for enhancing the σ of polymer electrolyte without sacrificing the mechanical properties. Sun et al. synthesized comb-branched single-ion polymer conductors based on copolymer of polyethylene glycol monomethyl ether acrylate and sulfonated polyethylene glycol acrylate with Li⁺ cation. The σ of dry polymer exhibited between 10^{-7} and 10^{-8} S/cm at room temperature. After imbibing 50 wt% of liquid carbonate electrolyte PC/EMC, the σ value increased to the order of 10^{-4} S/cm. In the galvanostatic cycling experiment, no concentration polarization effect occurred with current density of 0.1 mA/cm² at 85 °C.⁶⁸

Nafion membrane, which was originally designed as proton exchange membranes for fuel cells, was also modified to produce lithiated single-ion conductors due to its excellent chemical stability, mechanical strength, nanoporous structure, and insolubility in battery electrolyte solvents. Lu et al. studied the effect of lithated nafion film (Li-PEM) on the stability of lithium deposition on the electrode. They found the Li-PEM film showed high t_{Li^+} , facilitated uniform lithium stripping/plating, and impeded dendrite formation.⁷⁶

It is known that the commonly used LiPF₆ salt is not thermally stable (decompose above 60 °C) and can degrade in carbonate liquid electrolyte.^{25, 77} The byproducts after decomposition such as HF corrode the cathode materials. To replace LiPF₆, lithium chelatoborates such as lithium bis(oxalate) borate (LiBOB) and lithium bis[1,2-benzenediolato(2-)-O,O']borate (LBBB)

became attractive because of their excellent thermal and electrochemical stability, low cost, and capability of promoting solid electrolyte interphase (SEI) formation. These lithium borates have been either added to polymer electrolyte such as PVDF-HFP or chemically incorporated to polymer structures to make single-ion conductors. For example, low molecular weight polyborates such polymeric lithium pentaerythrite borate (PLPB) and polymeric lithium tartaric acid borate (PLTB) were added, as novel lithium salts, to polymer matrices such as PVDF-HFP.⁷⁸ Lithium polyvinyl alcohol oxalate borate (LiPVAOB) was synthesized via modification of the hydroxyl groups on PVA. Lithium oxalate polyacrylic acid borate (LiPAAOB) was obtained by modification of carboxyl groups of polyacrylic acid (scheme 1).^{69, 79}

Most of the single-ion polymer electrolytes mentioned above have relatively low glass transition temperature (T_g) due to PEO component with high chain flexibility. Although low T_g polymers are common selections for enhancing the room temperature σ (usually, the σ is still less than 10^{-5} S/cm for the dry polymer itself), their mechanical properties and thermal stabilities are partially sacrificed. Rigid aromatic structures were introduced to the main-chains of polymers to synthesis high T_g single-ion conductors. As an example, Oh et al. reported a single-ion poly(arylene ether)s with lithium perfluoroethyl sulfonates side chains (PAE-LiPFS) (Figure 6).⁷² This polymer was fabricated into microporous membrane (45 % porosity estimated from surface images by Scanning Electron Microscopy) which facilitated permeation of liquid electrolyte and charge transport. The dry PAE-LiPFS showed low σ of the order of 10^{-7} S/cm at room temperature. However, after soaking with DEC/EC/PC (1:1:1 by volume), σ increased dramatically to 3.1×10^{-3} S/cm. This was even superior to some liquid electrolyte containing polyolefin films. Negligible concentration polarization effect was confirmed by galvanostatic cycling test and the steady-state current method reported by Vincent and Bruce. The t_{Li^+} was close to unity (0.98) measured by the steady-state current method.⁸⁰

1.3.4 Solid polymer electrolytes

The ultimate goal for LPB is all solid-state battery whose electrolytes are free of volatile liquid components. Physically and chemically stable solid polymer electrolyte (SPE) with high ionic conductivity (σ), good electrochemical stability and compatibility with electrodes are perfect alternatives for organic liquid electrolyte.⁸¹ Non-flammable solid polymer electrolytes will not suffer from evaporation problems and can operate at high temperatures. The ion transport of Li^+ in the polymer matrix mainly results from either ion hopping on polymer chains or polymer segmental movement.⁴⁹ Currently, although some interesting works have been done to produce SPEs with decent σ and good mechanical strength, most of the reported SPEs still suffer from relatively low σ due to low ion mobility caused by crystallization of polymers.^{25, 49, 82, 83} High operation temperature is usually required to achieve good σ and sufficient interfacial contact.

1.3.4.1 PEO-based SPEs

The merits of PEO as solid polymer electrolytes have been well recognized.^{84, 85} Currently, researchers are putting great efforts to improve the low σ at room temperature and poor mechanical properties of PEO, such as blends with amorphous polymers and additives, grafting oligomeric PEO to the polymer backbones, block copolymers with rigid and soft blocks to integrate high mechanical strength and free conduction pathway at the same time, crosslinking chemistry to prepare polymer networks, and addition of inorganic fillers to enhance Li^+ transport, mechanical properties, transference number as well as anodic stability.^{86 82, 85, 87, 88}

BCPs can be an attractive option for SPEs because BCPs provide a flexible design in chemical structures and enable the formation of conductive channels for ions by self-assembly. Usually, one block is PEO to solvate the Li^+ dissociated from salt and the other block is polymer

containing stiff backbones with high T_g such as PS. The PEO block can be both linear or comb shaped. The σ is influenced by the block composition, the molecular weight of each block of BCPs, and the concentration of the salt.⁸⁹ Balsara group investigated the effect of PEO chain lengths on the σ of diblock copolymers. They found that an increase of PEO chain length led to a decrease of σ at the beginning, and gradually the σ stabilized (the largest σ at 60 °C could reach 2×10^{-4} S/cm when the ratio of ethylene glycol unit to Li^+ was 11).⁹⁰ This phenomenon was different from that of PEO homopolymer whose σ decreased when molecular weight rose. The authors explained that the proportion of dead zone (non-effective zone for conduction) at the PEO/PS interface increased when the PEO molecular weight decreased.⁹¹ The σ as a function of volume fraction of PEO (Φ_c) phase is shown in Figure 1-9. When Φ_c was high, $\log [\sigma]$ has linear relationship with Φ_c . When the salt concentration was high, the σ dropped rapidly because the formation of ion aggregates slowed down the mobility of ions. Also, the increase of Φ_c raised the melting point (T_m) and degree of crystallinity (X_c) of the linear BCPs. On the other hand, by increasing the fraction of PS, both linear and comb shaped BCPs exhibited enhanced mechanical properties (tensile strength and Young's modulus). When applied to lithium metal batteries using porous LFP cathode, linear BCPs seemed to be better than comb BCPs in terms of the cycling stability at low rates, but comb BCPs are more promising for room temperature application.⁸⁹

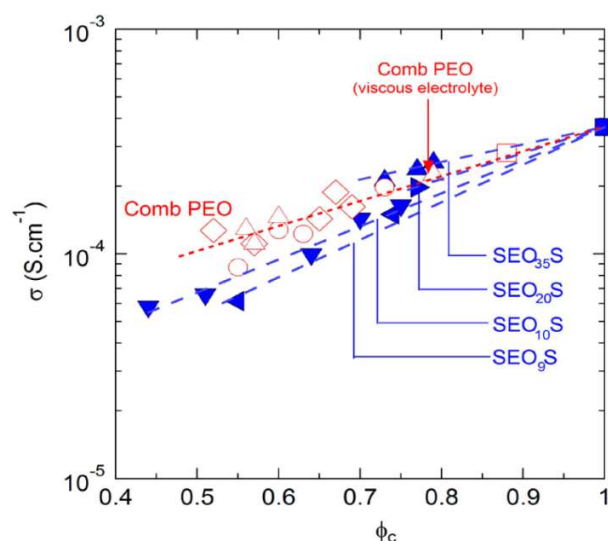


Figure 1-9 Ionic conductivity as a function of conducting phase ϕ_c .⁹¹

Besides the PEO based BCPs SPEs, strategies such as making polymer networks,⁷ adding plasticizers, ceramic fillers,^{41, 84, 88, 92} and other inorganic moieties are also adopted and tested.^{93, 94} It is known that lithium dendrite formation on lithium anodes of lithium metal battery will do harm to the battery life because these uneven deposited lithium dendrites could pierce through the electrolyte and bridge cathode and anode causing short circuit.^{66, 95} The Chazalviel model proved that low τ_{Li^+} in the electrolyte could accelerate the growth of dendrites.⁹⁶ Monroe proposed that improving the shear modulus above 7 GPa could significantly suppress dendrites.⁹⁷ Khurana et al. reported a method to synthesize crosslinked polyethylene (PE) using PEO-based crosslinker (PEOX). Although these PE-PEO crosslinked polymers could not show increased σ compared to other amorphous PEO-based polymers, it gave better mechanical strength and electrochemical stability. In order to meet the minimum requirement for room temperature application of batteries, σ has to be more than 1×10^{-4} S/cm. When poly(ethylene glycol) dimethyl ether (PEG) ($M_w=275$ g/mol) incorporated to the PE-PEO as plasticizer, σ further increased to 2×10^{-4} S/cm. Galvanostatic strip/plate experiments were carried out to study how the plasticized PE-PEO

perform to resist dendrite induced short-circuit. It was found that the PE-PEO/PEG polymer exhibited more than one order of magnitude higher of the charge passed before cell short circuit (C_d , 1790 C/cm² for (⁷⁰PEOX_{0.34})(³⁴PE_{0.35})(⁵PEG_{0.31}) under current density of 0.26 mA/cm² at 90 °C) than that of PEO ($M_n=900$ KDa) and PS-*b*-PEO BCPs. Nanohybrid polymer electrolytes based on PEO and lithium [(4-methylphenyl)sulfonyl][(trifluoromethyl)sulfonyl]amide anion co-grafted Al₂O₃ and SiO₂ nanoparticles were reported by Lago et al.⁸⁸ σ of 1.9×10^{-4} S/cm was found at 70 °C. The LFP/Li coin cells using above mentioned electrolyte could still deliver 120 mA·h/g after 130 cycles at C/2 rate, 70 °C.

Polyhedral oligomeric silsesquioxane (POSS) is composed of a thermally stable rigid inorganic SiO_{1.5} silicon-oxygen framework and eight attached organic groups. That can be adopted as filler to improve the mechanical properties of polymers.^{43, 98, 99} POSS as filler can form dendritic-like structure providing additional free volume, which allows to decrease glass transition temperature (T_g) of polymers and thus enhances the ion conduction.⁹⁹ Wunder group investigated eight PEO chains grafted POSS type Li⁺ ion conductors.^{43, 100-103} They found that the σ at room temperature of Octa PEO (4 ethylene oxide repeating units/chain) functionalized POSS could reach 10⁻⁴ S/cm level ($M_w=3000-5000$, LiClO₄ as salt), which was comparable to low molecular weight PEOs ($M_w=300-500$).¹⁰⁰ In another work, hybrid SPE composed of octa PEO functionalized POSS (POSS-PEG₈) and phenyl groups/-Si-O-BF₃Li ionic groups co-functionalized POSS (POSS-benzyl₇(BF₃Li)₃) was prepared (Figure 1-10). Due to the electron withdrawing POSS molecules and BF₃ anions, Li⁺ dissociation was improved.⁹⁴ The phenyl functional groups could crystallize which provided structural support. The Li⁺ ions of -Si-O-BF₃Li groups were solvated by the conduction phase POSS-PEG₈. Consequently, the σ at 30 °C was 2.5×10^{-4} S/cm when the O/Li ratio was 16/1. In addition, since the POSS-benzyl₇(BF₃)₃⁻³ anion was bulky, larger portion of the current could be carried by the Li⁺ ions. The t_{Li^+} was 0.5 ± 0.01 indicating slowing down of anion movement.

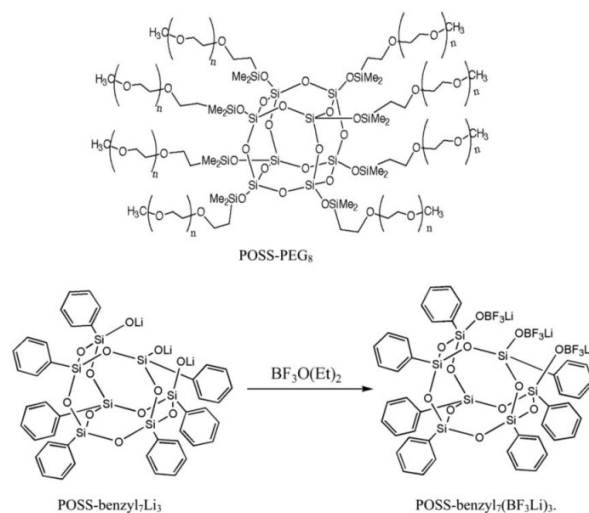


Figure 1-10 Chemical structure of POSS-PEG₈, POSS-benzyl₇Li₃ and POSS-benzyl₇(BF₃Li).³

1.3.4.2 Non PEO-based SPEs

Other than PEO, different polymers and additives (e.g. poly(propylene carbonate), PVA, succinonitrile, perfluoropolyether, etc.) have been tried in SPE.¹⁰⁴⁻¹⁰⁸ Nitrile compounds such as succinonitrile (SN) were proved to increase σ for SPE because the high polarity of $-C\equiv N$ group in SN enabled the solvation of salts.^{104, 109, 110} When mixed with Li salts, SN is viscous liquid rather than solid at room temperature. By the reason, SN was mixed with mechanically stronger polymers. Cyanoethyl PVA was synthesized in the SN/LiTFSI solution which was prefilled in the PAN fiber mat with 17 μm thickness (named SEN).¹¹⁰ The mechanical strength of SEN was 15.4 MPa which was higher than that of a PAN fiber mat. CV test showed that SEN was electrochemically stable up to 5 V. The σ at room temperature of SEN was 4.49×10^{-4} S/cm. The $\log \sigma$ -T relationship is presented in Figure 1-11. The curve could be well-fitted by empirical Vogel–Tammann–Fulcher equation shown in Equation 1.

$$\sigma(T) = \frac{A}{\sqrt{T}} \exp\left(\frac{-B}{R(T-T_0)}\right) \quad \text{Equation 1}$$

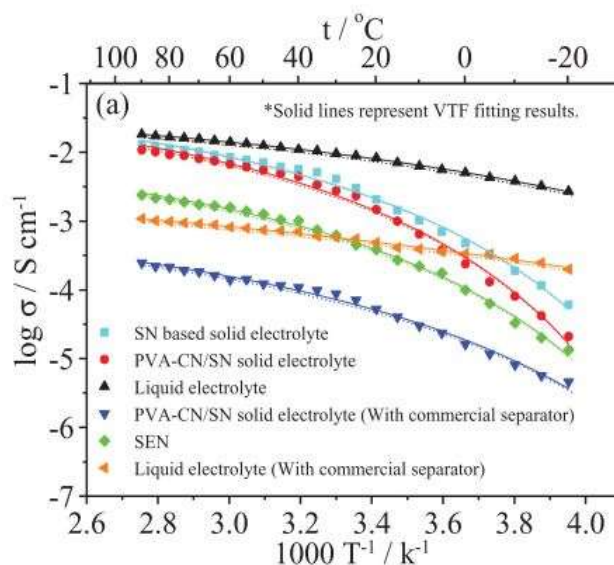


Figure 1-11 Ionic conductivity-temperature relationship of SN-based solid electrolyte, PVA-CN/SN solid electrolyte, 1 M LiPF₆-EC/EMC/DMC liquid electrolyte, PVA-CN/SN solid electrolyte with commercial separator, SEN, and liquid electrolyte with commercial separator. Solid lines are VTF fitted curves.

A is the pre-exponential factor representing the number of charge carriers, B is the pseudo activation energy for ion motion, T_0 is the ideal glass transition temperature at which the free volume disappears, and R is the gas constant. The B value obtained by fitting was 4.25×10^{-2} eV which was close to the activation energy of liquid electrolyte. The LFP/SEN/Li battery could delivery 97.7 mA·h/g at 1 C rate. Wong et al. reported a new perfluoropolyether-based electrolyte (PFPE-DMC) using commercial celgard membrane as physical separator.¹⁰⁶ They found that PFPE-DMC was able to solvate LiTFSI and promote the Li⁺ conduction with σ of 2.5×10^{-5} at 30 °C. The t_{Li^+} was close to unity (0.91). Poly(propylene carbonate)-based SPE in combination with cellulose nonwovens supports (CPPC-SPE) was also reported.¹⁰⁷ At 20 °C, the σ reached 3×10^{-4} S/cm which was 2 orders of magnitude higher than that of PEO-SPE counterparts. The

discharge capacity of LFP/CPPC-SPE/Li cell at 20 °C and 0.1 C was 142 mA·h/g. Moreover, the cell demonstrated excellent cycling stability. Only 5% of capacity loss was found after 1000 cycles at 20 °C and 0.5 C. When used in higher voltage LIBs with $\text{LiFe}_{0.2}\text{Mn}_{0.8}\text{PO}_4$ as the cathode, flat charge and discharge curves were observed around 4.1 V and 96% of capacity was retained after 100 cycles. These non-PEO based SPEs greatly enriched the exploration for safe LIBs electrolytes. Table 1 lists properties and performance in LIB of representative SPEs.

1.3.5 Ionic liquid based polymer electrolytes

1.3.5.1 Ionic liquids (ILs)

Ionic liquids (ILs) are molten organic at room temperature. They have been considered important in electrochemical devices especially as potential electrolyte candidates for LIBs because of their unique properties: ionic conductive ($\sigma=10^{-4}$ to 10^{-2} S/cm), non-volatile, non-flammable, and electrochemically stable (generally > 4 V).¹¹¹⁻¹¹³ The cations of ILs include 1, 3-dialkyl imidazolium, N-alkyl pyridinium, tetraalkyl ammonium, tetraalkyl phosphonium, and N-alkyl pyrrolidinium. The anions of ILs can be bis((trifluoromethyl) sulfonyl)imide (TFSI⁻), tetrafluoroborate (BF_4^-), hexafluorophosphate (PF_6^-), trifluoromethane sulfonate (Tf^-), chloride (Cl^-), bromide (Br^-), nitrite (NO_2^-), iodide (I^-), acetate (CH_3CO_2^-), etc. (Figure 1-12).

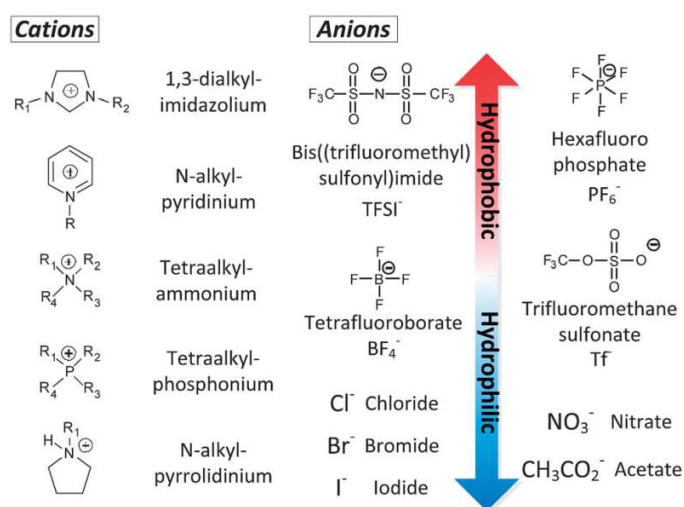


Figure 1-12 Common cations and anions of ionic liquids.¹¹¹

1.3.5.2 Polymers/ILs electrolytes

The introduction of ILs into polymer electrolyte system is one of the effective ways for enhancing the σ because the plasticizing ILs can provide more “free volume” in the polymers for ion diffusion.^{29, 114-116} ILs also play a role in adjusting the t_{Li^+} in the system due to their ionic features. Blends of polymer electrolytes and ILs have been widely studied. Basically, the hybrid polymer/ILs electrolytes can be prepared via (a) mixing polymers with ILs with or without addition of solvents, (b) soaking polymer membranes in ILs, (c) polymerizing in IL solvents.^{62, 111, 117-119} PEO and PVDF-HFP containing polymers are the most frequently used polymers to dope ILs. Due to their excellent electrochemical stability, alkyl pyrrolidiniums and alkyl imidazoliums cations based ILs are commonly studied.^{118, 120} The free-standing polymer/ILs membranes could be fabricated by solution-casting or hot-press methods. Passerini group and Scrosati group have done some solid works on studying electrochemical properties of dimensionally stable polymers/ILs membranes.^{29, 49, 114, 117, 118, 121, 122} N-methyl-N-propyl-pyrrolidinium bis-(trifluoromethanesulfonyl)imide (PyR₁₃TFSI), N-n-butyl-N-ethylpyrrolidinium N,N-

bis(trifluoromethane)sulfonamide (PyR₂₄TFSI), and N-butyl-N-methylpyrrolidinium bis-(fluorosulfonyl) imide (PyR₁₄FSI) are mostly used ILs because of their wide cathodic stability limit, good thermal stability, and compatibility with lithium.^{118, 121, 122} For example, Kim et al. developed a series of PEO-LiTFSI electrolytes incorporated with PyR_{1A}TFSI ILs (the subscript A stands for different alkyl side chain length and alkyl type. For example, A=n3 means n-propyl group). It was found that ILs in the polymer matrix did not give any negative influence on the electrochemical stability of the polymers. The PEO-PyR_{1n3}TFSI-LiTFSI hybrid electrolyte exhibited σ of 1.38×10^{-4} S/cm at 20 °C when PyR_{1n3}/Li⁺ molar ratio was 0.96. This was significantly larger than the ILs-free PEO-LiTFSI sample (1.33×10^{-6} S/cm). The increase of σ was due to the suppression of PEO crystallization and the coordination of Li⁺ to TFSI⁻ (from both LiTFSI and PyR_{1A}TFSI) in addition to PEO chains.¹¹⁹ The PEO matrix was further strengthened by UV crosslinking that enabled higher ILs content in the polymer film. The σ of crosslinked PEO-PyR₁₄TFSI-LiTFSI was slightly higher than that of linear PEO-PyR₁₄TFSI-LiTFSI over the temperature range from -40 °C to 100 °C.¹¹⁴ At temperature above 30 °C, this Li/SPE/LFP battery showed more than 150 mA·h/g of delivered capacity at 0.1 C and good term stability. In the case of ILs trapped PVDF-HFP polymeric films, it was discovered that by adding small amount of EC-PC mixture to the PVDF-HFP/ILs membrane, ion transport was improved, and passivation layer on the lithium electrode was formed.^{29, 122}

Imidazolium based ILs are another choice for the polymers/ILs systems. The tertiary nitrogen of the imidazole ring can be readily quaternized producing positively charged ring which was thermal stable (up to 275 °C). Kumar et al. investigated PEO/lithium trifluoromethanesulfonate (LiCF₃SO₃ or LiTf) doped by ILs 1-ethyl 3-methyl imidazolium trifluoromethanesulfonate (EMITf). High σ of 3×10^{-4} S/cm was obtained when the composition was PEOLiTf(EO/Li=25)+40 wt.% EMITf.¹²³ Nair et al. reported a facile way to fabricate free-standing crosslinked PEO/LiTFSI films with trapped EMI-TFSI. Basically, the ternary mixture of

PEO/LiTFSI/EMI-TFSI was hot-pressed into 90 μm thick film followed by exposure to UV light for crosslinking. This SPE after UV irradiation was much tougher than the uncrosslinked polymer. It showed σ of 2.5×10^{-4} S/cm at 20 $^{\circ}\text{C}$ and above 10^{-3} S/cm at 50 $^{\circ}\text{C}$. To ensure excellent contact of the SPE with electrode materials, the precursor film of PEO/LiTFSI/EMI-TFSI mixture was first obtained by hot pressing onto the LFP electrode and the UV light was then turned on to initiate the photo-crosslinking.¹²⁴

1.3.5.3 Poly(IL)s

Polymeric ILs (or Poly(IL)s) have been attracting much attention because of the excellent affinity and compatibility with ILs minimizing the chance to leak.¹²⁵⁻¹³² Poly(IL)s are polymerized form of IL monomers so that advantages of ILs are partially integrated into the polymers. Poly(IL)s as a new type of polyelectrolyte can be classified as polycations,^{127, 133} polyanions,^{131, 134} and polyzwitterions¹³⁵. (Figure 1-13) Different types of anions in the poly(IL)s strongly influence the physical properties of polymers such as solubility, σ , T_g , and thermal stability. For example, the imidazolium-based poly(IL)s with halide anions are water soluble. When the anions replaced to other fluorine containing counter ions, the polymers tend to be hydrophobic. It has also been found that different anions change T_g of poly(IL)s as much as following the order of $\text{Br} > \text{PF}_6 > \text{BF}_4 > \text{TFSI}$. Their σ values, however, follow the opposite trend as $\text{TFSI} > \text{BF}_4 > \text{PF}_6$. This is not surprising because lower T_g allows higher chain flexibility favoring ion transport. In addition, the cation ring structure and spacer structure are other two main factors influencing the σ of Poly(IL)s. For imidazolium based poly(IL)s, if the C2 position of the imidazole ring substituted by alkyl groups, the cathodic electrochemical stability can be improved, while the σ will drop obviously. Meanwhile, using ethylene oxide derivatives to

substitute the quaternized ammonium lead to improvement of σ . If IL structure was located far from the polymer main chain, the σ could also be enhanced.^{29, 136}

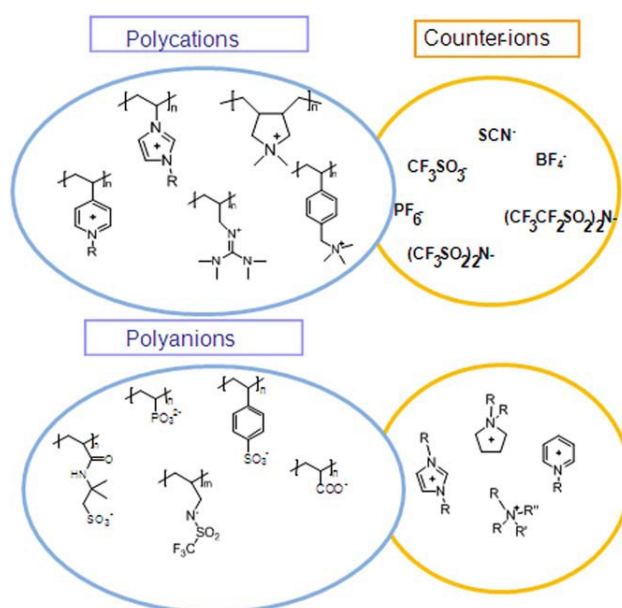


Figure 1-13 Representative structures of poly(ILs).¹³⁷

Most of the poly(IL)s reported for battery application are polycations due to the convenience of synthesis, they were combined with Li-salt and plasticizers (usually ILs) to form three component system.^{127, 129, 132, 138, 139} For example, Yin and coworkers designed a new synthetic route to prepare imidazolium-based poly(IL)s: poly(1-ethyl-3-vinylimidazolium bis(trifluoromethanesulfonylimide)) that had higher molecular weight than poly(IL)s polymerized directly from ILs monomers.¹⁴⁰ The poly(IL), (1,2-dimethyl-3-ethoxyethyl imidazolium bis(trifluoromethanesulfonyl) imide (IM(2o2)11TFSI)) as plasticizer IL, and LiTFSI salt were dissolved in acetonitrile. The poly(IL) films were prepared by solution cast method. The Li/LFP coin cells using the poly(IL)s could deliver higher specific capacity than conventional poly(IL)s (more than 40 mA·h/g at 0.1 C rate, 60 °C). Zhang et al. developed a poly(IL) network

electrolyte containing high density of ion pairs from ILs structure.¹²⁶ It was expected that the densely arranged charged units provided many weak electrostatic interaction sites for Li⁺ movement and the space among the high charge density poly(IL) domains provided channels for fast Li⁺ transport. The poly(IL)/LiTFSI crosslinked membrane showed σ at room temperature of 1.17×10^{-4} S/cm. After mixing with 1-ethyl-3-methyl- imidazolium bis(trifluoromethane)sulfonimide (EMIM-TFSI), the σ could further increased to 5.32×10^{-3} S/cm and the anodic electrochemical stability could be above 5 V. The Li/poly(IL)@LiTFSI-EMIM-TFSI/LFP batteries showed initial discharge capacity above 143 mA·h/g at room temperature.

Poly(IL)s could also be grafted onto inorganic nanoparticles through living/controlled free radical polymerization to produce new SPE with continuous ion conductive network. Sato et al. successfully polymerized IL monomer, *N, N*-diethyl-*N*-(2-methacryloylethyl)-*N*-methylammonium bis(trifluoromethylsulfonyl)imide (DEMM-TFSI), on silica nanoparticles using atom transfer radical polymerization (ATRP). By careful mixing these hybrid silica particles with ILs under the optimal composition in volatile solvent followed by solution casting, interesting colloidal crystal films were prepared (PSiP/IL, Figure 1-14).¹²⁹ The σ of the film was 1.7×10^{-4} S/cm at 30 °C. The potential value as solid electrolyte in LTO/LiMn₂O₄ battery was confirmed as well.

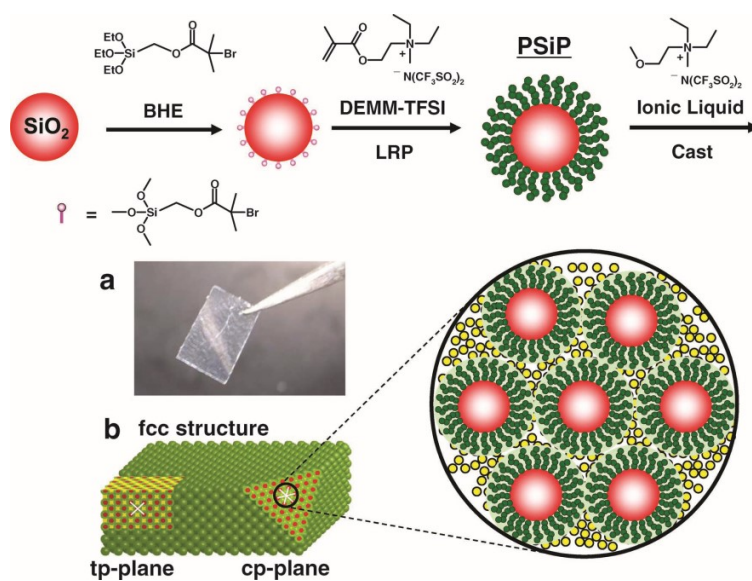


Figure 1-14 Synthesis and preparation of PSiP/IL solid electrolyte.¹²⁹

Chapter 2

Organic-Inorganic Hybrid Electrolytes from Ionic Liquid-Functionalized Octasilsesquioxane for Lithium Metal Batteries

2.1 Introduction

Lithium ion batteries are widely used for portable electronics and hybrid electric vehicles due to their high energy density, high efficiency and long life.^{5, 6, 49, 141} One of the major efforts in the development of next-generation lithium batteries to meet the future challenges of transportation and clean energy storage has focused on synthesis and characterization of polymer electrolytes.^{6, 27, 59, 142} Current rechargeable lithium batteries to power portable electronic devices and electric vehicles use a flammable mixture of carbonate solvents in electrolytes, which create safety and reliability concerns.^{20, 49} Furthermore, the presence of liquid electrolytes prevents the utilization of highly energetic metallic lithium anodes owing to the reactivity of the highly volatile organic solvents and the formation of lithium dendrite that may give rise to thermal runaway and even explosions. It is thus expected that the replacement of the conventional liquid organic electrolytes by solid-state electrolytes significantly improves the safety characteristics of high-energy batteries. For solid-state electrolytes addressed to battery applications, they have to concurrently possess a range of desirable properties such as high thermal stability, good mechanical strength, and a wide electrochemical stability window in addition to high ionic conductivity.^{5, 7, 27, 49, 66, 138} To date, poly(ethylene oxide) (PEO), a semicrystalline polymer, complexed with lithium salts such as lithium bis(trifluoromethylsulfonyl)imide (LiTFSI) has been the most widely studied and remains the best polymer electrolytes.^{7, 143} However, PEO exhibits poor conductivities (*i.e.* $\sim 10^{-6}$ S/cm) at room temperature as a result of crystallization. A practically useful conductivity value (\geq

10^{-4} S/cm) can only be achieved in PEO based polymer electrolytes above 70 °C which corresponds to semicrystalline-amorphous phase transition temperature of PEO.³⁸⁻⁴⁰ The addition of organic solvents able to compete with the polymer ether oxygens for Li⁺ cation coordination has been demonstrated as a means of attaining a high ionic conductivity at room temperature.^{72, 144} Unfortunately, the volatile and flammability nature of these solvents still cause safety concerns. More recently, much attention has been devoted to the investigation of alternative solid electrolytes beyond the state-of-the-art. In particular, ionic liquids (ILs) offer many attractive features as electrolytes, including non-flammability, excellent chemical and electrochemical stability, negligible vapor pressure and high ionic conductivity.^{113, 145} Solidification of ILs including polymerization of IL-containing monomers and grafting ILs onto inorganic nanoparticles has thus been carried out and explored as solid-state electrolytes for lithium batteries.^{16, 129, 137, 146-148} However, the immobilized ILs have not shown much improved ionic conductivity in comparison to PEO based polymer electrolytes, e.g. 10^{-5} S/cm at room temperature, although the plasticized solid electrolytes that containing additives such as organic solvents and ILs show much improved conductivity values.^{20, 53, 132}

Herein, we report the preparation and characterization of a novel class of solid electrolytes based on ionic liquid-functionalized polyhedral oligomeric silsesquioxanes (POSS-IL). The electrolyte not only is nonflammable but also exhibits an impressive ionic conductivity of 4.8×10^{-4} S/cm at 25 °C when doped with LiTFSI and a large electrochemical stability window approaching 5 V. We further demonstrate successful operation of Li/ Li₄Ti₅O₁₂ (LTO) and Li/ LiFePO₄ (LFP) batteries at 25 °C using the prepared solid electrolyte. This is especially noticeable because the state-of-the-art all-solid-state polymer electrolytes are typically cycled at elevated temperatures.^{40, 82, 92}

2.2 Experimental

2.2.1 Materials

Octasilane polyhedral oligomeric silsesquioxane (POSS) was purchased from Hybrid Plastics and dried at 60 °C under vacuum overnight before use. Hexaethylene glycol (97 %), triphenyl phosphine (99 %), tetrabromomethane (CBr₄, 99%), trichlorovinylsilane (97 %), lithium bis(trifluoromethanesulfonyl) imide (LiTFSI), Karstedt catalyst solution in xylene (2%), 1-butyl imidazole (98 %), anhydrous acetonitrile (ACN), anhydrous dimethylformamide (DMF), Anhydrous tetrahydrofuran (THF), and anhydrous benzene were purchased from Sigma-Aldrich. Dichloromethane (DCM), diethyl ether, ethyl acetate (EA), chloroform, and methanol were purchased from VWR.

2.2.2 Synthesis of 17-bromo-3,6,9,12,15-pentaoxaheptadecan-1-ol (2)

In a 50 mL flask equipped with a magnetic stirrer, hexaethylene glycol (hEG, 10 g, 35.42 mmol) and triphenyl phosphine (4.65 g, 17.71 mmol) were dissolved in 25 mL anhydrous THF at 30 °C. The system was purged with nitrogen for 35 min before CBr₄ (5.87 g, 17.71 mmol) was added. The reaction was allowed to proceed for 4 hours at 30 °C under nitrogen atmosphere. The solution was then concentrated on a rotary evaporator at 50 °C and the crude product was purified by column chromatography with chloroform/methanol (95:5 v/v) to give 17-bromo-3,6,9,12,15-pentaoxaheptadecan-1-ol as slight yellow oil. ¹H NMR (300 MHz, CDCl₃, ppm) δ: 3.16 (s, -OH), 3.45 (t, -CH₂-Br), 3.58-3.68 (m, -O-CH₂-), 3.78 (t, -CH₂-CH₂-Br); ¹³C NMR (CDCl₃, ppm) δ: 30.1, 61.6, 70.2-70.7 (br), 73.0 (-CH₂-CH₂-Br).

2.2.3 Synthesis of vinyl tris(17-bromo-3,6,9,12,15-pentaoxaheptadecan-1-yl) silane (**3**)

In a 100 mL flask equipped with a magnetic stirrer, 17-bromo-3,6,9,12,15-pentaoxaheptadecan-1-ol (5.6 g, 0.016 mol) and triethylamine (3.2 g, 0.032 mol) were dissolved in toluene (50 ml) at room temperature. The system was purged with nitrogen for 40 min before trichlorovinylsilane (0.873 g, 5.33 mmol) was added dropwise. The reaction mixture was stirred for 3 hours at room temperature under nitrogen atmosphere. The product solution was then diluted with EA (50 ml), washed with DI water and dried over anhydrous Na₂SO₄. The organic layer was separated, concentrated, and dried under vacuum at 60 °C to give product **3**. ¹H NMR (300 MHz, CDCl₃, ppm) δ: 3.43 (t, -CH₂-Br), 3.58-3.68 (m, -O-CH₂-), 3.79 (-O-CH₂-CH₂-Br), 3.89 (t, -Si-O-CH₂-), 5.9-6.1 (m, CH₂=CH-Si-), ¹³C NMR (CDCl₃, ppm) δ: 30.1, 62.4 (-Si-O-CH₂), 70.8-71.9 (signal overlap), 72.7 (-CH₂-CH₂-Br), 137.4 (CH₂=CH-Si-).

2.2.4 Synthesis of POSS-IL (**6**)

In a 50 mL flame dried flask equipped with a magnetic stirrer, POSS (640 mg, 0.63 mmol) and product **3** (5.48 g, 5.04 mmol) were dissolved in anhydrous benzene (20 ml) at room temperature. The system was degassed by bubbling with nitrogen for 1 hour. 2 drops (14 μL) of Karstedt catalyst were added subsequently. The mixture was stirred in an oil bath at 50 °C for 48 hours. Then the solvent was evaporated on a rotary evaporator and dried in vacuum at 60 °C to give the product **4**. Then the product **4** was dissolved in DMF (20 ml), 1-butyl imidazole was (2.04 g, 16.43 mmol) and the solution was stirred at 40 °C under N₂ for 24 hours. After removal of solvent, the obtained product was mixed with LiTFSI (4.72 g, 16.43 mmol) in anhydrous ACN (20 ml). The mixture was stirred for 24 hours at room before the solvent was evaporated. The product was redissolved in DCM, lithium bromide was removed by filtration. The final products

were purified by washing with diethyl ether several times, then the product were dried under vacuum to give final product **6**: POSS-IL: ^1H NMR (300 MHz, DMSO- d_6 , ppm) δ : 0.90 (t, $-\text{CH}_3$), 1.26 (m, $-\text{CH}_2-\text{CH}_2-\text{CH}_3$), 1.78 (m, $-\text{CH}_2-\text{CH}_2-\text{CH}_3$), 3.42-3.60 (m, $-\text{O}-\text{CH}_2-$), 4.20 (t, $\text{O}-\text{CH}_2-\text{CH}_2-\text{N}-$), 4.35 (t, $-\text{N}-\text{CH}_2-\text{CH}_2-$), 7.78 (d, $-\text{N}-\text{CH}=\text{CH}-\text{N}-$), 9.18 (s, $-\text{N}=\text{CH}-\text{N}-$).

2.2.5 Characterization Instrument

The chemical structures of the polymers were determined from ^1H NMR and ^{13}C NMR on a Bruker AM-300 Nuclear Magnetic Resonance Spectrometer. FTIR spectra were obtained using Bruker Vertex 70 spectrometer. Raman spectra were measured on a Horiba LabRam HR Evolution equipped with an Oxixus DPSS 532nm laser and a Horiba Synapse EM detector. Analysis of the peak around 742 cm^{-1} was performed with the 1800 gr/mm grating which yields a spectral resolution of 0.4 cm^{-1} . We tested for laser beam damage and found that all species measured with Raman were stable even at the maximum incident power of 45mW. All thermal analysis Raman measurements presented in this paper were performed with an acquisition time of 30 sec, a $50\text{ }\mu\text{m}$ confocal pinhole and 2 accumulation to account for any interference. A Linkam HFS600 temperature stage was used to change the environmental temperature and the objective used was an Olympus 50x LMPLFLN with a numerical aperture of 0.5. At each temperature set point there was a wait time > 10 min before each measurement to ensure that the temperature of the sample had stabilized. Pulse field gradient NMR (PFG-NMR) diffusion measurements were performed in Bruker Avance-III-HD-500 MHz, 11.7T, prodigy probe. Spectrometer frequency for ^7Li and ^{19}F are 194.4 MHz and 470.6 MHz. Signal attenuation parameters: diffusion delay (Δ) ranges from 0.1-0.6 s, gradient pulse length (δ) is 6 ms, gradient pulse magnitude (g) ranges from 0-50 G/cm, relaxation delay is 10s.

X-ray Photoelectron Spectroscopy (XPS) experiments were performed using a Physical Electronics VersaProbe II instrument equipped with a monochromatic Al $K\alpha$ x-ray source ($h\nu = 1,486.7$ eV) and a concentric hemispherical analyzer. Charge neutralization was performed using both low energy electrons (<5 eV) and argon ions. The binding energy axis was calibrated using sputter cleaned Cu foil (Cu $2p_{3/2} = 932.7$ eV, Cu $2p_{3/2} = 75.1$ eV). Peaks were charge referenced to CH_x band in the carbon 1s spectra at 284.8 eV. Measurements were made at a takeoff angle of 45° with respect to the sample surface plane. This resulted in a typical sampling depth of 3-6 nm (95% of the signal originated from this depth or shallower). Quantification was done using instrumental relative sensitivity factors (RSFs) that account for the x-ray cross section and inelastic mean free path of the electrons. The curves were fitted using mixed Gaussian/Lorentzian profile.

Glass transition temperature (T_g) was measured on TA Q100 differential scanning calorimeter (DSC) at a heating and cooling rate of 10 °C/min in the temperature range from -80 to 100 °C. Thermogravimetric analysis (TGA) measurements was performed on TA Instrument model Q50 at a heating rate of 10 °C/min under N_2 from room temperature up to a maximum of 800 °C to study the thermal stability. Wide-angle X-ray diffraction (WAXD) was performed on a Rigaku DMAX-Rapid Microdiffractometer equipped with a 2-D detector, also using $CuK\alpha$ radiation. The software routines were used to evaluate the scattering intensity as a function of the diffraction angle of 2θ , or q , defined as $q=4\pi\sin(\theta)/\lambda$.

Dynamic shear moduli were measured by using RDS-IIE rheometer. The POSS-IL sample was placed between two parallel plates with a diameter 25 mm. The shear strain was varied to obtain storage modulus (G') and loss modulus (G'') at room temperature.

The ionic conductivity (σ) was measured by Broadband Dielectric Relaxation Spectroscopy (DRS). Measurements were performed on a Concept 40 system from Novocontrol GmbH over

the frequency range 10 mHz to 10 MHz. Temperature was controlled by a Quatro temperature control system with a precision of greater than ± 0.1 °C. All polymers were measured over the temperature range from -25 °C to 80 °C. To prepare samples for DRS measurements, the polymer electrolytes solutions were casted onto stainless steel electrodes and dried under vacuum overnight at 60 °C.

Electrochemical impedance spectroscopy (EIS) was used to study the interfacial properties of Li/Li symmetrical cells using a PAR 2273 FRA/potentiostat. The lithium transference number (t_{Li^+}) of the electrolyte was also calculated from the results obtained from the Nyquist plots measured by EIS (1 MHz to 100 mHz, 20 mV AC voltage). t_{Li^+} was calculated according to method reported by Bruce and Vincent⁸⁰ (a combination of AC impedance and DC polarization measurements) which was widely used for the determination of t_{Li^+} of polymer-IL-Li salt system.^{115, 149, 150} The equation can be written as $t_{Li^+} = I_s(V - I_i R_i) / I_i(V - I_s R_s)$. V is the constant DC voltage applied; I_i and I_s are the initial and steady state current, R_i and R_s are the interfacial resistance before and after DC polarization. DC voltage of 30 mV was imposed on the two lithium electrodes. Voltammetry experiments were performed on PAR Potentiostat/Galvanostat Model 263A using a sealed cell with synthesized polymer electrolytes sandwiched between a stainless steel disk working electrode and a lithium foil counter/reference electrode aided by a teflon o-ring spacer with inner diameter of 1 cm. Tests were done at a scan rate of 1 mV/s at 25 °C.

Cell assembly and battery performances. The synthesized polymer electrolyte was dissolved in anhydrous THF (11% w/v) in the glove box. LiTFSI was then added to the above solution ([EO]:[Li]=12:1). Coin cells (CR2032) were assembled in an argon-filled glovebox (Labstar MB10, MBRAUN). $Li_4Ti_5O_{12}$ (LTO, Ishihara Sangyo Kaisha, Ltd.) and $LiFePO_4$ (LFP, Sud-Chemie) were selected as cathode material (slurries containing 80 wt% of LTO or LFP, 10 wt% of super P (a carbon additive to enhance electrode conductivity) and 10 wt% POSS-IL in 1-

Methyl-2-pyrrolidone (NMP) were made and casted onto 9 μm thick copper foil (15 μm thick aluminum foil was used for LFP) followed by doctor blade method). The areal density of active material was ca. 2.8 mg/cm^2 . The cathode sheets were punched into 1 cm diameter (0.785 cm^2) disks, vacuum dried at 80 $^\circ\text{C}$ completely, weighted, and transferred into glove box for coin cell assembly. Lithium foils (MTI, 250 μm thick) were used as the anode. The polymer electrolyte solution was casted on the anode and the solvent was evaporated in the glovebox leaving the solvent-free polymer electrolyte membrane. The coin cells were assembled by sandwiching the solvent-free polymer electrolyte between cathode and anode in the coin cell case with a 125 μm ring shaped Teflon spacer. Battery tests were measured on a Neware CT-3008 battery tester. The theoretical capacities of LTO and LFP were 175 $\text{mA}\cdot\text{h}/\text{g}$ and 170 $\text{mA}\cdot\text{h}/\text{g}$, respectively.¹¹⁸ ESPEC BTU-133 temperature chamber was used to change the environmental temperature for the coin cells. The batteries were cycled between 1.3 to 2.0 V for Li/POSS-IL-LiTFSI/LTO cell and 2.5 to 3.9 V for Li/POSS-IL-LiTFSI/LFP cell under constant current condition. Conventional liquid electrolyte (1 M LiTFSI in ethylene carbonate-dimethyl carbonate (EC-DMC, 1:1, v/v)) was used as contrast in the lithium strip/plate and galvanostatic polarization tests.

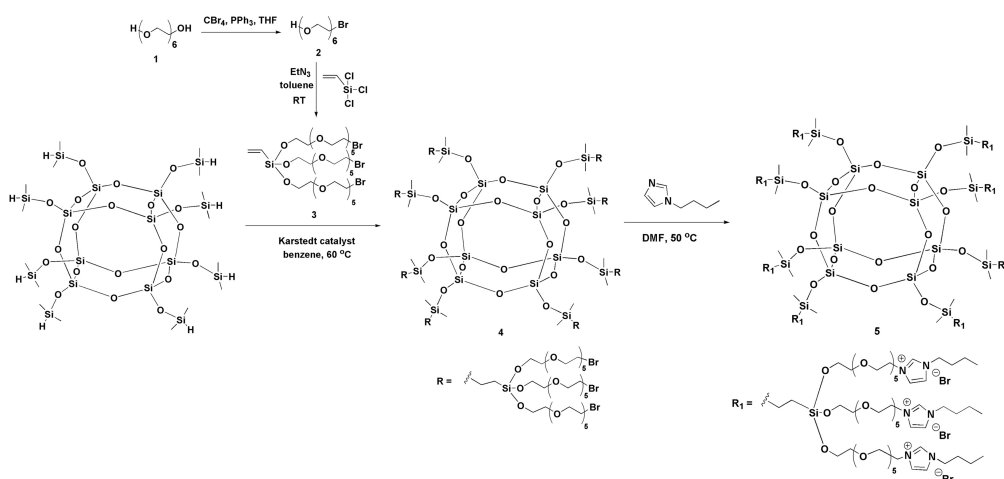
Field Emission Scanning Electron Microscopy (FEI NanoSEM 630 FESEM) was used to study the electrode surface morphology.

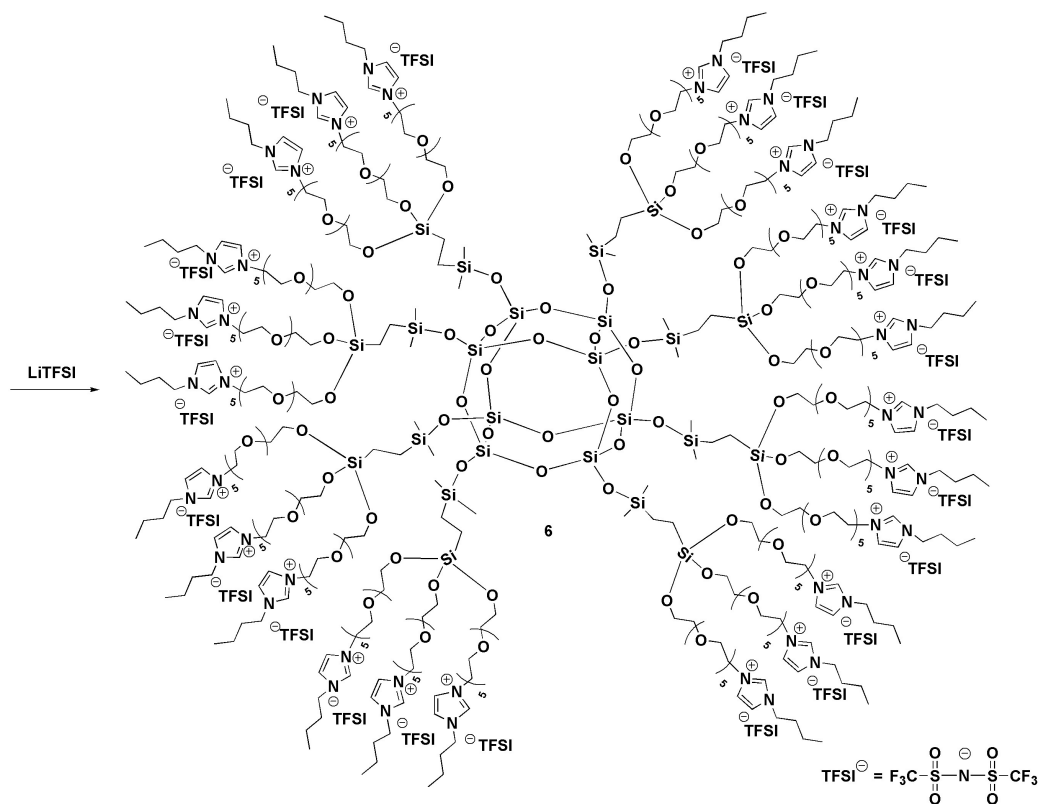
Flammability test was performed with Master Microtorch fed with butane flux, inert glass fiber filters strips with 1 cm width and 0.6 μm pore size were soaked in the concentrated POSS-IL solution in anhydrous THF for 5 min. Then these strips were dried and placed at fixed distance from the microtorch before testing. As a control, glass fiber filter was also soaked in liquid electrolyte (1 M LiTFSI EC-DMC, 1:1, v/v).

2.3 Result and discussion

2.3.1 Chemical synthesis and characterization

The synthetic route of POSS-IL is shown in Scheme 2-1. The mono-bromination of hexaethylene glycol (HEG) was achieved by modification of the chain-end hydroxyl groups of hEG using tetrabromomethane (CBr_4) as the bromine source. Then the mono-brominated HEG was coupled with trichlorovinylsilane. After that, the unreacted double bond reacted with POSS through hydrosilylation reaction. After tethering the HEG arms' terminals with 1-butyl imidazole and subsequent anion-exchange, POSS-IL was obtained. Imidazole rings were selected as chain end IL molecule because the nitrogen atom in imidazole ring can be readily quaternized with halogen terminated polymers and imidazolium based ILs proved to be applicable for LIBs owing to their high σ .^{151, 152} The negative charges on TFSI⁻ anions are delocalized which can facilitate the Li^+ ions dissociation from ion pairs.^{153, 154} Also, TFSI⁻ anions have plasticizing effect on polymers promoting chain flexibility.^{133, 155} Figure 2-1 shows the appearance of the POSS-IL.





Scheme 2-1 Synthetic route of POSS-IL.

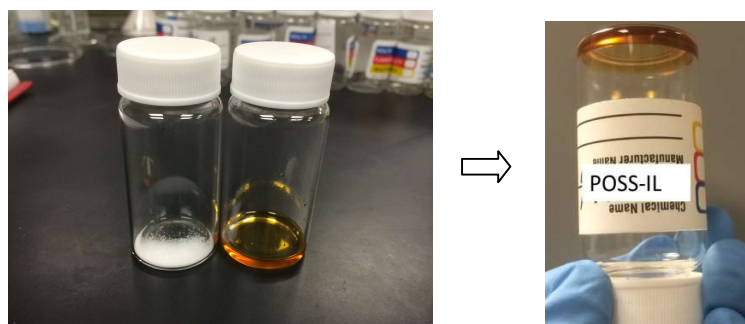


Figure 2-1 Picture of POSS powder and compound 2 (left) and POSS-IL (right).

From the ^1H NMR spectra, the chemical shift (δ) of the protons on the vinyl group (5.9-6.0 ppm) in Figure 2-4 and Si-H protons (5.1 ppm) in Figure 2-2 are not observed in the ^1H NMR of POSS-IL in Figure 2-5 indicating complete hydrosilylation reaction.

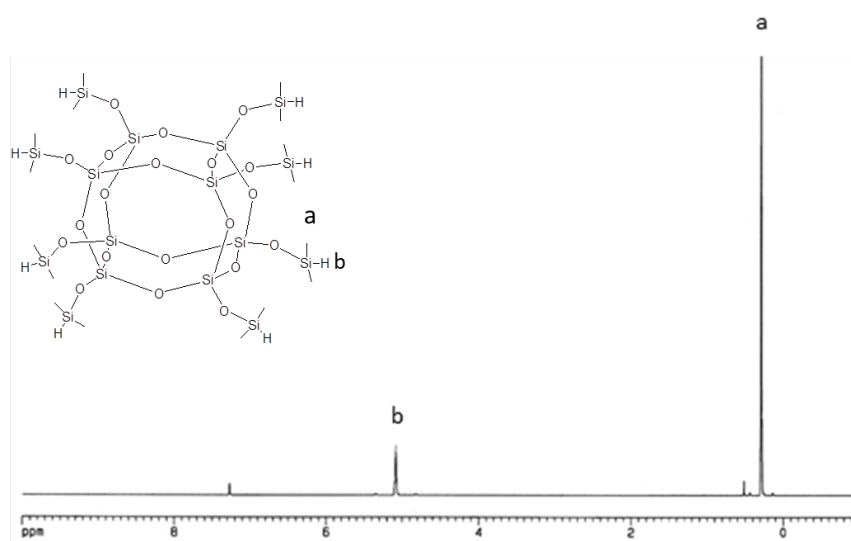


Figure 2-2 ^1H NMR spectrum of POSS.

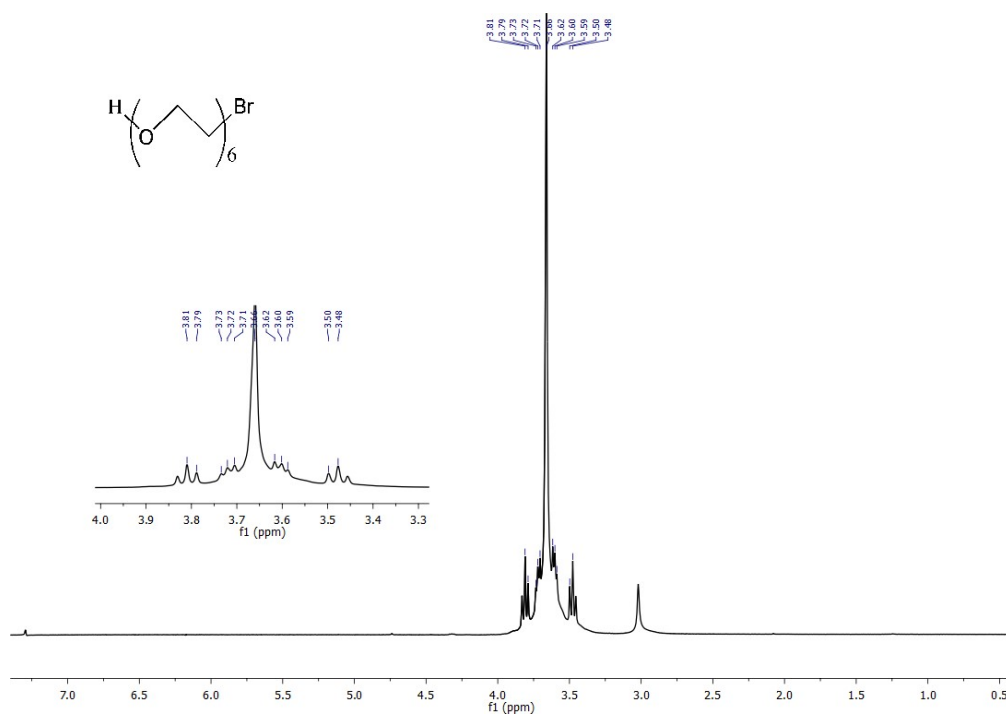
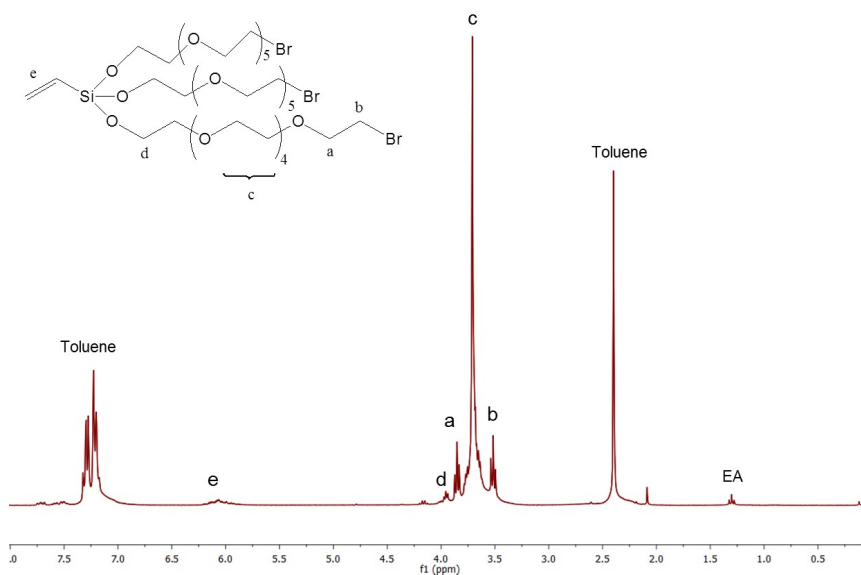
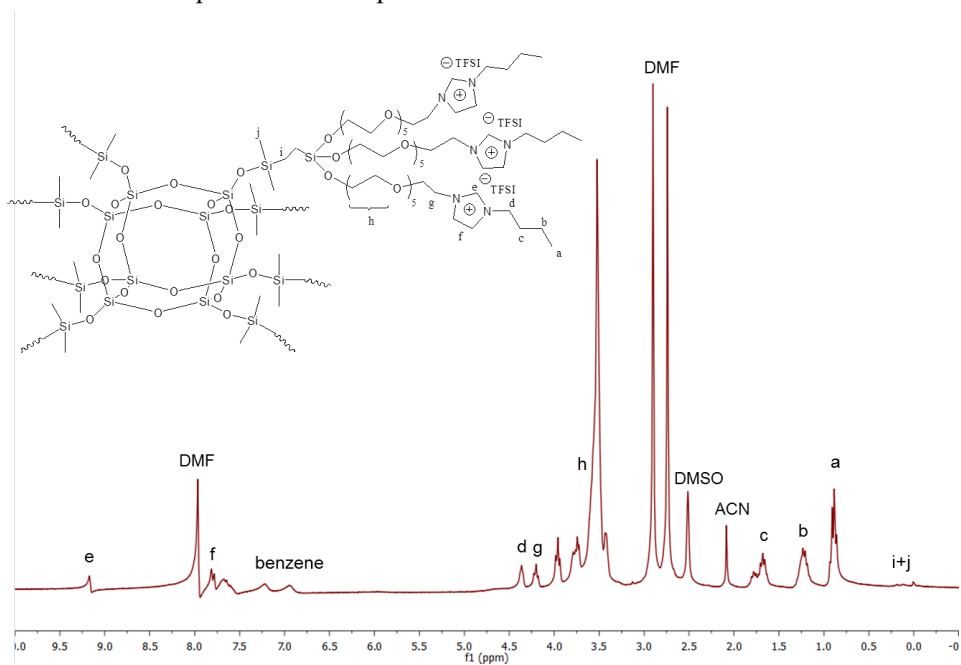


Figure 2-3 ^1H NMR of compound 2.Figure 2-4 ^1H NMR spectrum of compound 3.Figure 2-5 ^1H NMR spectrum of POSS-IL

The Si-H stretching vibration peak at $2,140\text{ cm}^{-1}$ and Si-H bending vibration peak at 900 cm^{-1} of the POSS molecules were absent in the FTIR spectrum of POSS-IL, which also confirmed the completion of grafting reaction. The characteristic vibrational bands of TFSI⁻ anions (1352 cm^{-1} , 1195 cm^{-1} , 1135 cm^{-1} , 1056 cm^{-1}) could be observed in the FTIR spectrum of POSS-IL (Figure 2-6). The C-N and C-C skeleton stretching vibrations of imidazole ring were found at 1448 cm^{-1} and 1570 cm^{-1} .

Figure 2-6 FTIR spectra of POSS and POSS-IL.

Furthermore, the tethered IL ion pairs in POSS-IL were also characterized by XPS (Figure 2-7). Two major peaks (401.7 eV and 399.1) in the N1s spectrum were observed after peak fitting using Gaussian-Lorentz model functions. Peak at 401.7 eV was assigned to N atoms in the positive charged imidazolium ring (N^+), peak at 399.1 eV was assigned to N atom in the TFSI⁻ anion (N^-).¹⁵⁶ The peak intensity ratio of N^+/N^- was 2.1:1, which was very close to the theoretical value 2:1 and this proved that the ratio of cation and anion is 1:1 in POSS-IL.

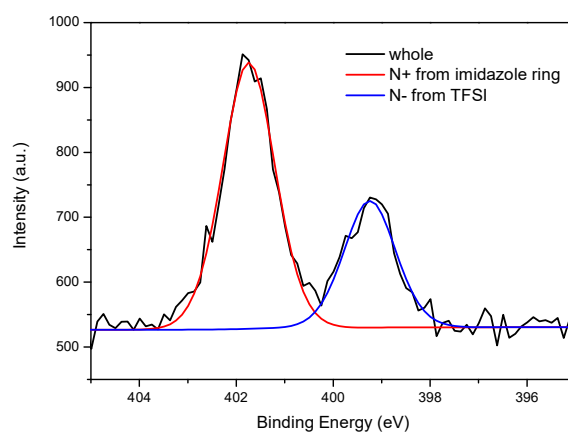


Figure 2-7 X-ray photoelectron spectroscopy N 1s spectrum of POSS-IL.

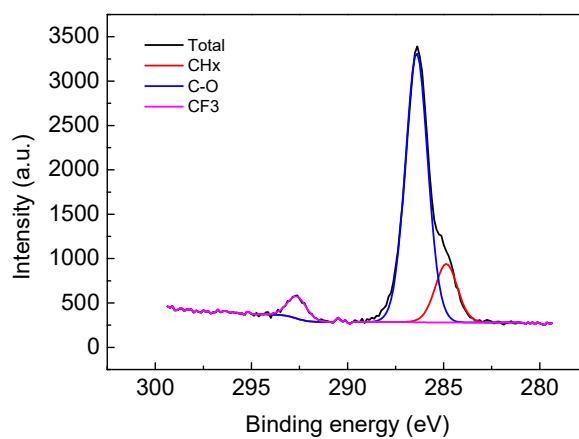


Figure 2-8 X-ray photoelectron spectroscopy C 1s spectrum of POSS-IL.

2.3.2 Thermal properties

The glass transition temperature (T_g) of POSS-IL is $-33\text{ }^\circ\text{C}$ from the DSC thermograms (Figure 2-9 left). Upon doping with LiTFSI, the T_g increased to $-31\text{ }^\circ\text{C}$. This is probably because the coordination complex of Li^+ and oxygen atoms restricted the polymer chain movement.^{30, 100} The relative low value of T_g was a reflection of quick polymer segmental motion which usually leads to high σ .⁷ No melting peaks were found in the curves showing that POSS-IL was dominated by amorphous phase. Thermal stability is another important parameter ensuring persistent performance of battery electrolyte especially at elevated temperatures. The TGA curves showed that the decomposition temperature of pure POSS was $246\text{ }^\circ\text{C}$. The onset decomposition temperature of POSS-IL was above $250\text{ }^\circ\text{C}$. (Figure 2-9 right)

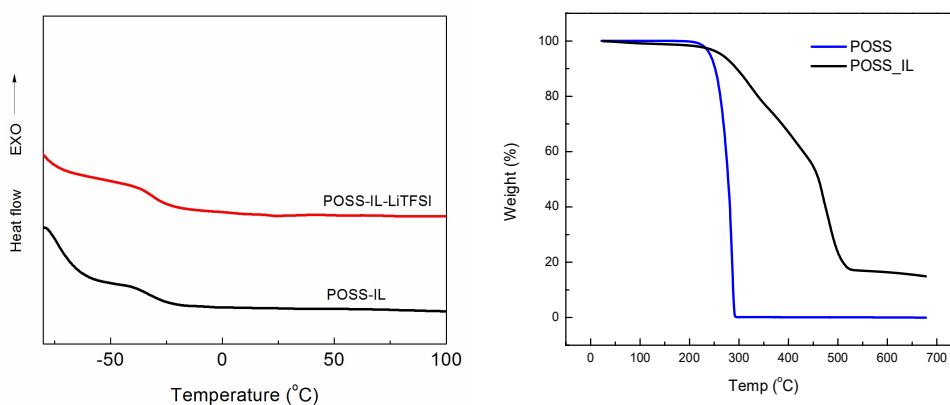


Figure 2-9 DSC and TGA curves of POSS-IL and POSS-IL-LiTFSI.

2.3.3 Microstructure Characterization.

Wide-angle X-ray Diffraction (WAXD) patterns of the POSS-IL and POSS-PEO are shown in Figure 2-10. The broad diffraction halo at $2\theta=7^\circ$ (d-spacing of 1.25 nm) can be related to the POSS inter distance. Another diffraction halo at $2\theta=20.1^\circ$ (d-spacing of 0.44 nm) could be

assigned to the very weak signal of PEG in both POSS-IL and POSS-PEO indicating the amorphous nature of POSS-PEO and POSS-IL.

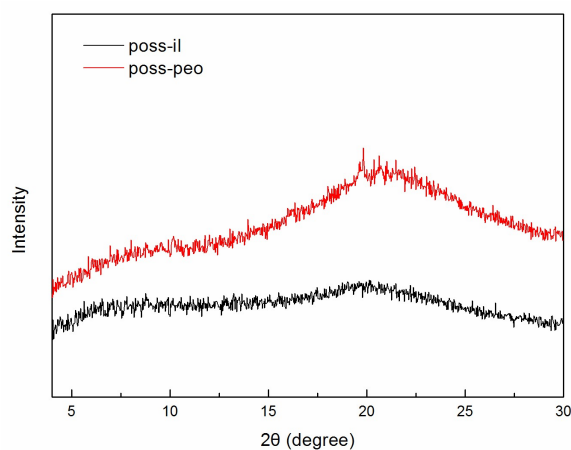


Figure 2-10 XRD patterns of POSS-IL and POSS-PEO.

2.3.4 Mechanical Properties.

Figure 2-11 shows the strain-dependent dynamic moduli of POSS-IL measured in an oscillatory shear flow as a function of applied strain amplitude with fixed frequency ($\omega = 10$ rad/s). At low shear strain region, storage modulus (G') was higher than loss modulus (G'') which indicates the tested sample is a solid-elastic material. With the further increase of the shear strain, G' gradually decreased and G'' reached a maximum value (the corresponding strain is called critical shear strain γ_c) indicating a strain-induced transition to fluid-like state. This behavior may indicate POSS-IL belongs to “soft glassy” materials. Soft glassy materials are individual elements trapped in tight cages produced by interactions with their neighbors as shown in cartoons in left cartoon of Figure 2-11.^{157, 158} The maximum in G'' was a sign of increased mechanical energy dissipation when the cages broke apart. The G' at zero strain was 1.2×10^5 Pa. Solution-casted

membrane of POSS-IL can be successfully prepared owing to the entanglement of the long chains grafted onto POSS.

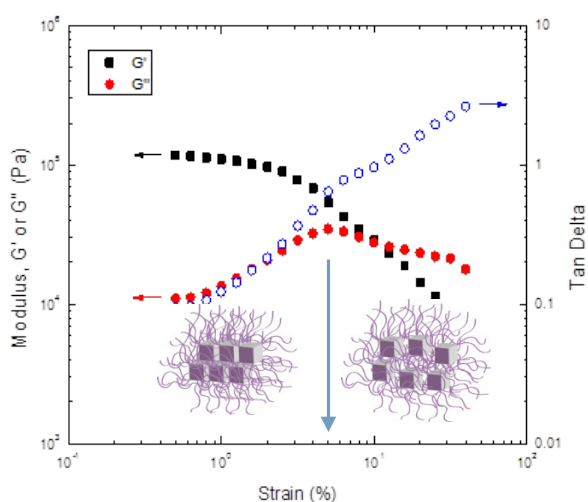


Figure 2-11 The dynamic shear moduli (G' , G'') and tan delta of POSS-IL as a function of applied strain at 25 °C.

2.3.5 Ionic conductivity and electrochemical properties

The temperature dependence of the ionic conductivity (σ) of POSS-IL doped with LiTFSI ([EO]:[Li]=12:1), measured by broadband dielectric relaxation spectroscopy, is presented in Figure 2-12. The POSS grafted with PEO side chains (POSS-PEO) has been prepared and characterized for the purpose of comparison. Clearly, σ of POSS-IL is much greater than that of POSS-PEO over the temperature range of -25 - 80 °C. At 25 °C, σ of POSS-IL/LiTFSI reaches to 4.8×10^{-4} S/cm, which, to the best of our knowledge, is among the highest room-temperature conductivity reported so far for solvent-free organic/polymeric material-based solid Li^+ electrolytes.^{94, 104, 106, 107, 129} On the other hand, POSS-PEO/LiTFSI, exhibits a σ of 5.6×10^{-6} S/cm at 25 °C, which is almost two orders of magnitude lower than POSS-IL. The σ value of POSS-PEO is consistent with the literature results on the PEO-based solid electrolytes measured at room

temperature.^{82, 159} Such a large difference in ionic mobility between POSS-IL and POSS-PEO is attributed to the presence of imidazolium rings at the chain ends in POSS-IL, in which the positive charged imidazole would interact with TFSI⁻ anions by electrostatic force to facilitate the liberation of Li⁺ from LiTFSI salts for higher mobility. To verify this hypothesis, Raman spectroscopy was employed to study the conformations of TFSI⁻ anions in the samples because the expansion-contraction mode of TFSI⁻ anions at $\sim 742\text{ cm}^{-1}$ in Raman spectra is sensitive to its conformational changes. As shown in Figure 2-13 and Figure 2-14, the Raman peak at 742 cm^{-1} can be fitted into three conformers using Gaussian/Lorentzian functions: C_1 , C_2 , and C_{coord} . C_1 (cisoid) and C_2 (transoid) conformers stem from free TFSI⁻ anions and C_{coord} originates from Li⁺ coordinated TFSI⁻ anions.^{151, 160} It is found that the relative peak intensity of C_{coord} in POSS-IL is much weaker than that of C_{coord} in POSS-PEO, indicative of much more uncoordinated, free Li⁺ ions existing in POSS-IL. In addition, as shown in Figure 2-15 where the POSS-PEO-LiTFSI Raman spectrum is subtracted from POSS-IL-LiTFSI spectrum, the appearance of the positive peak at around 740 cm^{-1} represents more free TFSI⁻ anions in POSS-IL-LiTFSI, whereas the negative peak at 746 cm^{-1} stands for less Li⁺ coordinated TFSI⁻ anions in POSS-IL-LiTFSI.

The temperature dependence of σ of POSS-IL shows empirical Vogel-Tammann-Fulcher (VTF) behavior, suggesting that ion conduction is related to molecular relaxation and swinging motions of chains tethered to POSS. For VTF equation, $\sigma = A \cdot T^{-1/2} \exp(-B/R(T-T_0))$, where A is a constant proportional to the number of charge carriers, B is equivalent to the activation energy for ion motion, R is the gas constant, T is the experimental temperature, and T_0 is an empirical reference temperature. The calculated VTF parameters A , B and T_0 for POSS-IL are provided in Table 2-1, and the fitting curves are plotted in Figure 2-12 as solid lines. A lower activation energy is found in POSS-IL in comparison to POSS-PEO, *i.e.* 9.2 vs. 12.2 KJ/mol, signifying a lower energy barrier in POSS-IL for Li⁺ conduction.

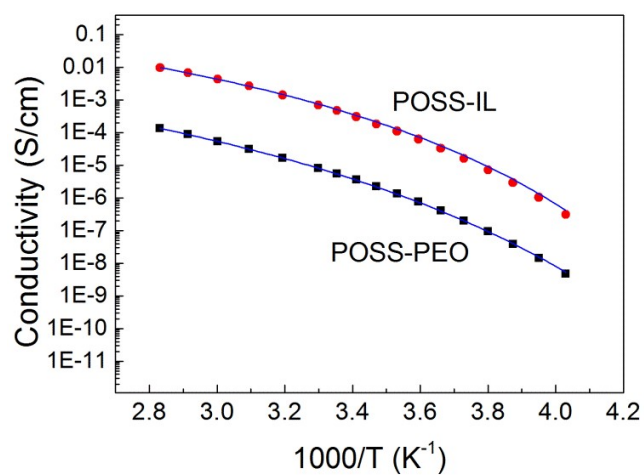


Figure 2-12 Temperature dependence of ionic conductivity of POSS-IL-LiTFSI and POSS-PEO-LiTFSI.

Table 2-1 Ionic conductivity values at room temperature and fitting parameters.

	σ (25 °C, S/cm)	R-square	B (KJ/mol)	$A(S/cm \cdot K^{1/2})$
POSS-IL	4.8×10^{-4}	0.999	9.2	125.8
POSS-PEO	5.6×10^{-6}	0.999	12.2	7.7

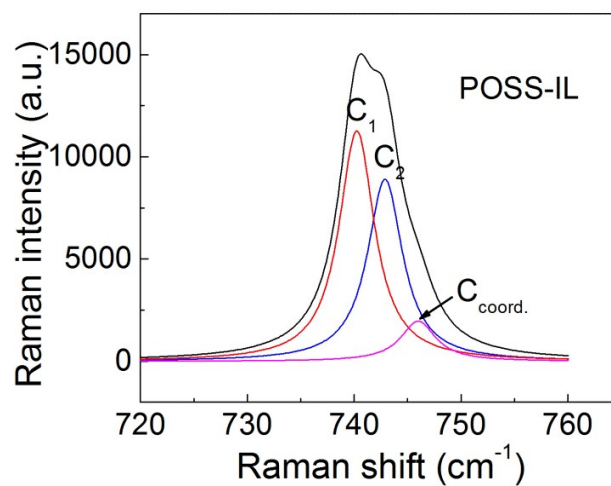


Figure 2-13 Raman Spectra for TFSI⁻ anion vibration of POSS-IL-LiTFSI at 25 °C in the range of 720-760 cm⁻¹.

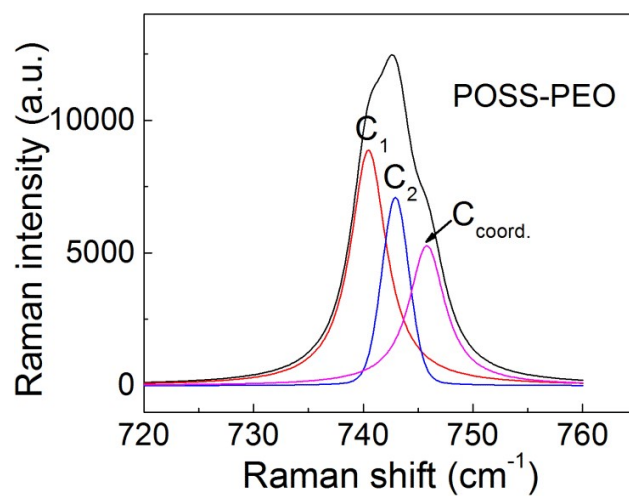


Figure 2-14 Raman Spectra for TFSI⁻ anion vibration of POSS-PEO-LiTFSI at 25 °C in the range of 720-760 cm⁻¹.

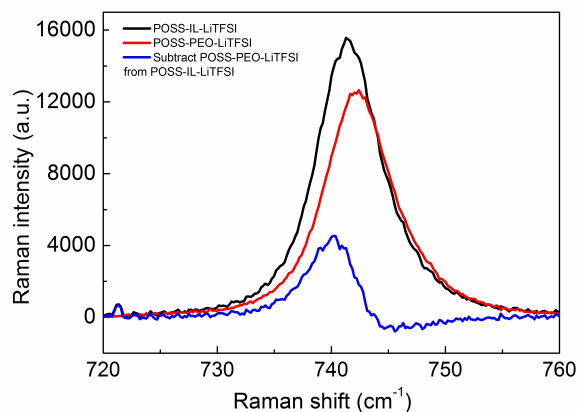


Figure 2-15 Raman spectra of TFSI- anion vibration of POSS-IL-LiTFSI (black), POSS-PEO-LiTFSI (red), and subtracting of POSS-PEO-LiTFSI from POSS-IL-LiTFSI (blue) at 25 °C in the range of 720-760 cm^{-1} .

From FTIR spectra, it was also found that the vibrational band position of antisymmetric stretching of C-O-C shifted from 1100 cm^{-1} to 1090 cm^{-1} when the lithium salt (Lithium hexafluorophosphate, LiPF_6) concentration in POSS-PEO increased. The band shift phenomenon was also reported in other related works.^{161,162} Interestingly, the POSS-IL sample showed no band shift behavior with lithium salt concentration variation. This probably indicates that the ion conduction mechanism in POSS-IL is different from that in POSS-PEO (Figure 2-17).

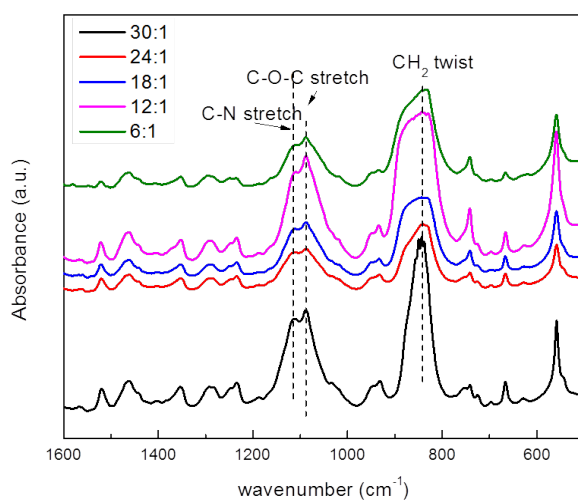


Figure 2-16 FTIR spectra of POSS-IL- LiPF_6 with different LiPF_6 concentrations.

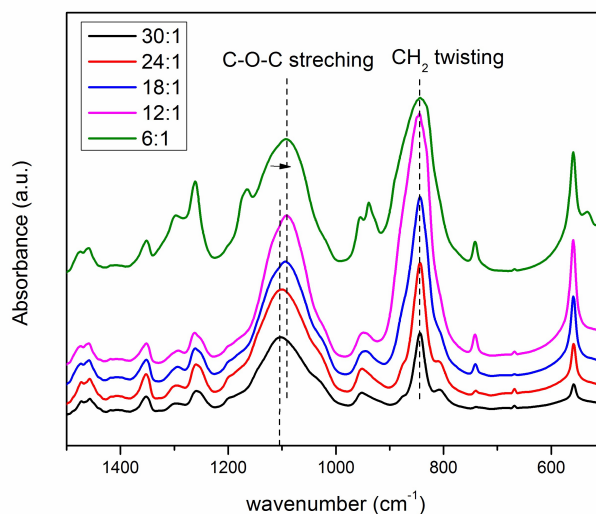


Figure 2-17 FTIR spectra of POSS-PEO-LiPF₆ with different LiPF₆ concentrations.

The interfacial properties of POSS-IL-LiTFSI against lithium electrode were characterized by electrochemical impedance spectroscopy (EIS). From the Nyquist plot of symmetrical Li/electrolyte/Li cells (Figure 2-18 a), the intercept at the real axis at the high frequency part represents bulk electrolyte resistance (R_b). The length between the intercepts of semicircle at the real axis represents interfacial resistance (R_{int}). The impedance measurements were done at different times of storage. The data points were fitted by Z-view software and the equivalent circuit is also shown in (Figure 2-18 a). R_1 is the bulk resistance, R_2 is the interfacial resistance. CPE and W stands for constant phase element and Warburg diffusion impedance (Li diffusion on the electrode/electrolyte interface and electrolyte salt diffusion). The change of R_1 and R_2 (obtained by curve fitting) with time can be seen in Figure (2-18 b). R_1 did not show significant change during the time frame revealing good chemical stability of POSS-IL-LiTFSI. Moreover, R_2 which was related to charge transfer resistance and passive layer resistance increased rapidly during the first three days. This probably resulted from reaction between POSS-IL-LiTFSI and lithium electrode to form passive solid electrolyte interphase (SEI).^{94, 149} After 3 days, the

corresponding R_{int} gradually decreased and stabilized around 420 Ω . This could be due to the gradual stabilization of passive SEI layer.

The fraction of current carried by certain ion is the ion transference number. The Li^+ transference number t_{Li^+} for POSS-IL-LiTFSI electrolyte was measured using Li/electrolyte/Li configuration according to steady state current method (Figure 2-19).⁸⁰ The t_{Li^+} calculated was about 0.3 which is in agreement with previously reported t_{Li^+} for ionic liquid plasticized PEO system.^{62, 124} This value of t_{Li^+} is on the high end for PEO/LiTFSI systems, which is ascribed to a high number of free Li^+ as a result of interaction between imidazolium and TFSI⁻. Moreover, it is thought that the POSS moieties in the hybrid structures may absorb TFSI⁻ and reduce TFSI⁻ mobility, which also contributes to the improved t_{Li^+} value.⁴⁵ We have also performed the PFG-NMR diffusion measurement on POSS-IL-LiTFSI. The self-diffusion coefficients obtained are Li^+ ($D_{\text{Li}^+}=6.9\text{e}^{-12}$ m²/s), TFSI⁻ ($D_{\text{TFSI}^-}=1.2\text{e}^{-11}$ m²/s). The t_{Li^+} calculated by $D_{\text{Li}^+}/(D_{\text{Li}^+}+D_{\text{TFSI}^-})$ is 0.36.

Figure 2-18 a) Nyquist plot of Li/POSS-IL-LiTFSI/Li symmetrical cell at different storage times.
b) Evolution of R_{int} and R_b as a function of storage time.

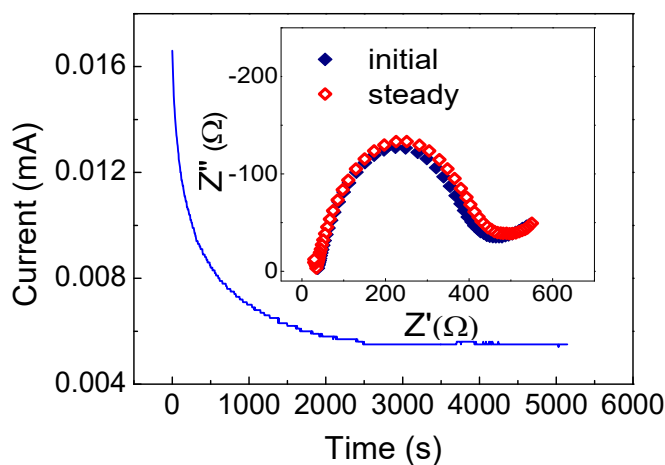


Figure 2-19 Chronoamperometry profile of Li/POSS-IL-LiTFSI/Li cell and inset nyquist plot at 25°C.

The electrochemical stability of POSS-IL-LiTFSI was studied by linear sweep voltammetry (LSV) (Figure 2-20). Stable current can be observed up to 5 V vs. Li/Li^+ . Upon reaching 5 V vs. Li/Li^+ , current value increased significantly showing the oxidative decomposition of POSS-IL-LiTFSI. Almost no residue decomposition current was seen reflecting good sample purity. This result suggests the applicability of POSS-IL-LiTFSI with high potential cathode materials. The anodic decomposition voltage of POSS-PEO-LiTFSI was about 4.2 V vs. Li/Li^+ . The improvement of electrochemical stability of POSS-IL-LiTFSI is possibly due to the more stable passive layer formed on the electrode.^{16, 115} Cyclic voltammetry (CV) was used to study the reversible lithium stripping and plating on stainless steel working electrode of Li/POSS-IL-LiTFSI/stainless steel cell (Figure 2-21). The plating of lithium on the working electrode can be assigned as the cathodic peak at -0.5 V vs. Li/Li^+ . In the returning anodic scan, the peak at 0.3 V vs. Li/Li^+ corresponds to the stripping of lithium. The cathodic and anodic peaks are well defined. It can also be seen that the lithium deposition peak current decreases from 2nd to 3rd cycle slightly. This may be due to the gradual formation of SEI layer that restrains the lithium reduction.¹⁶³

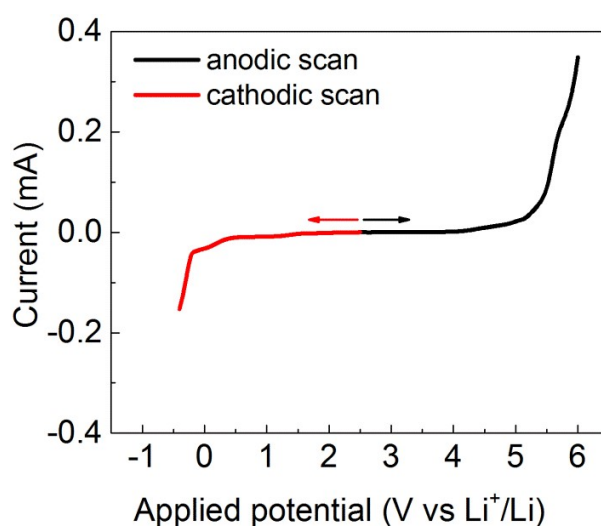


Figure 2-20 Linear sweep voltammetry of POSS-IL-LiTFSI (1 mV/s) at 25 °C.

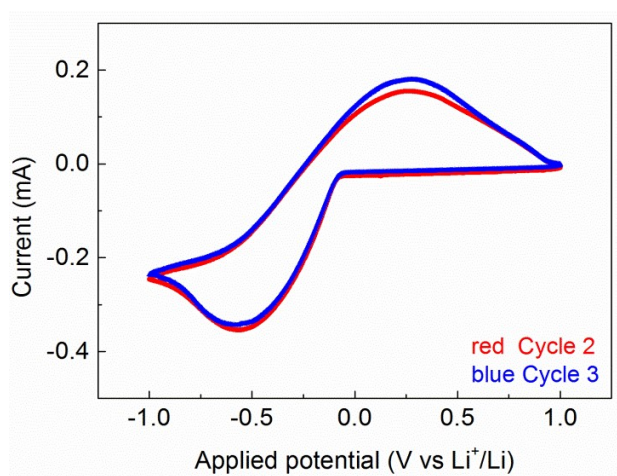


Figure 2-21 Cyclic voltammetry profiles of Li/POSS-IL-LiTFSI/Li symmetrical cell (1 mV/s) at 25 °C.

In order to study the lithium deposition stability of Li/Li symmetrical cell in the presence of POSS-IL-LiTFSI electrolyte, galvanostatic cycling (strip/plate) test was carried out. Constant current (0.05 mA/cm^2) was applied on the cell and reversed every hour. The negative potential value represents Li plating and positive potential value represents Li stripping. From the plot

shown in Figure 2-22, the overpotential value increased at the initial period and then stabilized for the rest of time until at least the 440th hour. The initial increase of potential indicated the increase of internal resistance that may be related to the thickening of SEI layer.¹⁵⁴ Then the overpotential stabilized gradually. No short circuit was observed for at least 600 hours. In contrast, cell using liquid electrolyte (1 M LiTFSI in EC-DMC) showed unstable overpotential profile (Figure 2-23). The results proved the good cycling stability of POSS-IL-LiTFSI against lithium. Figure 2-24 shows the surface morphology of the lithium foils disassembled from button cells after the strip/plate tests above. It can be seen that the lithium electrode surface using POSS-IL-LiTFSI electrolytes after 440h of cycling had sporadic lithium deposits and is much smoother than the lithium surface using liquid electrolyte after 40 h of cycling which had clear and large dendrite indicating uneven lithium deposition.

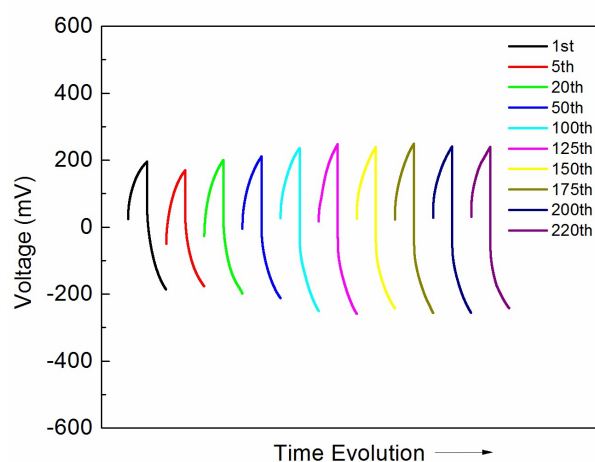


Figure 2-22 Selected galvanostatic stripping/plating cycles of Li/Li symmetrical cells with POSS-IL-LiTFSI at a current density of 0.05 mA/cm². (each cycle includes 1 h stripping and 1 h plating)

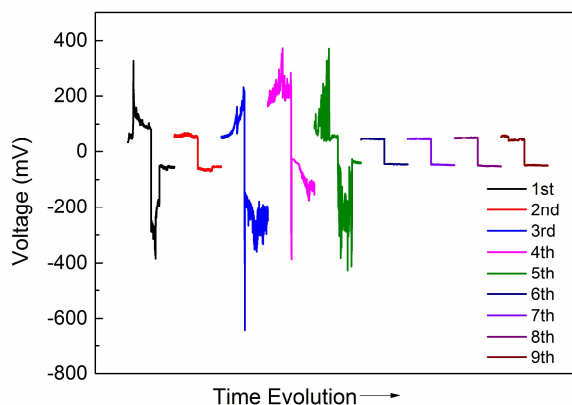


Figure 2-23 Selected galvanostatic stripping/plating cycles of Li/Li symmetrical cells with 1 M LiTFSI in EC/DMC (1:1, v/v) at a current density of 0.05 mA/cm^2 . (each cycle includes 1 h stripping and 1 h plating)

Figure 2-24 The surface morphology of the lithium foil after stripping/plating test characterized by SEM. Left) POSS-IL group after 440-h cycling. right) 1 M LiTFSI in EC/DMC (1:1, v/v) group after 40-h cycling.

A complementary, more aggressive method to study lithium deposition stability and cell life time is unidirectional galvanostatic polarization. In this measurement, lithium was continuously stripped from one electrode and deposited on the other electrode at constant current density until the failure of the cell either by consumption of all lithium or by short circuit caused by dendrite proliferation. The cell lifetime could be estimated by the time when sudden drop of the cell

happened. As can be seen in Figure 2-25 and Figure 2-26, at current density of 0.05 mA/cm^2 , the Li/POSS-IL-LiTFSI/Li cell clearly showed longer operation time than Li/1 M LiTFSI EC: DMC /Li cell. These results confirmed that Li/POSS-IL-LiTFSI/Li cell is much better than Li/1 M LiTFSI EC: DMC/Li in terms of lithium electrochemical deposition.

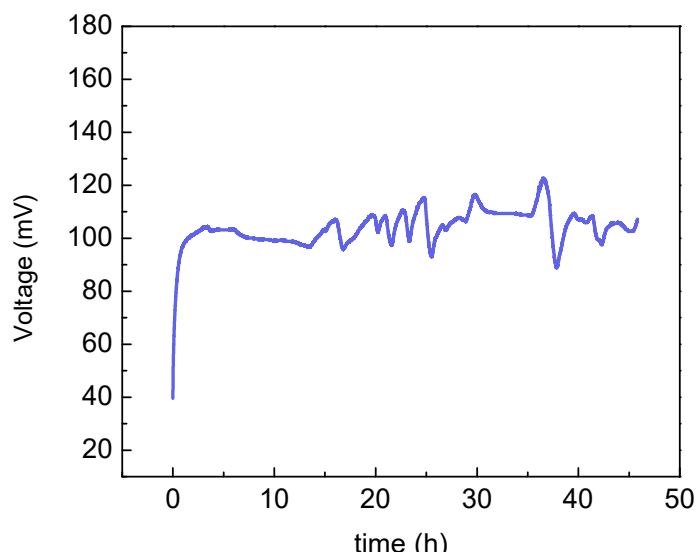


Figure 2-25 Galvanostatic polarization of Li/POSS-IL-LiTFSI/Li cells at current density of 0.05 mA/cm^2 .

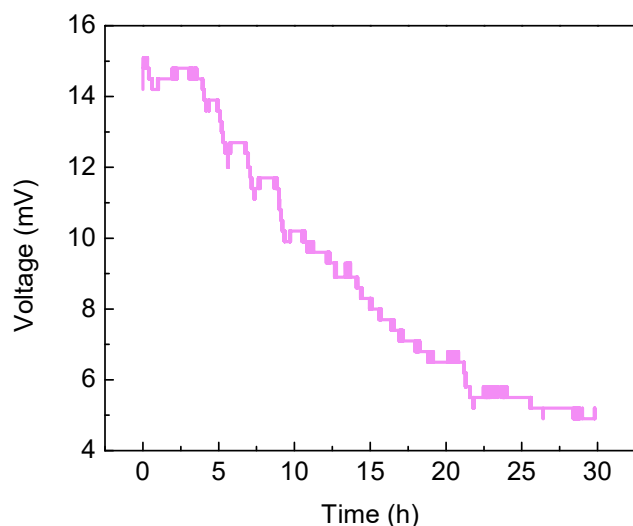


Figure 2-26 Galvanostatic polarization of Li/1 M LiTFSI-EC/DMC/Li cell at current density of 0.05 mA/cm^2 .

Standard Li/LTO coin cells with POSS-IL-LiTFSI as electrolyte were assembled to study the suitability of POSS-IL-LiTFSI in lithium batteries. The coin cells were cycled between 1.3 V and 2 V at 0.1 C, 60 °C. From the voltage profiles in Figure 2-27, well-defined charge/discharge plateaus around 1.55 V vs Li/Li⁺ due to two-phase Li insertion/extraction could be observed (from Li₄Ti₅O₁₂ to Li₇Ti₅O₁₂).¹⁶⁴ Also, the charge/discharge plateaus showed small overpotential (<0.1 V) indicating fast Li⁺ transport in POSS-IL-LiTFSI. The overpotential is generally contributed by charge-transfer overpotential at the electrodes, ohmic overpotential (electrolyte resistance, electrode and current collector resistance induced), and concentration polarization.¹⁶⁵ From Figure 2-28 shows the galvanostatical cycling performance of Li/POSS-L-LiTFSI/LTO cell at 0.1 C. The initial discharge capacity was 165.2 mA·h/g which was close to theoretical value. The cell could deliver discharge capacity of 159.3 mA·h/g at 100th cycle, which showed 96.4% of capacity retention. At 200th cycle, discharge capacity still reached 157.9 mA·h/g indicating 95.6% of capacity retention. This excellent cycling stability of Li/POSS-IL-LiTFSI/LTO cell reflects good interfacial stability and compatibility between electrolyte and electrodes.⁹² The discharge capacity of the battery at different rates from 0.1 C to 1 C vs cycle number is shown in Figure 2-29. The discharge capacity decreased from average 164.7 mA·h/g at 0.1 C to average 126.5 mA·h/g at 1 C (160.2 mA·h/g at 0.2 C, 146.6 mA·h/g at 0.5 C). The inset graph shows the first charge and discharge curve at each rate. The polarization effect and increased interfacial resistance at high rate which caused slower Li⁺ diffusion lead to reduced capacity. The rising of charge plateau and declining of discharge plateau with increased rate resulted from increased battery internal resistance.¹⁶⁶ For example, the overpotential only increased 0.042 V to 0.078 V from the 1st cycle to 100th cycle. After that the overpotential almost showed no further increase. To further study the usefulness of POSS-IL-LiTFSI in LIBs at lower temperature, Li/POSS-IL-LiTFSI/LTO cells were also tested at 25 °C. As can be seen in Figure 2-30a, the discharge capacity of the first cycle at 0.1 C was 159.6 mA·h/g. Compared with the

charge/discharge curves shown in Figure 2-27, larger IR drop at 25 °C compared with 60 °C indicates higher battery resistance.^{53, 119} For example, the overpotential is 0.085 V for the 1st cycle. The overpotential did not show further increase throughout the cycles. The cycling performance results showed that at 70th cycle, discharge capacity of 154.5 mA·h/g could be obtained demonstrating 96.8% of capacity retention. The rate performance data (Figure 2-30b) shows that the discharge capacity at 0.5 C rate (99.1 mA·h/g) was about 65 % of the capacity at 0.1 C (153.6 mA·h/g). The discharge capacity recovered when the C-rate came back to 0.1 C.

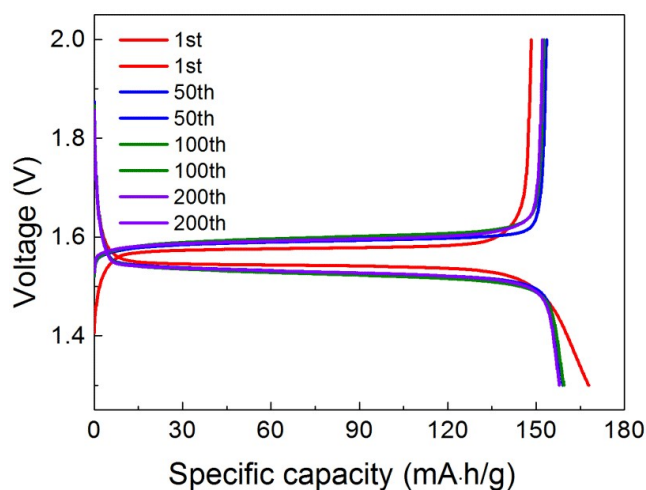


Figure 2-27 Voltage vs Specific capacity profile of a galvanostatic charge-discharge cycling of Li/LTO cell at 0.1 C rate, 60 °C (17 mA/g).

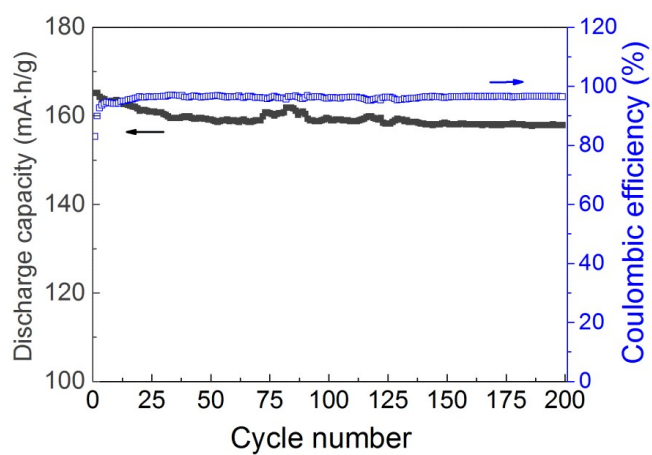


Figure 2-28 Cycling stability of Li/LTO cell at 0.1 C, 60 °C.

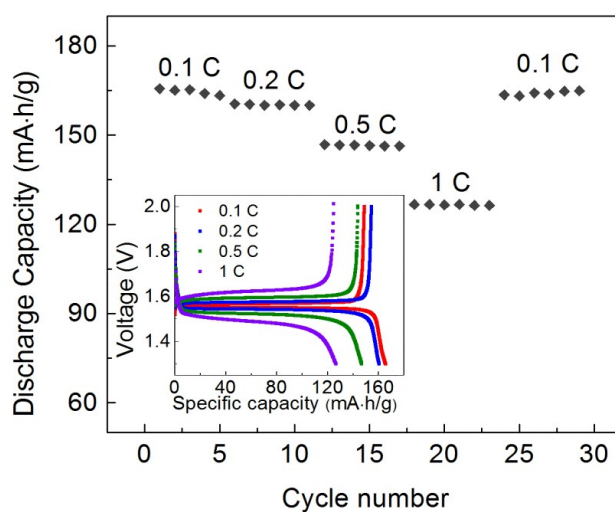


Figure 2-29 Rate capability of Li/POSS-IL-LiTFSI/LTO cell at 60 °C (inset graph: charge/discharge curve at different rates).

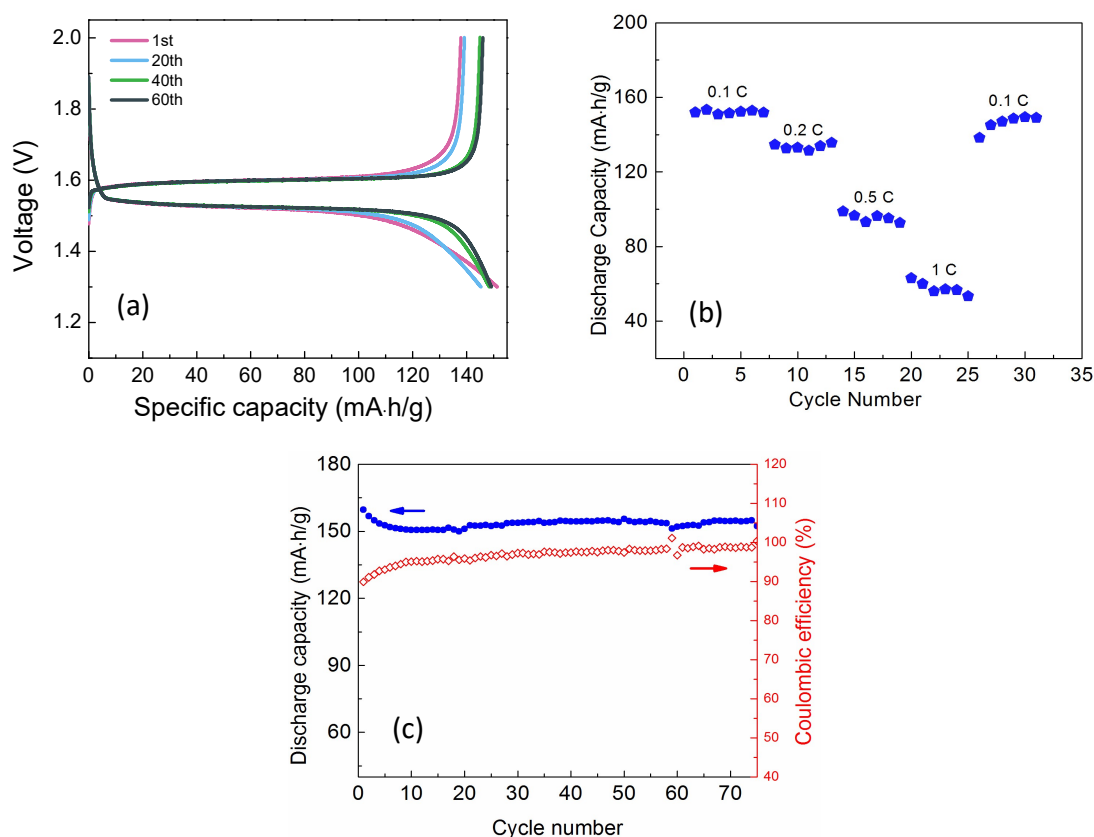


Figure 2-30 a) Typical voltage vs Specific Capacity profile of a galvanostatic charge-discharge cycling of Li/POSS-IL-LiTFSI/LTO cell at 0.1 C. b) Rate capability of Li/POSS-IL-LiTFSI/LTO cell. c) Cycling stability test of Li/POSS-IL-LiTFSI/LTO cell at 0.1 C. All tests were under 25 °C.

Cathode material LFP which has higher electrode potential (3.5 V vs Li/Li^+) was also selected for the Li/POSS-IL-LiTFSI/LFP coin cells assembly. In Figure 2-31a, the Li/POSS-IL-LiTFSI/LFP cells showed clear charge/discharge potential plateaus near 3.45 V (vs Li/Li^+) which were commonly observed for Li/LFP batteries.^{53, 107} The coulombic efficiency was around 99.3% except for the first cycle (94.6%) (Figure 2-31b). The rate performance data (Figure 2-31c) showed that the discharge capacity at 0.1 C was quite close to the value at 0.2 C. The discharge capacity at 0.5 C (115 mA·h/g) was about 76.1 % of the average capacity at 0.1 C (151 mA·h/g). These results are quite impressive because there have been only a few research works reporting

that solvent free polymer electrolyte could successfully support the cycling of lithium secondary batteries at ambient temperature.^{104, 106, 107, 166} In contrast, the Li/POSS-PEO-LiTFSI/LFP batteries could not work at 25 °C mainly due to the low σ of the electrolyte (Figure 2-32). At 60 °C, the capacity delivered was much lower than that of Li/POSS-IL-LiTFSI/LFP cells and faded rapidly probably resulting from low σ and increasing battery internal resistance. This further revealed the advantage of POSS-IL-LiTFSI as promising LIB solid electrolyte candidate. Table 2-2 compares the ionic conductivities, interfacial resistances, and discharge capacities reported in the literatures with current work.

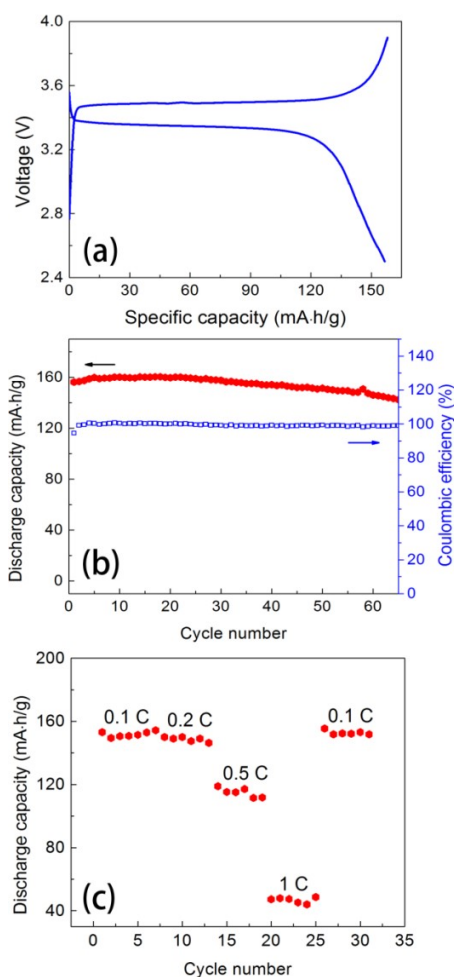


Figure 2-31 Battery performance of Li/POSS-IL-LiTFSI/LiFePO₄ cell at 25 °C. a) charge and discharge voltage profiles at 0.1 C. b) cycling stability at 0.1 C. c) rate capability test.

Figure 2-32 Cycling stability test of Li/POSS-PEO-LiTFSI/LFP at 60 °C, 0.1 C.

Table 2-2 Properties of solvent-free polymer electrolyte reprinted in literature.

Entry	Electrolyte	Conductivity (S/cm)	Interfacial impedance (Ω)	Discharge capacity (mAh/g)	Ref.
1	POSS-PEG/Poss-benzy7(BF3Li3)	2.5e-4 at 30 °C	200-550 at 80 °C		94
2	POSS-PEG/MC	1.6e-5 at 30 °C	3000-9000 at 50 °C		101
3	POSS-PEO/PEO	8e-6 at R.T.			43
4	Crosslinked POSS/PEO	9.5e-5 at 30 °C		160 (90 °C), Li/LFP, C/5	167
5	AI-PEO/PEGMA	More than 10 ⁴ at R.T.	150 at 60 °C	125 (60 °C), Li/LFP, 1C	92
6	Poly(ionic liquid)	1.35e-4 at 30 °C			
7	Organic/inorganic	1.6 e-4 at 30 °C	1200 at 60 oC		41
8	Comb like PEO	10e-5 at R.T.		146 (80 °C), Li/LFP, C/24	82
9	Single ion DADS	3.96 e-4 at R.T.		140 (25 °C), Li/LFP, 0.1 C	168
10	N-PCPE	5.7e-4 at 30 °C		128 (R.T.), LCO/LFP	104
11	Single ion +PVDF-HFP	6e-4 at R.T.	200-1200 at 80 C	130 R.T., Li/LFP, 0.1 C	169
12	PFPE-DMC	8e-5 R.T.		120 (30 °C), Li/NMC, 0.1 C	106

13	PMA/PEG+SIO ₂	2.6e-4 R.T.		Different electrode	170
14	Graft polymer	over 1e-4 at R.T.	2000-3000 at R.T.	Over 130 at R.T., Li/LFP, C/17	87
15	poly(allyl glycidyl ether) (PAGE)	3e-5 at R.T.			171
16	organic-inorganic solid polymer electrolyte	1e-4 at 30 °C			172
17	Poly(ionic liquid)	1e-5 at R.T.			153
18	PEO/LiBOB			156.8 (80°C), Li/LFP, 0.1 C	86
19	poly(ϵ -caprolactone) /tmc	4 e-5 at R.T.		132 (40 °C), Li/LFP, 0.1 C	173
20	PEO graft on ceramic	4e-5 R.T.		125 (70 °C), Li/LFP,C/2	88
21	POSS-PEO/graphene	2e-4 at R.T.			174
22	IPN	5e-4 at 30			85
23	This work	4.8e-4 at 25 °C		151 (25 °C), Li/LFP, 0.1C	

2.3.5 Flammability test

Ignition test was carried out to confirm the non-flammability of POSS-IL-LiTFSI. The results were shown in Figure 2-33. No flame was observed in the POSS-IL-LiTFSI group, only some yellow marks appeared when the bottom edge was heated up. This was because the POSS-IL-LiTFSI could not be easily ignited. In comparison, 1 M LiTFSI EC/DMC group was quite flammable and once ignited the flame did not extinguished even after the microtorch was turned off indicating the serious safety issue of traditional liquid electrolyte. The flammability test proved the non-flammability of POSS-IL-LiTFSI showing its applicability for safe lithium ion battery.

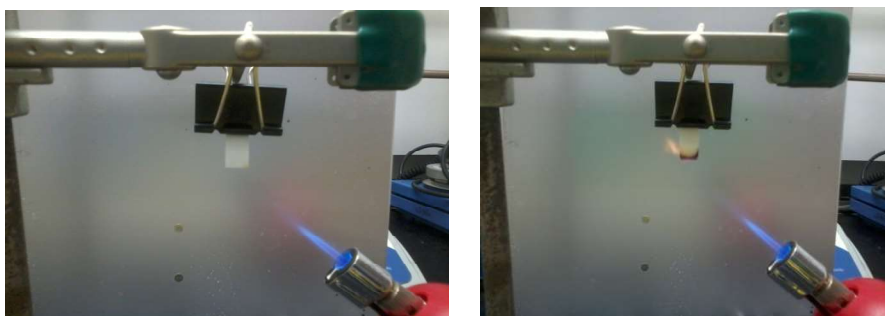


Figure 2-33 Flammability test of left) POSS-IL. right) 1 M LiTFSI in EC/DMC

2.4 Conclusion

In summary, we proposed and successfully synthesized solid polymer electrolyte (POSS-IL) based on dense ILs and oligomeric PEG functionalized POSS that enriches the library of ion-containing polymer electrolytes for LIBs. This thermal stable hybrid electrolyte POSS-IL-LiTFSI showed high σ at room temperature (0.48 mS/cm) as well as great electrochemical stability limit (up to 5 V vs Li/Li⁺). POSS-IL-LiTFSI also proved its ability to support lithium ion batteries to operate at room temperature. The stable electrodeposition of lithium further indicated that POSS-IL-LiTFSI had good interfacial compatibility with lithium metal. Li/LTO and Li/LFP batteries employing POSS-IL-LiTFSI as electrolyte demonstrated high specific capacity and good cycling stability at room temperature or 60 °C. These results indicate that POSS-IL-LiTFSI is a promising candidate of solvent free polymer electrolyte for next-generation LIBs.

Chapter 3

Dumbbell-Shaped Octasilsesquioxane Functionalized with Ionic Liquids as Hybrid Electrolytes for Lithium Metal Batteries

3.1 Introduction

Lithium ion batteries (LIBs) have been gaining intense attention owing to their broad applications in portable electronics (such as cell phones, laptops) and electric vehicles.^{5,6,175} Although the use of lithium as anode to replace the conventional graphite anode is very promising because lithium metal has significant higher theoretical capacity (3860 mA·h/g) and low redox potential (-3.04 V),^{170,176} there exists a serious safety issue arisen from liquid electrolyte that needs to be addressed before large capacity lithium metal batteries can be trusted for electrifying our daily life. The currently available organic, liquid carbonate electrolytes need to be substituted by safer electrolytes to prevent unexpected battery accidents such as leakage, combustion and explosion, etc. Additionally, the liquid electrolytes are not able to interfere with formation and growth of the lithium dendrite. Consequently, the replacement of graphite anode with much higher capacity lithium metal anode is severely hindered.^{20,49} As important alternatives of liquid electrolyte, solid polymer electrolytes are easy to process and leakage-free.^{27,40} The ideal features for solid state electrolytes include excellent chemical and electrochemical stability, facile processability, good compatibility with electrodes, inexpensiveness, and satisfactory mechanical properties in addition to sufficiently high ionic conductivities. Achieving these properties concurrently is a great challenge toward unveiling the broader applications of LIBs.

The study of all solid-state polymer electrolytes dates back to 1970s when noticeable ionic conductivities of poly(ethylene glycol) (PEO)/Na⁺ system were realized by pioneer researchers

Wright and Armand.^{39, 177, 178} However, despite of decades of intensive efforts, the ionic conductivities of PEO based solid electrolytes are usually lower than 10^{-6} S/cm at ambient temperature. Therefore, for the lithium polymer batteries operating at room temperature, a certain amount of liquid electrolytes or organic solvents have to be introduced to the polymer host to boost the room-temperature ionic conductivity.^{3, 179}

More recently, extensive efforts have been placed on plasticizing polymer electrolyte with non-volatile and non-flammable molecules,^{119, 180} improving the ion transport by creating ion conduction channel in the copolymers,^{67, 90} incorporating inorganic nanoparticles to form composite electrolytes,^{38, 181} and developing other alternative polymeric materials with desired electrochemical properties.^{104, 106} In particular, ionic liquids (ILs) have been intensively investigated as electrolytes or solvents for electrochemical energy devices.¹⁴⁵ For example, imidazolium-based ILs possesses low viscosity, good thermal stability, and high ionic conductivity ($> 10^{-3}$ S/cm).^{113, 138, 152} ILs can either function as plasticizers for polymer electrolytes or serve as monomers to be polymerized as poly(ionic liquid) electrolytes. Cations or anions of ILs have also been covalently bonded to polymer backbone or side chain structures as electrolytes.^{137, 182, 183} Unfortunately, most of the IL-grafted polymers and inorganic particles still show unacceptably low conductivities (less than 10^{-5} S/cm at room temperature in most cases) when considered as ion transport medium for LIBs.

In this work, we describe the synthesis and characterization of a dumbbell-shaped organic-inorganic hybrid electrolyte (CPOSS-IL) based on polyhedral oligomeric silsesquioxane (POSS) grafted with IL side chains. POSS with an inorganic $(\text{SiO}_{1.5})_n$ ($n=6, 8, \text{ or } 10$) cage and organic functional groups located at the corners of the cage is a versatile building block for organic-inorganic hybrids and polymer nanocomposite.¹⁸⁴ PEO has been combined with POSS to form the linear, star shaped and crosslinked hybrid polymer electrolytes. More recently, we have reported a hybrid dendritic-like electrolyte derived from ionic liquid grafted POSS, which exhibits

outstanding ionic conductivities and electrochemical properties.¹⁸⁵ Herein, by using methylene diphenyl diisocyanate as a linker, two monohydroxylated POSS molecules were coupled followed by subsequently attaching ILs onto peripheral of POSS. An impressively high ionic conductivity of 1.2×10^{-4} S/cm has been obtained from the prepared hybrid electrolyte measured at room temperature. Meanwhile, the electrolyte exhibits good electrochemical stability and the ability to support stable lithium deposition. Moreover, it is found that the all-solid-state Li battery cells fabricated from the prepared electrolyte deliver high capacities at room temperature.

3.2 Experimental

3.2.1 Materials

Octavinyl polyhedral oligomeric silsesquioxane (OVPOSS) was purchased from Hybrid Plastics (>97%), dried at 60 °C overnight before use. Triflic acid (Aldrich, 98%). Sodium carbonate (ACS grade, EMD). Sodium sulfate (ACS grade, EMD). Mono-hydroxyl heptavinyl substituted POSS (VPOSS-OH) was synthesized according to the reported method¹⁸⁶. 4,4'-methylene bis(phenyl isocyanate) (MDI, 98%, Aldrich). 1,1,3,3-tetramethyldisiloxane (97%, Aldrich). Dibutyltin dilaurate (95%, Aldrich). Anhydrous dichloromethane (DCM) and anhydrous toluene were purchased from Aldrich. Ethyl acetate (EtOAc, ACS grade, EMD). Karstedt catalyst solution in xylene (2%, Aldrich). 1-butyl imidazole (98%, Aldrich). lithium bis(trifluoromethanesulfonyl) imide (LiTFSI, Aldrich).

3.2.2 Synthesis of CPOSS

In a 100 mL flask with a magnetic stir bar, VPOSS-OH (0.48 g, 0.74 mmol) and MDI (92.5 mg, 0.37 mmol) dissolved in anhydrous toluene (40 mL) were added under the protection of nitrogen atmosphere at room temperature. The reaction mixture was heated up to 90 °C and 15 μ L of dibutyltin dilaurate was added to the solution. The reaction was kept for 5 h and toluene was evaporated under reduced pressure. Yellow powder was obtained after drying under vacuum at 60 °C. ^1H NMR (300 MHz, 25 °C, CDCl_3) δ : 7.12 (m, protons from the MDI aromatic ring), 3.90 (s, $-\text{C}-\underline{\text{CH}_2}-\text{C}-$), 4.30 (s, $\text{Si}-\text{CH}_2-\underline{\text{CH}_2}-\text{O}-$), 0.86 (s, $\text{Si}-\underline{\text{CH}_2}-\text{CH}_2-\text{O}-$), 1.29 and 1.59 (protons from catalyst). ^{13}C NMR (CDCl_3) δ : 153.4 ($-\text{N}-\underline{\text{C}}\text{OO}-\text{CH}_2-$), 136.6, 136.4, 136.2, 136.1, 136.0, 130.1, 130.0, 129.6, 129.4, 129.3, 121.7, 118.9, 61.4 ($-\underline{\text{CH}_2}-\text{O}-\text{CO}-$), 40.63 ($\text{C}-\underline{\text{CH}_2}-\text{C}$), 14.1 ($-\text{Si}-\underline{\text{CH}_2}-$). FTIR (KBr, cm^{-1}): 1734 (v, $\text{C}=\text{O}$), 1091 (v, Si-O-Si). 1526 (δ , N-H bending).

3.2.3 Synthesis of 17-bromo-3,6,9,12,15-pentaoxaheptadecan-1-ol

Hexaethylene glycol (5 g, 17.71 mmol), triphenyl phosphine (2.33 g, 8.86 mmol) were dissolved in 25 mL dichloromethane in a 100 mL flask. The solution was purged with N_2 for 40 min before CBr_4 (2.935 g, 8.86 mmol) was added. The reaction mixture was stirred for 4 h at room temperature. Then the solvent was evaporated under vacuum and the crude product was purified by column chromatography with chloroform/methanol eluent (95:5, v/v). The final product was obtained as slight yellow oil. (81% yield) ^1H NMR (CDCl_3) δ : 3.16 (s, $-\underline{\text{OH}}$), 3.46 (t, $-\underline{\text{CH}_2}-\text{Br}$), 3.58-3.68 (m, $-\text{O}-\underline{\text{CH}_2}-$), 3.79 (t, $-\underline{\text{CH}_2}-\text{CH}_2-\text{Br}$); ^{13}C NMR (CDCl_3) δ : 30.1, 61.6, 70.2-70.7 (br), 73.0 ($-\underline{\text{CH}_2}-\text{CH}_2-\text{Br}$).

3.2.4 Synthesis of vinyl tris(17-bromo-3,6,9,12,15-pentaoxaheptadecan-1-yl) silane (1)

17-bromo-3,6,9,12,15-pentaoxaheptadecan-1-ol (2.8 g, 0.008 mol) and triethylamine (1.6 g, 0.016 mol) was dissolved in 40 mL toluene in a 100 mL flask with magnetic stirrer. In an inert N₂ atmosphere, trichlorovinylsilane (0.437 g, 2.67 mmol) was added at room temperature. The reaction lasted for 3 h at ambient temperature before 50 mL of EtOAc was added to dilute the reaction mixture. After washed with water and dried over Na₂SO₄. The organic layer was concentrated and dried under vacuo overnight to give the final product. (84 % yield) ¹H NMR (CDCl₃) δ: 3.43 (t, -CH₂-Br), 3.58-3.68 (m, -O-CH₂-), 3.79 (-O-CH₂-CH₂-Br), 3.89 (t, -Si-O-CH₂-), 5.9-6.1 (m, CH₂=CH-Si-), ¹³C NMR (CDCl₃) δ: 30.1, 62.4 (-Si-O-CH₂), 70.8-71.9 (signal overlap), 72.7 (-CH₂-CH₂-Br), 137.4 (CH₂=CH-Si-).

3.2.5 Synthesis of 2

To a solution of **1** (1 g, 0.92 mmol) dissolved in anhydrous toluene (10 mL) in a 50 mL flask equipped with a magnetic stir bar, 0.616 g (4.6 mmol) of 1,1,3,3-tetramethyldisiloxane was added at room temperature. Then Karstedt catalyst solution in xylene (15 μL) was added. The solution was stirred for 2 days at 60 °C under nitrogen protection. Then the solvent and unreacted 1,1,3,3-tetramethyldisiloxane was then removed under reduced pressure to give light yellow oil. ¹H NMR (CDCl₃) δ: 3.46 (t, -CH₂-Br), 3.58-3.68 (m, -O-CH₂-), 3.80 (t, -O-CH₂-CH₂-Br); 0.08 (s, -Si-CH₃). ¹³C NMR (CDCl₃) δ: 72.5 (-O-CH₂-CH₂-Br), 70.2-70.6 (signal overlap), 61.6 (-Si-O-CH₂-CH₂-), 30.4 (-O-CH₂-CH₂-Br), 0.2, -0.7 (-OSi(CH₃)₂-H), 0.65 (-Si(CH₃)₂-O-).

3.2.6 Synthesis of CPOSS-PEO

To a solution of **2** (1g, 0.8 mmol) dissolved in anhydrous toluene (10 mL) in a 50 mL flask, CPOSS (0.09g, 0.057 mmol) was added at room temperature. The solution was purged with N₂ for 40 min before Karstedt catalyst was added. The reaction proceeded for 2 days at 60 °C and the solvent was evaporated under reduced pressure to give yellow material. ¹H NMR (CDCl₃) δ: 3.46 (t, -CH₂-Br), 3.58-3.68 (m, -O-CH₂-), 3.80 (t, -CH₂-CH₂-Br); 0.08 (s, -Si-CH₃).

3.2.7 Synthesis of CPOSS-IL

CPOSS-PEO (0.8g, 0.042 mmol) was dissolved in 15 mL anhydrous acetonitrile (ACN) in a 50 mL flask followed by adding 1-butyl imidazole (223 mg, 1.8 mmol) to the solution. The reaction mixture was stirred in 50 °C for 12 h and LiTFSI was added. After removing of the ACN, the product was redissolved in DCM and the solution was filtrated and concentrated to give light brown material. ¹H NMR (CDCl₃) δ: 0.08 (s, -Si-CH₃); 0.99 (t, -CH₂-CH₃); 1.38 (m, -CH₂-CH₂-CH₃); 1.88 (m, -CH₂-CH₂-CH₃); 3.58-3.69 (m, -O-CH₂-); 4.29 (t, O-CH₂-CH₂-N-); 4.65 (t, -N-CH₂-CH₂-); 7.78 (s, -N-CH=CH-N-); 10.26 (s, -N=CH-N-). FTIR (KBr, cm⁻¹): characteristic bands for TFSI: 1352, 1195, 1135, 1056. 1565 (v, C=N).

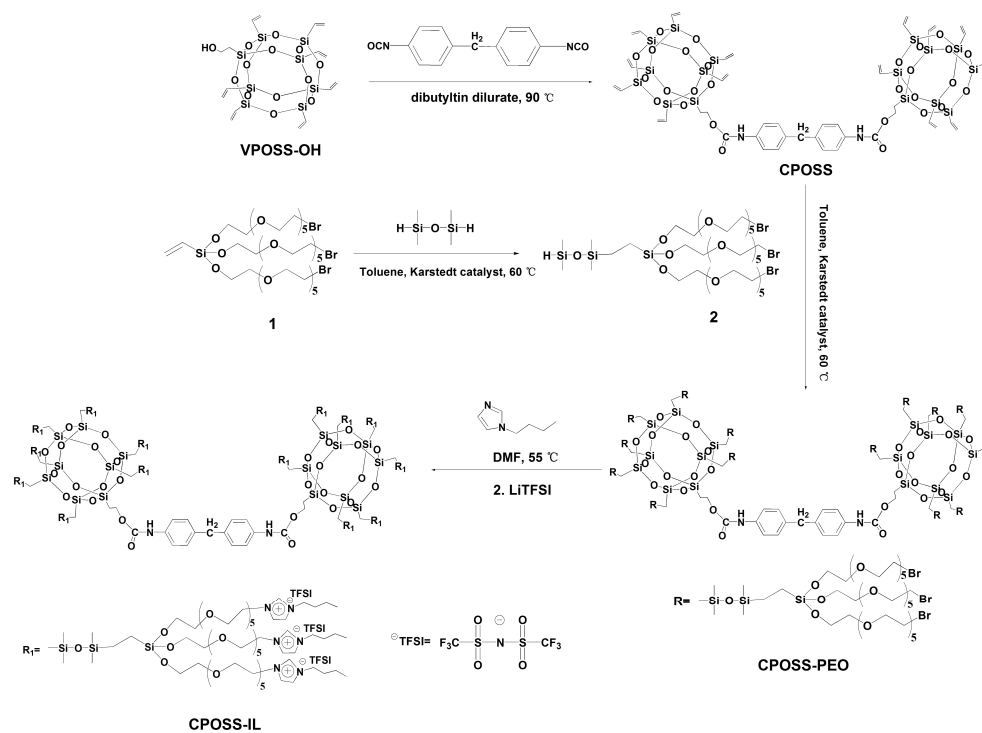
3.2.8 Characterization Methods

¹H NMR and ¹³C NMR tests were carried out on a Bruker AM-300 nuclear magnetic resonance spectrometer. Fourier transform infrared (FTIR) spectra were obtained using Bruker Vertex 70 spectrometer. Differential scanning calorimetry (DSC) was performed on TA Q100 DSC instrument at a heating and cooling rate of 10 °C/min from -85 to 30 °C. Thermogravimetric

analysis (TGA) was performed on TA Instrument model Q50 at a heating rate of 10 °C/min under N₂ from 25- 650 °C. X-ray Diffraction (XRD) was performed on a Rigaku DMAX-Rapid Microdiffractometer using CuK_α radiation. The software routines were used to evaluate the scattering intensity as a function of the diffraction angle, 2θ, in the range of 4°-30°.

The ionic conductivity (σ) of the polymer electrolyte samples was analyzed by electrochemical impedance spectroscopy (EIS). Samples were sandwiched between two stainless steel (SS) blocking electrodes separated by a teflon o-ring spacer (125 μm thick). Criterion Temperature Bench-top Chamber was used to simulate environmental temperature. The ionic conductivity was calculated based on $\sigma=L/R_bS$, σ is the ionic conductivity (S/cm), L is the polymer electrolyte thickness, R_b is the bulk resistance and S is the contacting area (0.785 cm²). Cell impedance values were obtained on Solatron 1260 impedance/gain phase analyzer over the frequency range from 1 MHz to 100 mHz. The Li⁺ ion transference number (t_{Li^+}) was measured by combined DC polarization and AC impedance method (1 MHz to 100 mHz, 20 mV DC potential). t_{Li^+} was calculated according to method reported by Bruce and Vincent⁸⁰ (a combination of AC impedance and DC polarization measurements) which has been used for the determination of t_{Li^+} of polymer-IL-Li salt system.^{115, 149, 150} A very small dc pulse was applied to the Li/Li symmetrical cell and the initial current and steady state current was measured. Also, to consider the resistance of the passivation layers before and after the polarization, the same symmetrical cell was subjected to AC impedance test. The equation can be written as $t_{\text{Li}^+} = I_{\text{ss}}(\Delta V - I_0 R_0) / I_0(\Delta V - I_{\text{ss}} R_{\text{ss}})$. I_0 and I_{ss} are initial and steady state current. R_0 and R_{ss} are initial and steady state resistance. ΔV is the DC pulse voltage to polarize the cell. A DC voltage of 30 mV was chosen to polarize the cell. Cyclic voltammetry and linear sweep voltammetry (LSV) were performed at room temperature on PAR Potentiaostat/Galvanostat Model 263A with Li/polymer electrolyte/stainless steel 2032 coin cells (stainless steel working electrode and lithium foil counter and reference electrode). Scan rate: 1 mV/s.

For the electrolyte preparation and coin cells assembly, CPOSS-IL was dissolved in anhydrous THF (11% w/v) first. LiTFSI was then weighted and added to the above solution (2 mol of IL tethered PEO chains: 1 mol of LiTFSI). The solution was stirred overnight to let the solvent fully dissolve the salt. LFP cathode was prepared by spreading slurries containing 80 wt% of LFP, 10 wt% of super P, 10% of CPOSS-IL in 1-Methyl-2-pyrrolidone (NMP) onto 15 μm aluminum foil. The dried cathode sheets were punched into 1 cm diameter disks, vacuum dried at 80 $^{\circ}\text{C}$ completely, weighted, and transferred into glove box for coin cell assembly. Lithium foils (MTI, 250 μm thick) were used as the anode. The prepared polymer solution was dropped on the lithium foil and dried under argon atmosphere for 18 h at 65 $^{\circ}\text{C}$. The prototype buttons cell CR2032 was assembled with ring shaped 125 μm thick Teflon ring as spacer. The cell performance tests were completed on a Neware CT-3008 battery tester at constant current and the cut-off voltage was between 2.5 V to 3.9 V vs Li^+/Li .



Scheme 3-1 Synthetic route of CPOSS-IL.

3.3 Result and discussion

3.3.1 Synthesis

The synthetic route for CPOSS-IL is shown in Scheme 1. 4,4'-methylene bis(phenyl isocyanate (MDI) was used as diisocyanate linker for the synthesis of CPOSS. The urethane bonds formation was achieved after the reaction between MDI and VPOSS-OH. Each halogen atom of trichlorovinylsilane acted as coupling site with mono-brominated hexaethylene glycol to produce **1**. With the help of 1,1,3,3-tetramethyldisiloxane as connector, **1** was grafted onto the CPOSS structure. After quaternization reaction of imidazole ring with CPOSS-PEO and anion exchange, CPOSS-IL was obtained. The successful formation of urethane bonds in the CPOSS synthesis step was confirmed by the NMR and FTIR spectra. From the ^1H NMR results shown in Figure 3-2, the proton signal located at chemical shift of 3.90 ppm could be assigned to the protons on the methylene group between the two aromatic rings. The proton signal at 4.26 ppm came from the protons of urethane linkages (-NH-CO-O-) and its carbonyl carbon signal at 153 ppm can be seen in the ^{13}C NMR. Moreover, in the FTIR spectra in Figure 3-8, the formation of the ester carbonyl bond in the -NH-CO-O could be seen at wavenumber of 1734 cm^{-1} . The N-H bending vibration could be seen at 1527 cm^{-1} . The disappearance of stretching vibration of NCO bond at 2280 cm^{-1} from the starting material MDI indicated the completion of reaction. For the synthesis of product **2**, the disappearance of vinyl proton signal at around $\delta 6$ ppm in the ^1H NMR spectrum proved the completion of hydrosilylation reaction (Figure 3-4). From the ^1H NMR spectrum of CPOSS-IL, the significant suppression of $-\text{CH}_2\text{-Br}$ and $-\text{CH}_2\text{-CH}_2\text{-Br}$ proton signals in the CPOSS-PEO structure at $\delta 3.46$ and $\delta 3.80$ indicated the successful coupling of 1-butyl imidazole (Figure 3-7). Also, the characteristic absorbance peaks of TFSI⁻ anions (1352 cm^{-1} ,

1195 cm^{-1} , 1135 cm^{-1} , 1056 cm^{-1}) could be observed in the FTIR spectrum of CPOSS-IL-LiTFSI (Figure 3-9).^{187, 188}

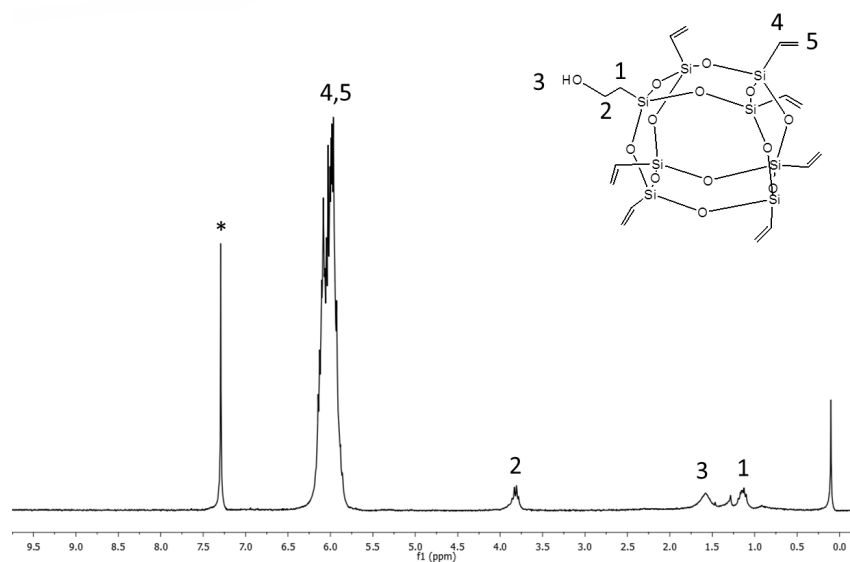


Figure 3-1 ^1H NMR of VPOSS-OH.

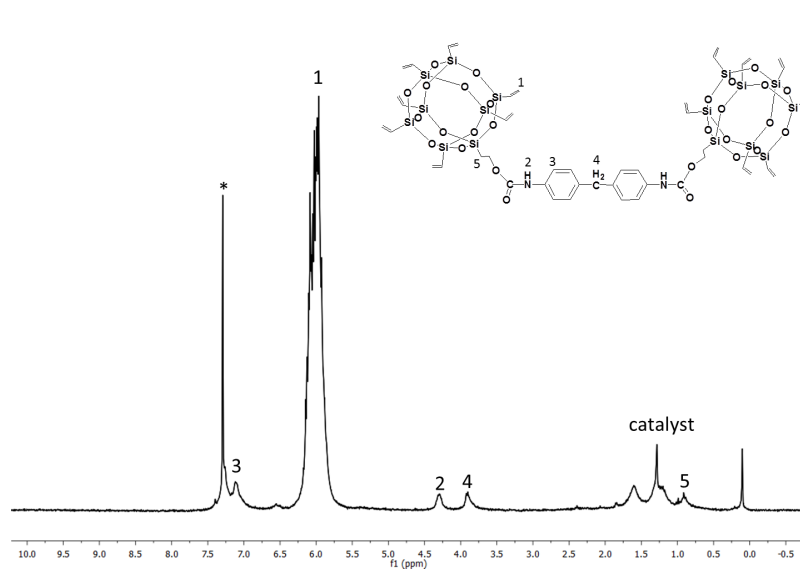


Figure 3-2 ^1H NMR of CPOSS.

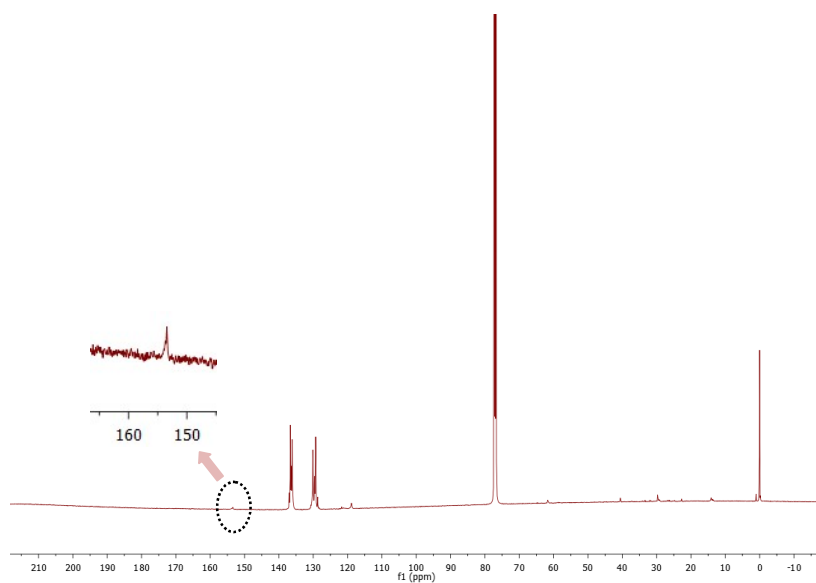


Figure 3-3 ^{13}C NMR of CPOSS.

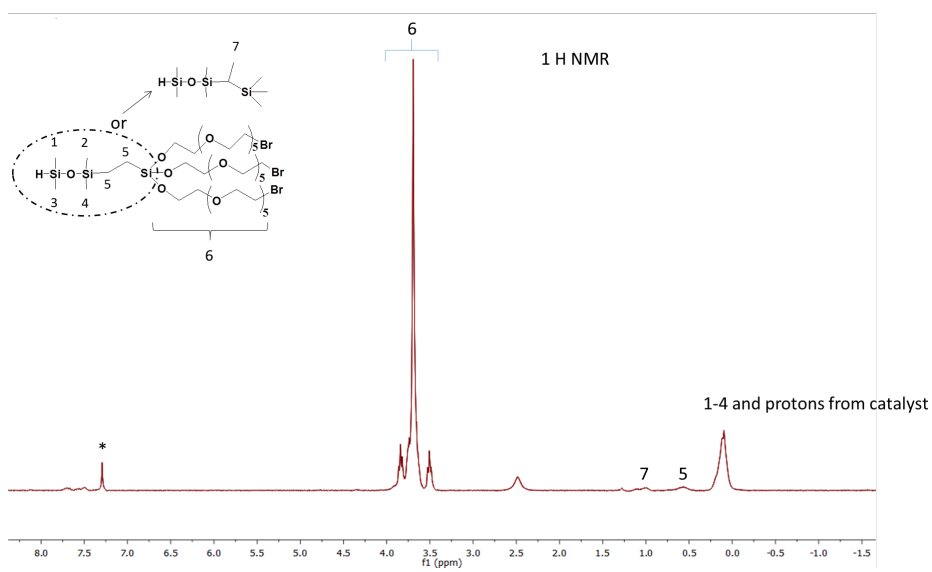


Figure 3-4 ^1H NMR spectrum of 2.

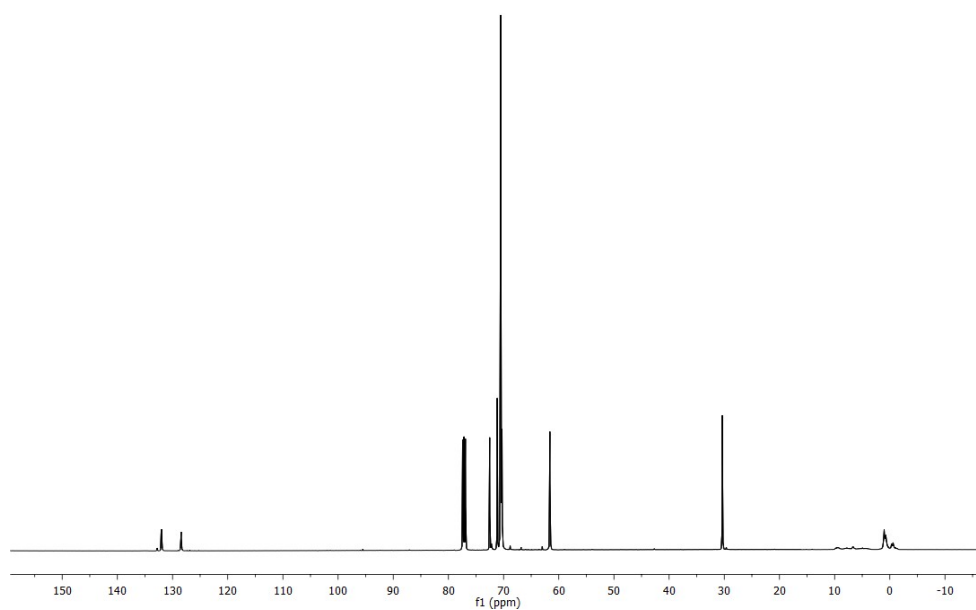
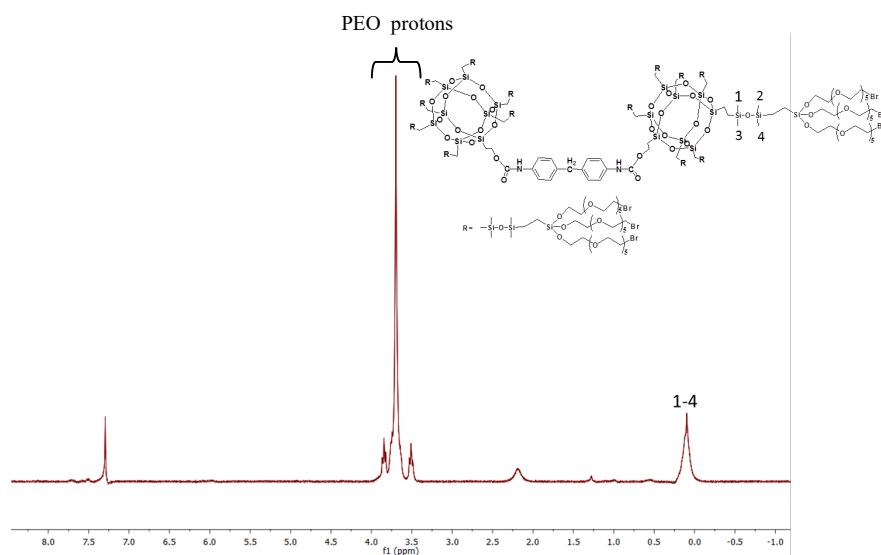
Figure 3-5 ^{13}C NMR spectrum of 2.Figure 3-6 ^1H NMR spectrum of CPOSS-PEO.

Figure 3-7 ^1H NMR spectrum of CPOSS-IL.

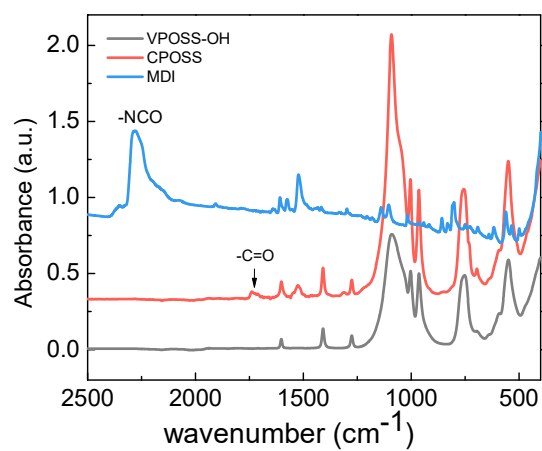


Figure 3-8 FTIR spectra of MDI, VPOSS-OH, and CPOSS.

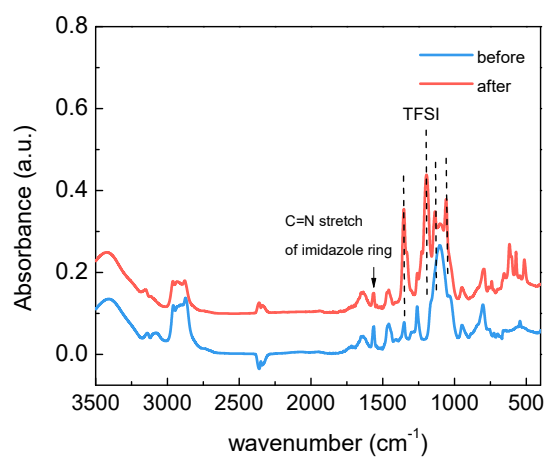


Figure 3-9 FTIR spectra of CPOSS-IL before and after ion exchange.

3.3.2 Thermal properties

The thermal properties of CPOSS-IL-LiTFSI were investigated by DSC and TGA. Figure 3-10 presents the DSC profile from -85 °C to 20 °C. The glass transition temperature (T_g) was found to be -62 °C. No endothermic melting transition was found showing the amorphous nature of the material. Thermal stability is also important because heat can be generated when battery is operating and also battery should be able to work with high environmental temperature. The thermal decomposition temperature was measured by TGA under nitrogen environment from 25 °C to above 500 °C (Figure 3-11). The initial 3 % weight loss before sharp decomposition mainly came from the releasing of preabsorbed moisture.¹⁸⁹ The sharp degradation of CPOSS-IL-LiTFSI was found at around 230 °C, which appears to be higher than both the decomposition temperatures of hEG and OVPOSS. This was probably because CPOSS-IL-LiTFSI had higher molecular weight and the interaction within molecules was stronger than that in hEG and OVPOSS.^{190, 191} CPOSS-IL-LiTFSI showed 75 % weight loss between 230 °C and 500 °C and the remaining char residue is likely to be composed of SiO₂ and decomposed lithium salt.¹⁹² TGA result demonstrates good thermal stability of CPOSS-IL-LiTFSI.

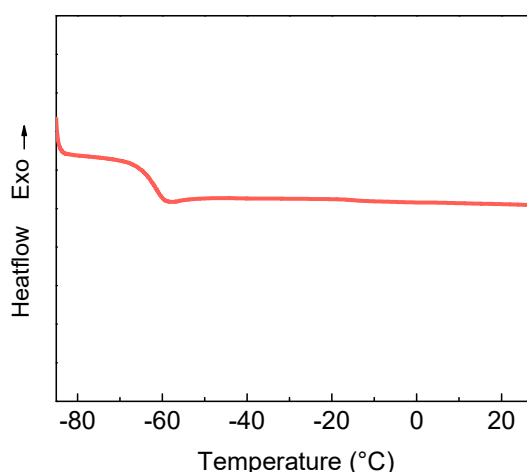


Figure 3-10 DSC curve of CPOSS-IL-LiTFSI.

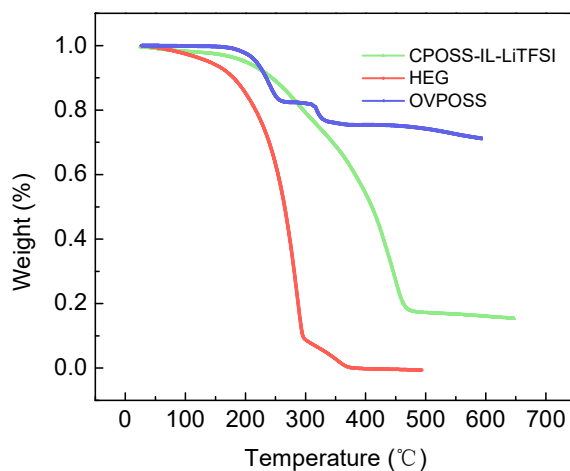


Figure 3-11 TGA curve of CPOSS-IL-LiTFSI, HEG, and OVPOSS.

3.3.3 Microstructural Characterization

The amorphous characteristic of CPOSS-IL was confirmed by X-ray diffraction (XRD). From Figure (3-12), it could be seen that amorphous halo at $2\theta=8.1^\circ$ (d-spacing of 1.1 nm) originated from the inter-distance of POSS. The diffraction peak at $2\theta=20^\circ$ (d-spacing of 0.44 nm) is from the amorphous PEO chain.

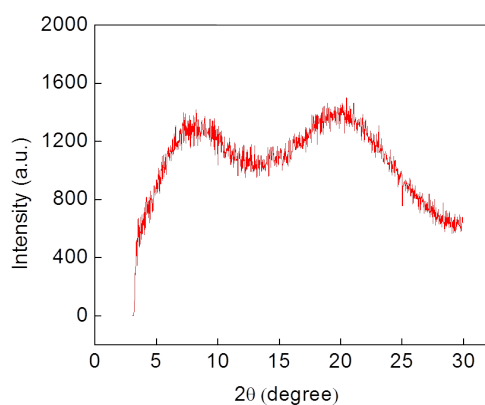


Figure 3-12 XRD pattern of CPOSS-IL-LiTFSI

3.3.4 Ionic conductivity

Ionic conductivity is one of the fundamental parameters to evaluate suitability of polymer electrolytes for battery application. The temperature dependence of the ionic conductivity of CPOSS-IL-LiTFSI and non-ionic liquid tethered CPOSS-PEO-LiTFSI were shown in Figure 3-13. The conductivity value monotonically increased with temperature rising for both groups exhibiting nonlinear fashion. The conductivity data points of the heating up and cooling down process for each group matched very well showing the stability of the ion conduction in the CPOSS-IL-LiTFSI over the temperature range. Note that the ionic conductivity of CPOSS-IL-LiTFSI is significantly higher than that of CPOSS-PEO-LiTFSI, e.g. 1.2×10^{-4} S/cm vs. 5.2×10^{-5} S/cm at 20 °C. This is impressively high for solid-state organic/polymer material.^{92, 106, 129, 193} One reason for the conductivity difference is that the presence of imidazolium cations could associate with TFSI anions through coulombic force to produce more dissociated, mobile Li^+ ions from LiTFSI.^{16, 194}

The data points could be well fitted by Vogel–Tamman–Fulcher (VTF) equation: $\sigma = AT^{-1/2} \exp[-E_a/R(T-T_0)]$. E_a is a constant related to activation energy for ion conduction. A is pre-exponential factor. T_0 is the reference temperature. R is the ideal gas constant. VTF behavior indicates that the ion motion in polymers is correlated to segmental motion of polymer chain above its T_g . The E_a value of CPOSS-IL-LiTFSI fitted by VTF equation was 8.3 kJ mol^{-1} , corresponding to $8.6 \times 10^{-2} \text{ eV}$. The E_a of CPOSS-PEO-LiTFSI is higher (9 kJ mol^{-1} , corresponding to 0.093 eV), indicating larger energy barrier for ion transport compared with CPOSS-IL-LiTFSI. The fitting results are shown in Table 3-1.

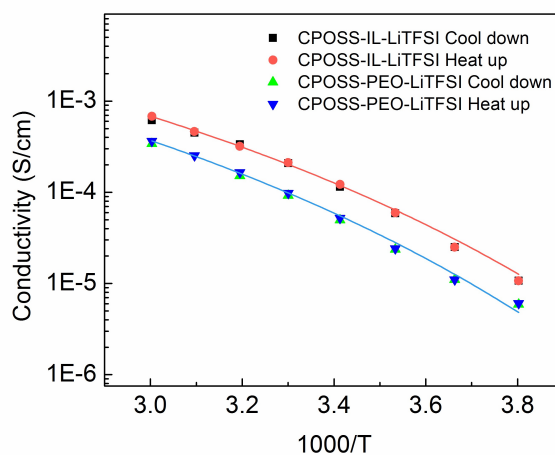


Figure 3-13 Ionic conductivity change with inverse temperature for CPOSS-IL-LiTFSI and CPOSS-PEO-LiTFSI.

Table 3-1 VTF parameters and ionic conductivity.

	σ (20 °C, S/cm)	R-square	B (KJ/mol)	A(S/cm·K ^{1/2})
CPOSS-IL-LiTFSI	1.2×10^{-4}	0.999	8.3	4.3
CPOSS-PEO-LiTFSI	5.2×10^{-5}	0.999	9.0	3.9

3.3.5 Electrochemical properties.

The electrochemical stability of CPOSS-IL-LiTFSI was studied by voltammogram. As shown in Figure 3-14. At the low potential region, clear lithium plate and strip peak could be observed confirming the efficient movement of Li^+ ions through the polymer electrolyte. The small, broad redox peak in the 0 to 1 V vs Li/Li^+ range might be related to redox reaction of electrode surface species,¹⁹⁵ or parasite reaction of TFSI^- anion, or other impurities.¹⁵³ From the

positive scan in the voltammetry curve, the onset of anodic current can be found at 4.6 V vs Li/Li⁺.

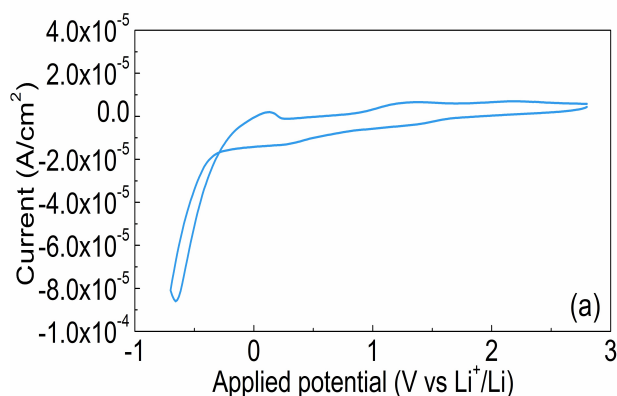


Figure 3-14 Cyclic voltammogram of CPOSS-IL-LiTFSI at 25 °C.

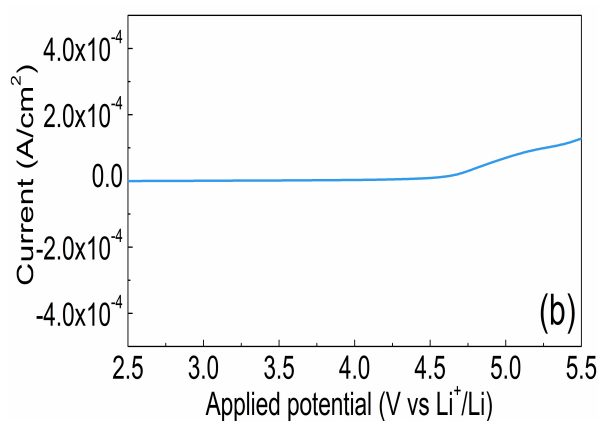


Figure 3-15 LSV curve of CPOSS-IL-LiTFSI at 25 °C.

Electrochemical impedance spectrum (EIS) was utilized to characterize the interfacial stability of CPOSS-IL-LiTFSI against lithium anode. Figure 3-16 is the nyquist plot of Li/CPOSS-IL-LiTFSI/Li cell showing the evolution of semicircle as a function of aging time at room temperature. The bulk resistance (R_b , reflects the electrolyte resistance) is reflected by the left high frequency intercept at real axis of semicircle) and interfacial resistance (R_{int} , represents the charge transfer resistance of $\text{Li}^+ + \text{e}^- = \text{Li}$ reaction at lithium/polymer electrolyte interface and

the resistance of the passive layer) is the amplitude of the diameters of the distorted semicircles. The R_b and the semicircle shape did not show noticeable increase over the storage time. The diameter of semicircle increased continuously at the early stage indicating the formation of passivation film and then ceased to grow after 9 days. After fitting with simplified equivalent circuit model, the R_b and R_{int} values were extracted from the fitting results and plotted as a function of storage time in figure 3-17. R_1 corresponds to the bulk resistance, R_2 is the interfacial resistance. CPE and W are constant phase element and Warburg diffusion element (Li^+ diffusion on the electrode/electrolyte interface and electrolyte salt diffusion), respectively.

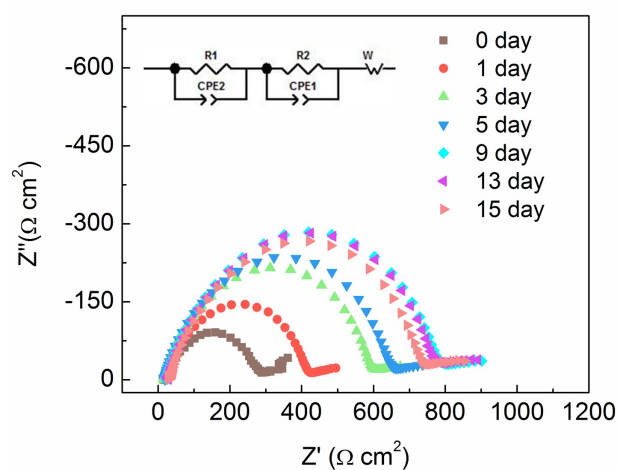


Figure 3-16 The Nyquist plots of Li symmetrical cell with CPOSS-IL-LiTFSI electrolyte at different storage time.

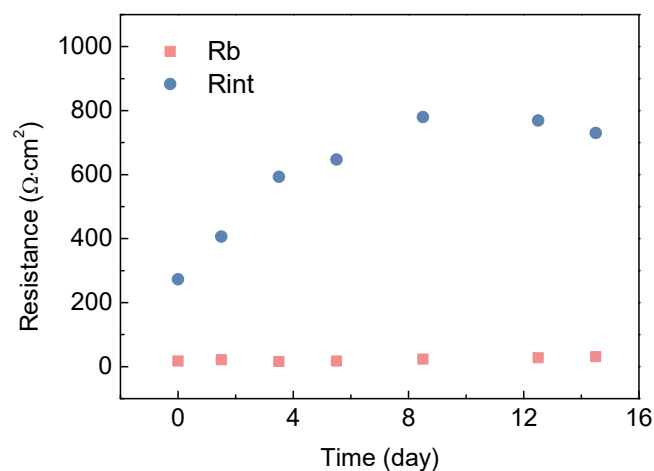


Figure 3-17 The fitted resistance value of R_b and R_{int} as a function of time.

Lithium transference number (t_{Li^+}) in CPOSS-IL-LiTFSI was investigated by chronoamperometry in combination with impedance spectroscopy reported by Bruce et al.⁸⁰ The equation can be written as $t_{Li^+} = I_s(V - I_i R_i) / I_i(V - I_s R_s)$. V is the constant DC voltage applied; I_i and I_s are the initial and steady state current, R_i and R_s are the interfacial resistance before and after DC polarization. t_{Li^+} was calculated to be 0.37 (Figure 3-18). For organic liquid electrolyte, IL-based electrolytes, and PEO-Li salt electrolyte, t_{Li^+} is normally less than 0.35.^{13, 101, 194, 196, 197} This relatively higher t_{Li^+} obtained in CPOSS-IL-LiTFSI can be attributed to reduced TFSI⁻ mobility in CPOSS-IL-LiTFSI through Coulombic interaction between imidazolium ions and TFSI⁻ and attraction between POSS and TFSI⁻ besides high mobility of Li^+ .

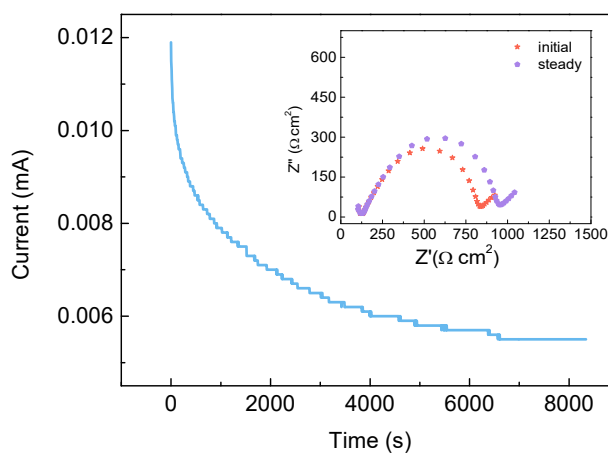


Figure 3-18 Chronoamperometry profile of Li/CPOSS-IL-LiTFSI/Li cell and inset nyquist plots at 25°C.

Lithium strip/plate test was completed on Li/CPOSS-IL-LiTFSI/Li symmetrical cells at current densities of 0.05, 0.075, and 0.10 mA/cm² to study the lithium electrodeposition stability (Figure 3-19). The Li/Li cells were charged and discharged sequentially for a period of one hour. As a control, cells with organic liquid electrolyte (1 M LiTFSI in EC/DEC/DMC, 1:1:1 by weight) were also tested. It can be observed that the 0.05 mA/cm² and 0.075 mA/cm² groups showed initial overpotential decrease (<25 cycles) which could be possibly explained by the improvement of the electrolyte/Li contact or the initial disruption of some part of passive layer.¹¹⁴ The overpotential evolution did not show fluctuations or short circuit indicating the capability of CPOSS-IL-LiTFSI to mediate lithium electrochemical deposition and dissolution. Under higher current density condition (e.g., 0.075 mA/cm² and 1 mA/cm²), higher overpotential was observed. Although the voltage hysteresis (the sum of overvoltage of stripping and plating) increased with cycle numbers for the Li/polymer/Li cells, the process is slow especially for the relative low current density (0.05 mA/cm²) group. At 50th cycle the voltage hysteresis was 47 mV. At 250th cycle, voltage hysteresis increased to 58 mV. The liquid electrolyte cells cycled at 0.075 mA/cm²

show unstable and irregular voltage spikes during the cycling process which were likely related to uneven lithium stripping/plating or dendrite formation.

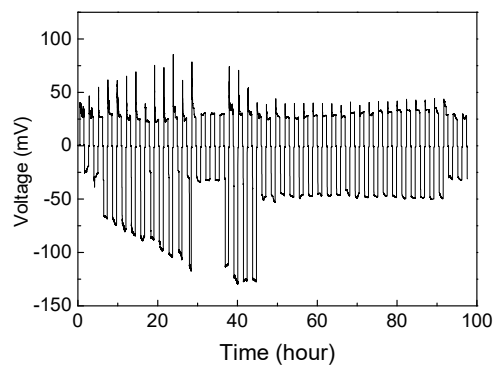
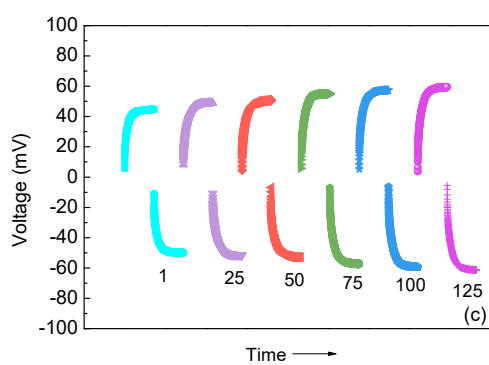
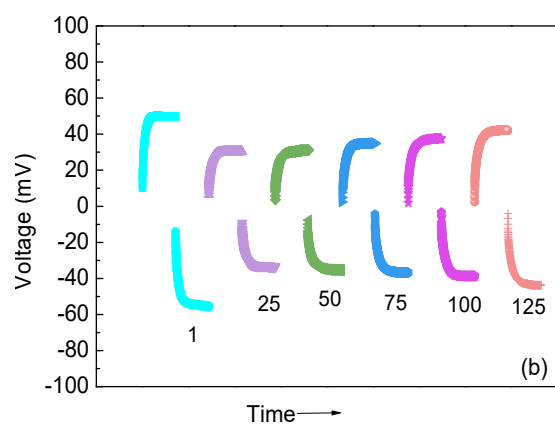
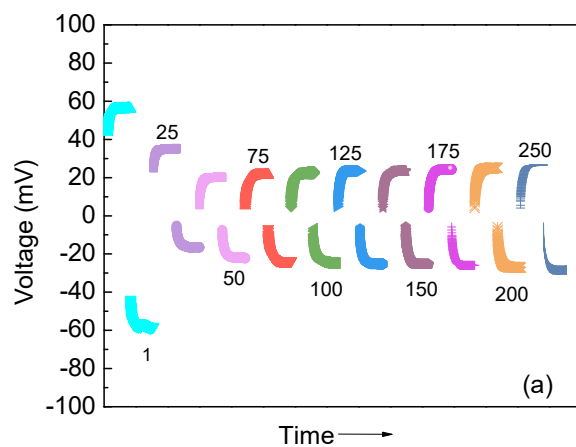


Figure 3-19 Selected galvanostatic stripping/plating cycles of Li/CPOSS-IL-LiTFSI/Li symmetrical cells with current density of a) 0.05 mA/cm^2 , b) 0.075 mA/cm^2 , and c) 0.1 mA/cm^2 . each cycle includes 1 h stripping and 1 h plating. d) Li/1 M LiTFSI EC-DEC-DMC/Li cell at 0.075 mA/cm^2 .

3.3.6 Battery Performance

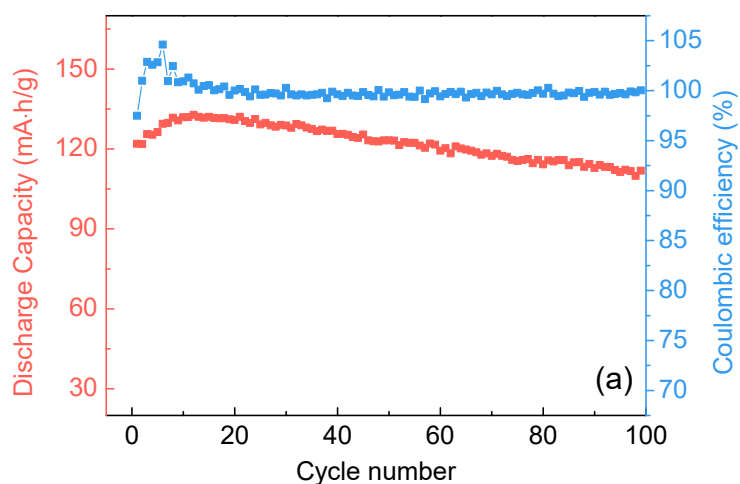


Figure 3-20 Cycling stability test of Li/CPOSS-IL-LiTFSI/LFP cell at 0.1 C. All tests were done at $25 \text{ }^\circ\text{C}$.

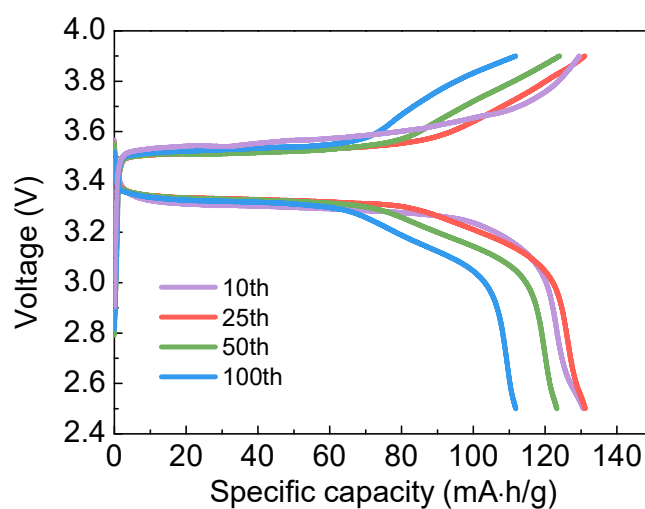


Figure 3-21 Charge-discharge curves of Li/LFP cell assembled with CPOSS-IL-LiTFSI operating at 25 °C, 0.1C.

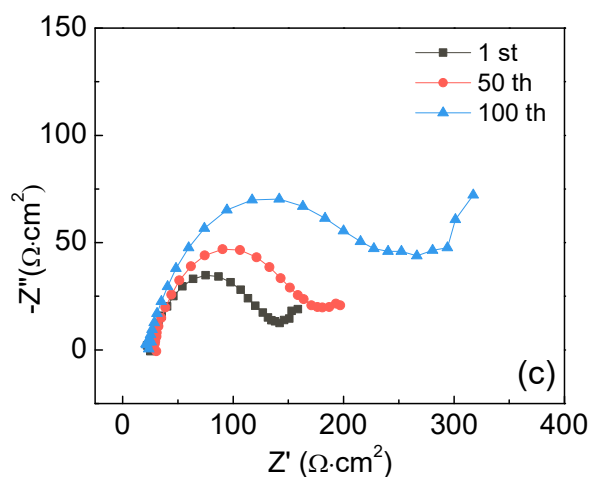


Figure 3-22 Nyquist plot of Li/CPOSS-IL-LiTFSI/LFP cell after 1, 50, and 100 cycles at 0.1 C, 25 °C, measured at half discharge state.

Galvanostatic cycling measurements of all-solid-state Li/LFP cells based on the hybrid CPOSS-IL-LiTFSI electrolyte were performed at 25 °C. At C/10, a discharge capacity up to 133 mA·h/g has been obtained. While this value is slightly lower than the discharge capacity reported in our dendritic-like electrolyte (151 mA·h/g),¹⁸⁵ this result is still among the highest values achieved so far for all-solid-state polymer lithium battery operating at room temperature.^{87, 104, 107, 110, 169} The promising performance apparently results from the notable ionic conductivity achieved at ambient temperature and outstanding electrochemical stability of CPOSS-IL-LiTFSI. Typical charge/discharge behavior is shown in Figure 3-21. The charge plateau is clearly identified at around 3.5 V vs Li^+/Li and the discharge plateau is seen at around 3.3 V vs Li^+/Li , which successfully demonstrates a reversible cycling process. The evolution of discharge capacity and coulombic efficiency with cycle number are plotted in Figure 3-20. The enhancement of the specific capacity for the first 13 cycles probably results from contact optimization of the electrode/electrolyte interface.¹⁹⁸ The specific delivered capacities at the 1st, 50th, 100th cycle are 121.9, 123.2, and 112.1 mA·h/g, respectively. Stable cycling performance is also indicative of

high ionic conductivity of the electrolyte and good compatibility between CPOSS-IL-LiTFSI and the electrodes. It is understood that the capacity fading comes from the degradation of electrode materials, the growth of solid electrolyte interphase (SEI) consuming electrolyte and lithium, the increase of interfacial resistance, and other irreversible process.^{87, 92, 199} Correspondingly, the coulombic efficiencies are 97.5%, 99.8%, and 99.8%, respectively. High coulombic efficiency is important for practical applications because it signifies good charge transfer reversibility in battery cells. The coulombic efficiency of the first cycle is lower than those of the subsequent cycles because of the formation of SEI. After the first cycle, the coulombic efficiency value rises to close to 100%, indicative of stable SEI formation between electrode and electrolyte.^{139, 200} As a demonstration, light-emitting diodes are successfully lightened up by this cell operating at ambient temperature as shown in Figure 3-23. It should be mentioned that, while intensive efforts have been focused on the development of polymer electrolytes and prototype all-solid-state polymer batteries, operation temperature is often elevated (e.g. 60 °C) in order to boost the ionic conductivity to ensure the operation of the polymer batteries.^{82, 85, 201, 202}

To further understand the all-solid-state Li/CPOSS-IL-LiTFSI/LFP battery cycling process, the evolution of nyquist plot from EIS of the battery cells is plotted in Figure 3-22. It can be seen that the bulk resistance (R_b) which is the intercept at the high frequency shows very slight changes and the interfacial resistance (R_{int}) of the Li/LFP battery gradually increases to 150 $\Omega \cdot \text{cm}^2$ at the 50th cycle and 242 $\Omega \cdot \text{cm}^2$ at the 100th cycle compared with 117 $\Omega \cdot \text{cm}^2$ of the first cycle. This is probably one of the main reasons that lead to capacity fading because the lithium loss and thickening of SEI layer could hinder the ion movement between electrolyte and electrode.^{92, 104, 203, 204} Also, the interfacial resistance likely makes the major contribution to the overpotential seen in Figure 3-21. Note that the overpotential reported herein is comparable to the literature results in which solid polymer electrolytes were utilized for lithium ion batteries at elevated temperature.²⁰⁵⁻²⁰⁷ Due to lack of liquids that could facilitate ion/charge transport across

the electrode/electrolyte interface, considerable interfacial resistances are always found in all-solid-state batteries even though the ionic conductivity of the electrolyte is high. Thus, innovative approaches are urgently needed in order to address the challenging issue of interfacial resistance in all-solid-state batteries.



Figure 3-23 Light-emitting diodes with different color could be lighted up by Li/CPOSS-IL-LiTFSI/Li cell at room temperature.

3.4 Conclusion

In summary, we have developed a new class of organic/inorganic hybrid electrolyte based on IL-grafted dumbbell-shaped POSS for the all-solid-state lithium batteries operating at ambient temperature. The resulting electrolyte exhibits excellent thermal stability and a low T_g promoting Li^+ conduction. High ionic conductivities, e.g. 1.2×10^{-4} S/cm at 20 °C, have been obtained in the hybrid electrolyte, which is among the highest values obtained in solid-state organic/polymer electrolytes measured at ambient temperature. In addition, the electrolyte exhibits great electrochemical stability (up to 4.6 vs Li^+/Li) and excellent compatibility with lithium electrode during cycling. No short circuit has been observed after more than 500 hrs in the polarization tests of Li/Li symmetrical cell. The all-solid-state Li/LFP cells using CPOSS-IL-LiTFSI as electrolyte display decent charge/discharge performance when operating at room temperature. This is remarkable since most of the current solid-state polymer cells can only operate efficiently at elevated temperatures, e.g., ≥ 60 °C. Although much work still remains to be done in order to enhance overall cell performances such as battery performance at higher rates and large current densities, we believe CPOSS-IL offers a promising structure platform to develop next-generation electrolyte for all-solid-state lithium batteries operating at ambient temperature.

Chapter 4

Network of Ionic Liquid/Octasilsesquioxane Hybrid Electrolyte Plasticized by Ionic Liquid for Lithium Ion Batteries

4.1 Introduction

Lithium ion batteries have made revolutionary change to the consumer electronics market due to their high working voltage (e.g., at the level of 4 V), long cycle life, and high energy density (e.g., 150 W h/kg).^{5,6,141} Lithium metal is regarded as the ultimate choice of anode material because of its high capacity (3860 mA h/g) and low electrode potential (-3.04 V) besides its light weight.²⁰⁸ But conventional lithium battery electrolytes (e.g., ethylene carbonate (EC), dimethyl carbonate (DMC), ethylmethyl carbonate (EMC), etc.) which is the medium between the pair of electrodes allowing ions transport bring about potential safety issue due to their volatility and strong flammability.²⁰⁹ Also, the application of lithium anode in the lithium ion batteries is severely hindered in the present of liquid electrolyte because uncontrolled and uneven deposition of lithium on the electrode surface can lead to unstable battery performance or even short-circuit.^{7,210} It is thus agreed that replacing liquid carbonate electrolytes with solid electrolytes will greatly facilitate the development of lithium battery technology towards higher energy density and larger scale application.^{138,211}

Polymers are soft, non-volatile and have much less probability to burn.^{27,175,212} Solid polymer electrolytes are excellent alternatives to replace organic liquid electrolytes because they can significantly ameliorate the battery safety problems. But there is still long way to go before ideal solid polymer electrolyte is developed because many desired parameters for solid polymer electrolytes (e.g., high ionic conductivity, excellent electrochemical stability, low interfacial

resistance between electrode and electrolyte, good mechanical integrity) are still not reached at the same time to enable practical application.^{40, 143} Poly(ethylene oxide) (PEO) has been investigated for several decades because of its oligoether linkages' ability to solvate and conduct Li⁺ ions. PEO has large fraction of crystalline phase that inhibits the Li⁺ ions motion (the amorphous phase promotes the chain dynamics above glass transition temperature T_g), ionic conductivity of PEO/lithium salt electrolyte at room temperature is normally less than 10⁻⁶ S/cm.^{27, 49, 143, 213} In addition, PEO itself is also limited by poor electrochemical stability (about 3.9 V vs Li⁺/Li).²¹⁴ Efforts such as reducing the polymer crystallization^{90, 193} and creating ion transport channel in the polymer electrolyte membrane^{99, 215} have been made aiming to improve the ionic conductivity although the improvement was quite limited. However, their ionic conductivities are still lower than 10⁻⁵ S/cm in most cases. Gel polymer electrolyte (GPE) composed of polymer hosts (e.g., poly(vinylidene fluoride) (PVDF), poly(methyl methacrylate) (PMMA), poly(acrylonitrile) (PAN), and PEO) and large amount of flammable liquid electrolyte showed enhanced ionic conductivity compared with their liquid-free counterparts at the cost of battery safety and sometimes electrochemical stability.^{42, 54, 144}

Ionic liquids (ILs) are featured by their negligible vapor pressure, high chemical and electrochemical stability in addition to their intrinsic ion conduction capability.¹⁴⁵ Covalently solidifying IL structures to polymer backbone is an effective method to integrate the ion conduction function of ILs to polymers.^{111, 129, 137, 216} Imidazolium based ILs are attractive not only because of their high ionic conductivity (close to 1×10⁻² S/cm), wide electrochemical stability window, negligible volatility, and non-flammability, but also their structural tunability and thermal stability.¹⁵² 1-ethyl-3-methyl-imidazolium bis(trifluoromethanesulfonyl)imide (EMITFSI) which has low viscosity (e.g., 30 cP), high ionic conductivity and excellent thermal stability has been tested as electrolyte component for lithium ion batteries.^{115, 217-220} Polyhedral oligomeric silsesquioxane (POSS) cubes composed of SiO_{1.5} are versatile building blocks to develop

functional hybrid materials.^{95, 102, 221-223} PEO functionalized POSS molecules have been reported before because POSS cages are non-flammable and have been used as flame retardant in polymers.^{224, 225} Moreover, POSS can induce extra free volume of polymers, resist polymer crystallization, and provide mechanical strength in the polymer electrolyte system.^{94, 95, 99} Therefore, POSS is suitable to be incorporated into polymer electrolytes to develop organic-inorganic hybrid electrolytes.^{95, 226}

In this work, organic-inorganic electrolyte (XPOSS-IL) was constructed as network of imidazolium-based ionic liquid functionalized, oligomeric PEO grafted POSS cages. To the best of our knowledge, this is the first example of immobilizing ionic liquid structure within the network of oligomeric silsesquioxanes as hybrid electrolyte. Small fraction of Ionic liquid EMITFSI was incorporated as plasticizer and high ionic conductivity of the electrolyte (e.g., $>1 \times 10^{-4}$ S/cm) is obtained at ambient temperature. Successful cycling performances of Li/LTO and Li/LFP battery cells with XPOSS-IL-LiTFSI/EMITFSI electrolytes at low and elevated temperatures were also confirmed.

4.2 Experimental

4.2.1 Materials

Azoisobutyronitrile (AIBN, Aldrich, 98%). Octasilane polyhedral oligomeric silsesquioxane (POSS) was purchased from Hybrid Plastics and dried at 60 °C under vacuum overnight before use. 1-ethyl-3-methyl-imidazolium bis(trifluoromethanesulfonyl)imide (EMITFSI, 99.9%, Solvionic). Anhydrous tetrahydrofuran (THF), anhydrous dichloromethane (DCM), anhydrous N-Methyl-2-pyrrolidone (NMP) were ordered from Aldrich. Karstedt catalyst solution in xylene

(2%, Aldrich). 1-vinyl imidazole (99%, Aldrich), lithium bis(trifluoromethanesulfonyl) imide (LiTFSI, Aldrich). Dichloromethane, chloroform, and methanol were purchased from VWR.

4.2.2 Synthesis of 17-bromo-3,6,9,12,15-pentaoxaheptadecan-1-ol

In a 50 mL flask equipped with a magnetic stirrer, hexaethylene glycol (hEG, 10 g, 35.42 mmol) and triphenyl phosphine (4.65 g, 17.71 mmol) were dissolved in 25 mL anhydrous THF at 30 °C. The system was purged with nitrogen for 35 min before CBr₄ (5.87 g, 17.71 mmol) was added. The reaction was allowed to proceed for four hours at 30 °C under nitrogen atmosphere. The solution was then concentrated on a rotary evaporator at 50 °C and the crude product was purified by column chromatography with chloroform/methanol (95:5 v/v) to give 17-bromo-3,6,9,12,15-pentaoxaheptadecan-1-ol as slight yellow oil. ¹H NMR (300 MHz, CDCl₃, ppm) δ: 3.16 (s, -OH), 3.45 (t, -CH₂-Br), 3.58-3.68 (m, -O-CH₂-), 3.78 (t, -CH₂-CH₂-Br); ¹³C NMR (CDCl₃, ppm) δ: 30.1, 61.6, 70.2-70.7 (br), 73.0 (-CH₂-CH₂-Br).

4.2.3 Synthesis of vinyl tris (17-bromo-3,6,9,12,15-pentaoxaheptadecan-1-ol) silane (Vtris(PEO-Br))

17-bromo-3,6,9,12,15-pentaoxaheptadecan-1-ol (2.8 g, 0.008 mol) and triethylamine (1.6 g, 0.016 mol) were dissolved in 40 mL toluene in a 100 mL flask. Trichlorovinylsilane (0.437 g, 2.67 mmol) was charged to the solution under N₂ atmosphere. The reaction took place for 3 h and EtOAc was added to dilute the solution. After washing with water and dried with Na₂SO₄. The organic phase was concentrated to give the product. : ¹H NMR (CDCl₃) δ: 3.43 (t, -CH₂-Br), 3.58-3.68 (m, -O-CH₂-), 3.79 (-O-CH₂-CH₂-Br), 3.89 (t, -Si-O-CH₂-), 5.9-6.1 (m, CH₂=CH-Si-),

^{13}C NMR (CDCl_3) δ : 30.1, 62.4 (-Si-O- $\underline{\text{C}}\text{H}_2$), 70.8-71.9 (signal overlap), 72.7 (- $\underline{\text{C}}\text{H}_2$ - $\underline{\text{C}}\text{H}_2$ -Br), 137.4 ($\underline{\text{C}}\text{H}_2=\underline{\text{C}}\text{H}$ -Si).

4.2.4 Synthesis of 1-vinyl imidazole grafted POSS (POSS-Vim)

VtrisPEO-Br (2.74 g, 2.52 mmol) and POSS (320 mg, 0.32 mmol) were dissolved in 30 mL toluene in a 100 mL flask equipped with a magnetic stir bar. The solution was purged with N_2 for 40 min before Karstedt catalyst was added. The reaction lasted for 48 h at 55 °C before the solvent was evaporated. The product was dried in vacuo to give light yellow viscous material (POSS-hEG-Br). POSS-hEG-Br (2.73 g, 0.28 mmol) and 1-vinyl imidazole (632 mg, 6.72 mmol) was dissolved in 30 mL THF. The reaction mixture was stirred under N_2 at 60 °C for 24 h. LiTFSI was added to the solution subsequently. After evaporation of solvent, the product was redissolved in DCM and the solution was filtrated and concentrated to give light yellow viscous oil. ^1H NMR (CDCl_3 , ppm) δ : 7.67(-N- $\underline{\text{C}}\text{H}$ -N-), 7.18 6.93-6.85 (- $\underline{\text{C}}\text{H}=\underline{\text{C}}\text{H}_2$), 5.30-4.87 (- $\underline{\text{C}}\text{H}=\underline{\text{C}}\text{H}_2$), 3.43-3.80 (-O- $\underline{\text{C}}\text{H}_2$ -), 0.15-0.04 (Si- $\underline{\text{C}}\text{H}_3$).

4.2.5 Synthesis of X-POSS-IL and preparation electrolyte precursor solution

In the argon-charged glove box, POSS-Vim (0.4 g) and initiator (AIBN, 7 mg) were dissolved in 5 mL THF. 0.5 mL of the solution was taken out and heated at 60 °C for 10 h to give solvent-free crosslinked sample X-POSS-IL for FTIR characterization. FTIR (cm^{-1}): 1575, 1457 (ν , imidazole ring), characteristic bands for TFSI: 1352, 1195, 1135, 1056, 653. 1100 (ν , C-O-C, Si-O-Si). To prepare the sample for the ionic conductivity measurement and electrochemical testing, LiTFSI (18 wt.%) and EMITFSI with different weight compositions was completely dissolved in the mixed solution of POSS-Vim and initiator prior to the reaction (The composition

is shown in Table 4-1). Then the solution was casted on substrates followed by crosslinking reaction. The final crosslinked electrolyte was named as X-POSS-IL-LiTFSI/x.(x is equal to 100×weight percentage of EMITFSI).

Table 4-1 Summary of X-POSS-IL/ionic liquid composition and ionic conductivity at 30 °C.

Sample name	x-POSS-IL weight (g)	LiTFSI weight (g)	EMITFSI weight (g)	EMITFSI/x-POSS-IL ratio wt./wt.	Ionic conductivity at 30 °C (S/cm)
x-POSS-IL	0.4	0	0	0	1.7×10^{-5}
x-POSS-IL-LiTFSI/0	0.4	0.08	0	0	5.4×10^{-5}
x-POSS-IL-LiTFSI/4	0.4	0.08	0.02	0.04	9.7×10^{-5}
x-POSS-IL-LiTFSI/11	0.4	0.08	0.06	0.11	1.4×10^{-4}
x-POSS-IL-LiTFSI/20	0.4	0.08	0.12	0.2	2.0×10^{-4}

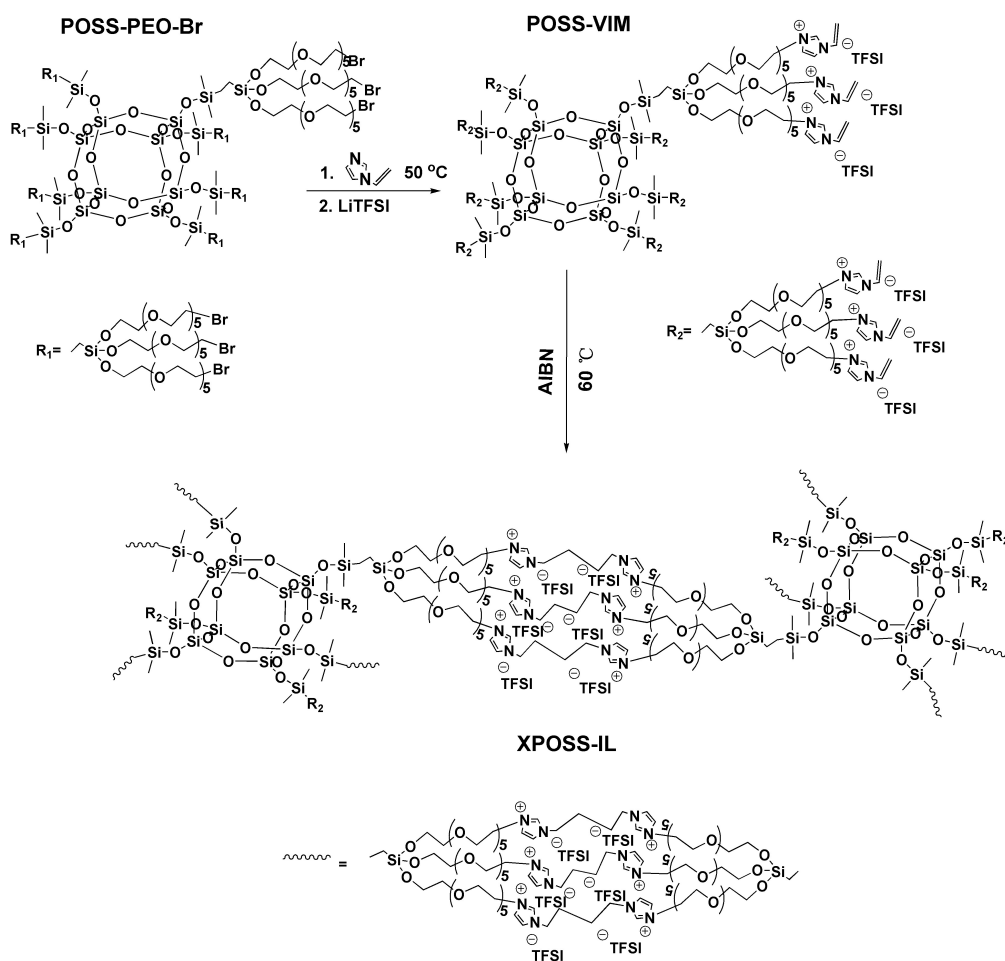
4.2.6 Characterization

^1H NMR was measured on a Bruker AV-500 Nuclear Magnetic Resonance Spectrometer using CDCl_3 as the solvent. FTIR measurements were performed on Bruker Vertex 70 spectrometer. TA Q100 differential scanning calorimeter (DSC) was used to measure the glass transition temperature with heating and cooling rate of 10 °C/min in the range of -85 to 40 °C. The thermal stability was studied by thermogravimetric analysis (TGA) measurements on TA Instrument model Q50 at a heating rate of 10 °C/min under N_2 from 25 °C to 650 °C.

Wide-angle X-ray diffraction (WAXD): WAXD was performed on a Rigaku DMAX-Rapid Microdiffractometer equipped with a 2-D detector using CuK_α radiation. The software routines were used to evaluate the scattering intensity as a function of the diffraction angle of 2θ ranging from 4 to 30 °C.

The ionic conductivities of the electrolytes were measured by Electrochemical Impedance Spectroscopy (EIS). The electrolyte samples were sandwiched between two stainless steel (SS) blocking electrodes with O-shaped Teflon ring as spacer (125 μm thick). The σ was calculated according to $\sigma=L/R_bS$, L is the film thickness, R_b is the bulk resistance and S is the electrode contacting area (0.785 cm^2). The impedance data was recorded on Solatron 1260 impedance/gain phase analyzer with AC voltage amplitude of 30 mV over the frequency range from 1 MHz to 100 mHz. Li^+ ion transference number (t_{Li^+}) was calculated based on the method report by Bruce and Vincent.⁸⁰ $t_{\text{Li}^+}=I_{\text{ss}}(\Delta V-I_0R_0)/I_0(\Delta V-I_{\text{ss}}R_{\text{ss}})$. R_0 and R_{ss} are initial and steady state resistance. I_0 and I_{ss} are initial and steady state current. ΔV is the DC pulse voltage to polarize the cell. ΔV of 30 mV was used to polarize the cell. For voltammetry test, Li/polymer/stainless steel CR2032 coin cell samples were measured on PAR Potentiostat/Galvanostat Model 263A, scan rate: 1 mV/s.

For the battery cells performances study, CR2032 type coin cells were assembled in the argon-filled glovebox. The cathode slurries containing 80 wt.% of LFP, 10 wt.% of super P, and 10 wt.% of PVDF in NMP was spread onto the aluminum foil and dried at 80 $^{\circ}\text{C}$ under vacuum to get uniform thickness with the areal density of 1.5-1.8 mg/cm^2 . The prepared cathode was cut into circular disks with 1 cm diameter (0.785 cm^2) and weighted. The prepared electrolyte precursor solution with LiTFSI and initiator with was drop casted onto the anode followed by gently heating around 60 $^{\circ}\text{C}$ to start the crosslinking process. The two electrodes were separated by a ring-shaped spacer with thickness of 125 μm . The battery charge/discharge tests were carried out on Neware CT-3008 battery tester at room temperature between 2.5 V and 3.9 V vs Li^+/Li .



Scheme 4-1 Synthetic route of XPOSS-IL.

4.3 Result and discussion

4.3.1 Synthesis

The preparation of X-POSS-IL was completed by two general steps. First, POSS-Vim was synthesized by coupling POSS-PEO-Br (shown in scheme 4-1) with 1-vinyl imidazole and ion exchange process. The synthesis of POSS-PEO-Br was achieved by grafting vinyl tris (17-bromo-3,6,9,12,15-pentaoxaheptadecan-1-ol) silane to the POSS through hydrosilylation. Then

POSS-Vim was crosslinked by free radical reaction process of the vinyl groups (Scheme 4-1 and Figure 4-7). The ^1H NMR spectrum of POSS-Vim is shown in Figure 4-1 from which the proton signals of the grafted C=C double bond can be observed. From the FTIR characterization results in Figure 4-2, the C-N and C-C stretching vibration of the imidazolium ring are found at 1457 cm^{-1} and 1575 cm^{-1} . TFSI characteristic bands are observed at 1352, 1195, 1135, 1056, and 653 cm^{-1} . The C-O-C and Si-O-Si stretching vibration bands overlapped at 1100 cm^{-1} .

Figure 4-1 ^1H NMR of POSS-VIM.

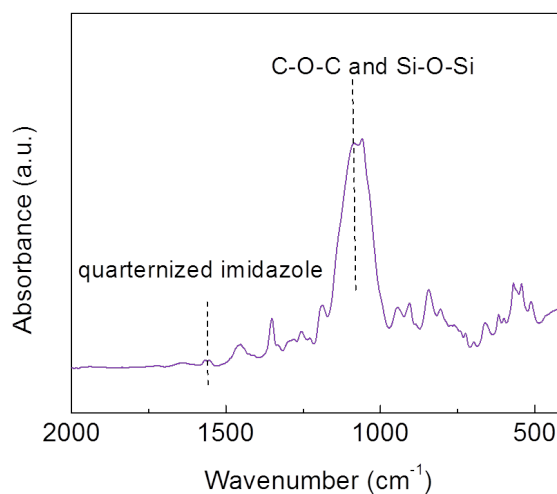


Figure 4-2 FTIR spectrum of X-POSS-IL.

4.3.2 Thermal properties

Figure 4-3 shows the typical DSC characterization result of X-POSS-IL-LiTFSI. Its glass transition temperature (T_g) was found to be $-60.3\text{ }^{\circ}\text{C}$. The thermal decomposition measurement result of X-POSS-IL-LiTFSI is shown in Figure 4-4. The thermal composition temperature was treated as 5 % of weight loss. Roughly, two-stage decomposition behavior was observed for X-POSS-IL-LiTFSI. The first stage starting at $200\text{ }^{\circ}\text{C}$ was attributed to the thermal decomposition of the polymer matrix. The second stage around $400\text{ }^{\circ}\text{C}$ was the LiTFSI decomposition.^{66, 227} EMITFSI has excellent thermal stability and has been reported to be thermally stable up to $450\text{ }^{\circ}\text{C}$.^{124, 228} So the incorporation of EMITFSI was not supposed to weaken the electrolyte thermal stability.

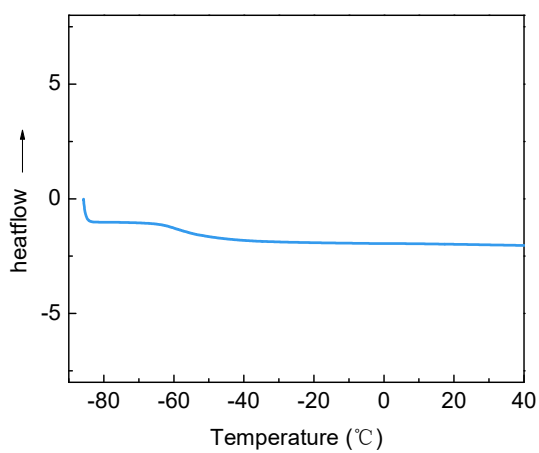


Figure 4-3 DSC curve of XPOSS-IL-LiTFSI.

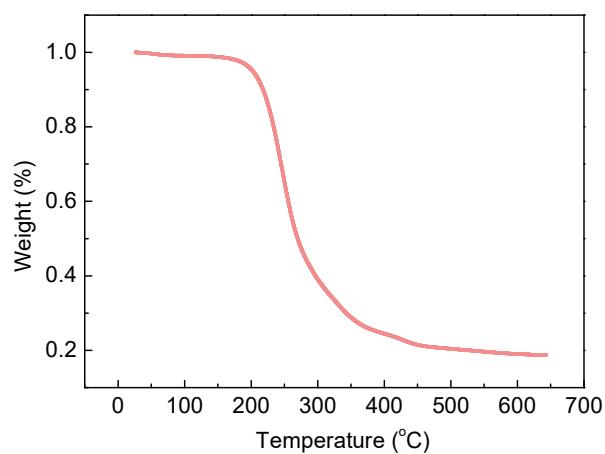


Figure 4-4 TGA curve of XPOSS-IL-LiTFSI.

4.3.3 Microstructural characterization

The amorphousness of X-POSS-IL was also confirmed by the XRD analysis (Figure 4-5). The scattering amorphous halo located at $2\theta = 8.2^\circ$ (d spacing of 10.7 Å) was assigned to the 101

reflection of POSS rhombohedral unit cell. Another scattering halo at $2\theta = 21.3^\circ$ (d spacing of 4.2 Å) is a sign of the amorphous state of PEG in X-POSS-IL.

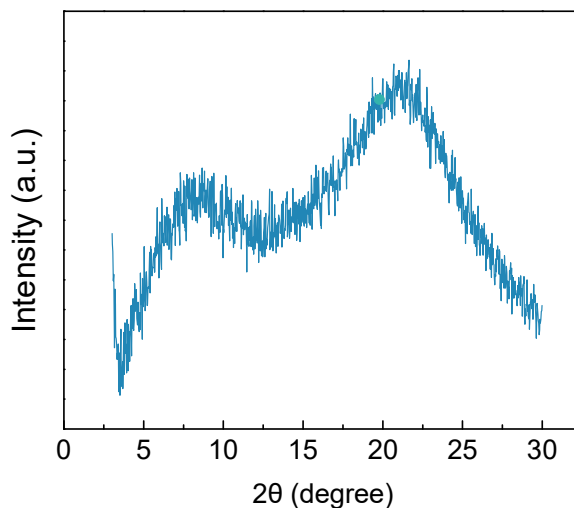


Figure 4-5 X-ray diffraction pattern of XPOSS-IL-LiTFSI.

4.3.4 Ionic conductivity

The ionic conductivity dependence of X-POSS-IL-LiTFSI with temperature was investigated by impedance spectroscopy in the temperature range between -10°C to 60°C and the calculated σ data was plot against temperature in Figure 4-6. At 30°C , the ionic conductivity value of X-POSS-IL-LiTFSI was $5.4 \times 10^{-5} \text{ S/cm}$. The conductivity value was lower than that of our previously reported non-crosslinked electrolyte with similar molecular structure probability because crosslinking process can restrict the polymer chain segmental motion.¹⁸⁵ Interestingly, the conductivity is comparable with other non-crosslinked PEO functionalized POSS electrolytes which had no tethered ionic liquid moieties.¹⁰² The addition of room temperature ionic liquids into polymer electrolyte system has proved to promote Li^+ conduction both theoretically and experimentally.^{16, 115, 124, 138, 218, 229} It is reported that the ionic conductivity of EMITFSI is as high as $1.06 \times 10^{-2} \text{ S}\cdot\text{cm}^{-1}$ at 303K.²³⁰ By adding 4 wt%, 11 wt%, and 20 wt% of EMITFSI in XPOSS-

IL-LiTFSI, the corresponding ionic conductivity at 30 °C increased to 9.74×10^{-5} S/cm, 1.4×10^{-4} S/cm, and 2.0×10^{-4} S/cm, respectively. This is noticeable because only a small fraction of ionic liquid could significantly bring up the ionic conductivity to the 10^{-4} S/cm range.^{197, 231} The conductivity data can be fitted as the dashed lines by Vogel-Tamman-Fulcher (VTF) equation. $\sigma = AT^{-1/2} \exp[-E_a/R(T-T_0)]$. E_a is a constant related to activation energy for ion conduction. A is a pre-exponential factor. T_0 is the reference temperature. R is the ideal gas constant.

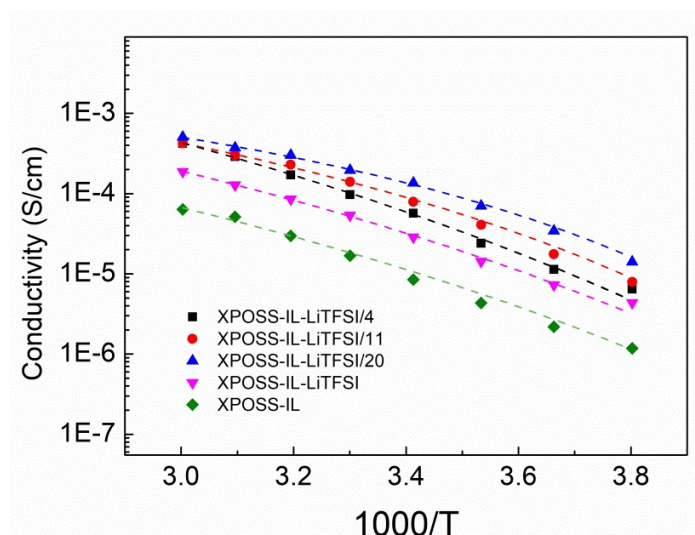


Figure 4-6 Comparison of ionic conductivity of XPOSS-IL, XPOSS-IL-LiTFSI, and XPOSS-IL-LiTFSI with different amount of added EMITFSI.

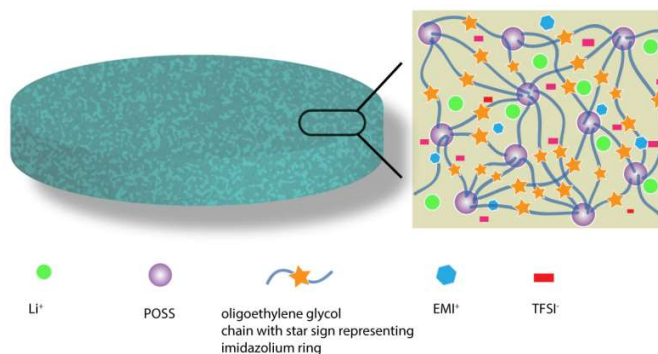


Figure 4-7 Photo image and schematic illustration of XPOSS-IL-LiTFSI/EMITFSI.

4.3.5 Electrochemical properties

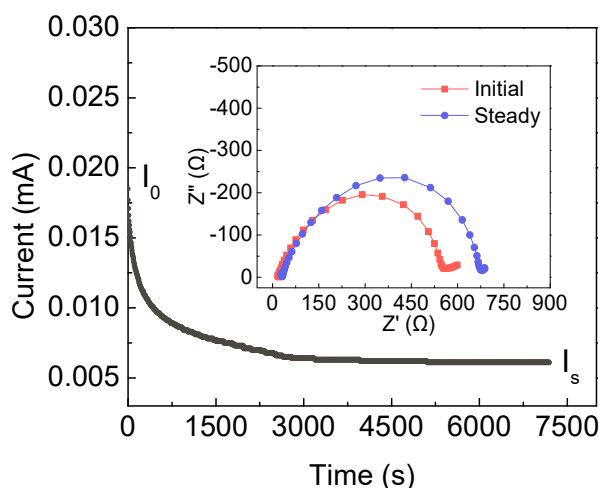


Figure 4-8 Chronoamperometry profile of Li/X-POSS-IL-LiTFSI/11/Li cell and inset nyquist plots before and after the polarization at 25°C.

The Li^+ ions transference number (t_{Li^+}) of X-POSS-IL-LiTFSI/11 was calculated according to the method reported in the literature.⁸⁰ The equation is written as $t_{\text{Li}^+} = I_s(V - I_i R_i) / I_i(V - I_s R_s)$. V is the constant DC polarization potential difference applied; I_i and I_s are the initial and steady-state current, R_i and R_s are the initial and steady-state interfacial resistance. Figure 4-8 shows the chronoamperometry profile of Li/X-POSS-IL-LiTFSI/11/Li cell with inset AC impedance spectra. The transference number for X-POSS-IL-LiTFSI/11 was calculated to be 0.25. The electrochemical stability of X-POSS-IL-LiTFSI/EMITFSI investigated by LSV method is shown in Figure 4-9 and Figure 4-10. Three samples with different EMITFSI concentrations were measured. In the oxidation side (above 3.0 V vs Li^+/Li), the onset of anodic currents are found at 4.1 V vs Li^+/Li , 4.2 V vs Li^+/Li , and 4.6 V vs Li^+/Li for X-POSS-IL-LiTFSI/0, X-POSS-IL-LiTFSI/11, and X-POSS-IL-LiTFSI/20, respectively. From the cathodic scan, two major peaks

can be identified for the samples, peaks are at 1.0 V and 0.48 V for the 15 wt% group. This was possibly due to the irreversible reduction of C-2 carbon of the EMI^+ cations.¹²⁴ As the EMITFSI concentration increases to 20 wt%, the reduction current increases as well. The LSV cathodic scan of pure X-POSS-IL showed a broad and weaker reduction peak. Zhu et al. found that introducing a small amount of EMITFSI to PEO-LiTFSI electrolyte system will not only enhance the ionic conductivity but also electrochemical stability window.¹¹⁵ Another group prepared poly[diallyldimethylammonium] bis(trifluoromethane) sulfonamide based polymer electrolyte plasticized by EMITFSI and enhanced electrochemical stability was also observed compared with pure ionic liquid.²¹⁹

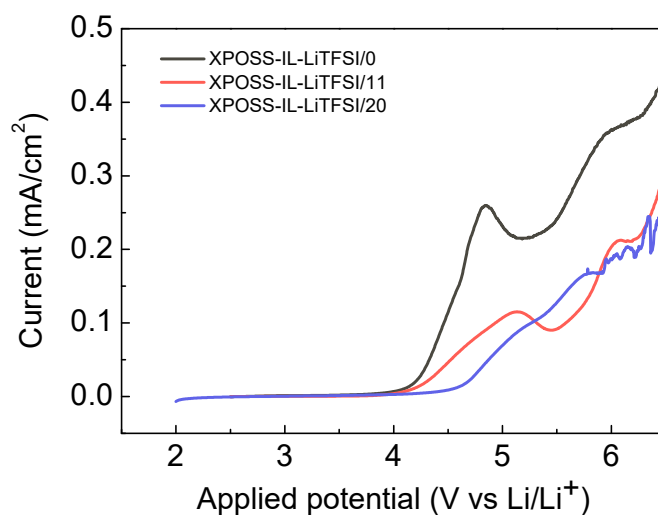


Figure 4-9 Anodic scan of XPOSS-IL-LiTFSI with different percentages of added ionic liquid.

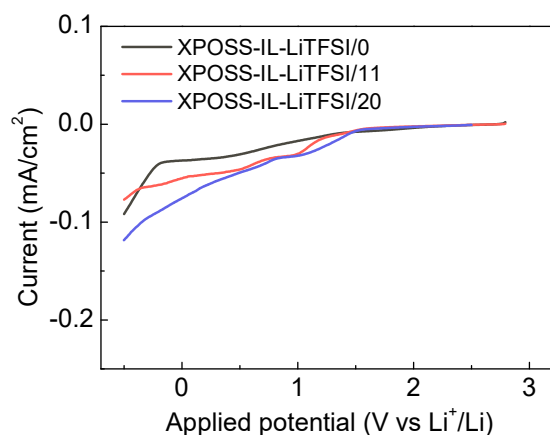


Figure 4-10 Cathodic scan of XPOSS-IL-LiTFSI with different percentage of added ionic liquid.

4.3.6 Battery Performance

Li/LTO and Li/LFP coin cells were assembled with XPOSS-IL-LiTFSI/11 electrolyte to evaluate its electrochemical performance in lithium metal batteries. From the rate performance plot of Li/XPOSS-IL-LiTFSI/11/LTO cell at 60 °C, it can be seen that XPOSS-IL-LiTFSI/11 could support Li/LTO cell to cycle at different C-rates (Figure 4-11). The specific capacities delivered were 142 mA·h/g at 0.1 C, 132 mA·h/g at 0.2 C, 108 mA·h/g at 0.5 C, 51 mA·h/g at 1 C, respectively. Li/ XPOSS-IL-LiTFSI/11/LFP coin cells were investigated as well. The cells were cycled under constant current condition at 25 °C from 2.5 V to 3.9 V (C/10). C/x indicates charge or discharge of the theoretical capacity value of cathode takes x hours. As shown in Figure 4-12, potential plateaus at 3.55 V and 3.35 V stand for the two phase lithium insertion/extraction ($\text{LiFePO}_4/\text{FePO}_4$) during charge and discharge process. The cell could deliver maximum specific capacity of 158.6 mA·h/g at the second cycle. Figure 4-13 displays the cycle number dependence of the delivered specific capacity. The maximum capacity could be maintained for the initial 12 cycles and then the cycling performance started to fade. This is probably due to the gradual

thickening of electrode/electrolyte interfacial layer contributed by reduction product of electrolyte or consumption of electrode materials.^{197,231} The coulombic efficiency at 1st, 15th, and 30th cycle were 88.1 %, 99.1 %, and 99.6 %, respectively. EIS method was used to characterize the interfacial compatibility of X-POSS-IL-LiTFSI/EMITFSI based coin cells. The nyquist plots obtained based on the EIS data of Li/LFP cells in the charged state of 15th and 30th cycle is shown in Figure 4-14. The high frequency intercept represents the electrolyte resistance R_e . The diameter of distorted semicircle is interfacial resistance (R_i) contributed by charge-transfer resistance and also the ion transport resistance in the SEI film. The interfacial resistance increased from 296 $\Omega \cdot \text{cm}^2$ to 410 $\Omega \cdot \text{cm}^2$ due to side reactions in the cells and this also explained the reason for the delivered capacity decay.⁹² The bulk resistance did not show obvious change indicating good electrochemical stability of the electrolyte.

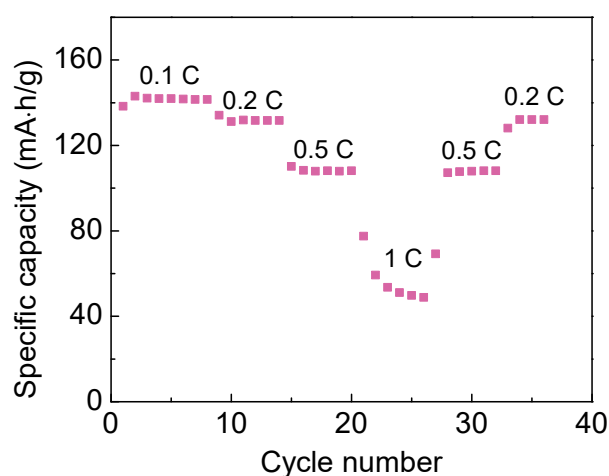


Figure 4-11 Rate performance of Li/XPOSS-IL-LiTFSI/11/LTO cell running at 60°C, 0.1C.

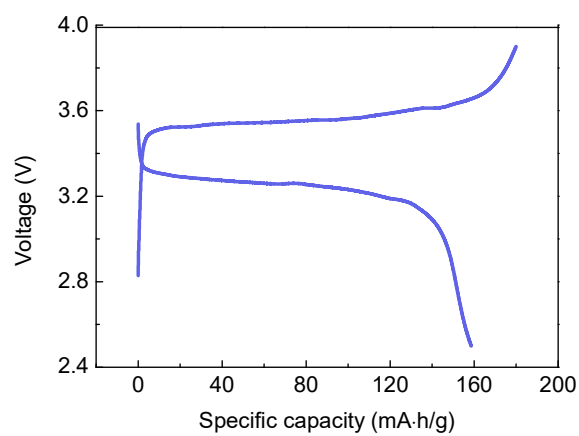


Figure 4-12 Charge/discharge curve of Li/LFP cell assembled with XPOSS-IL/11 operating at 25 °C, 0.1C.

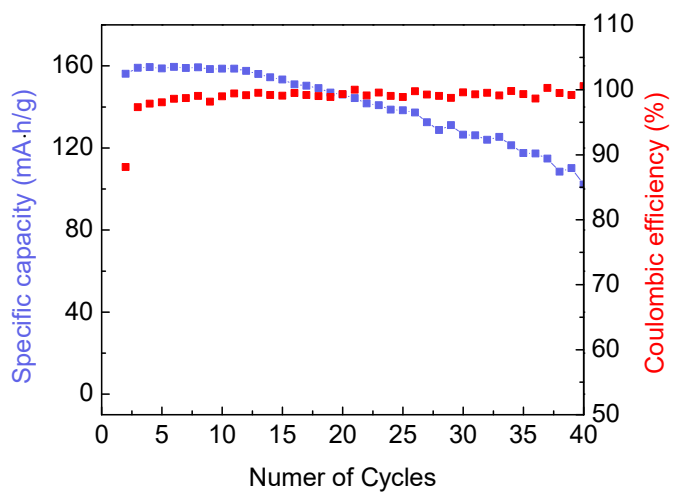


Figure 4-13 Cycling stability of Li/LFP cell assembled with XPOSS-IL/11 operating at 25 °C, 0.1C.

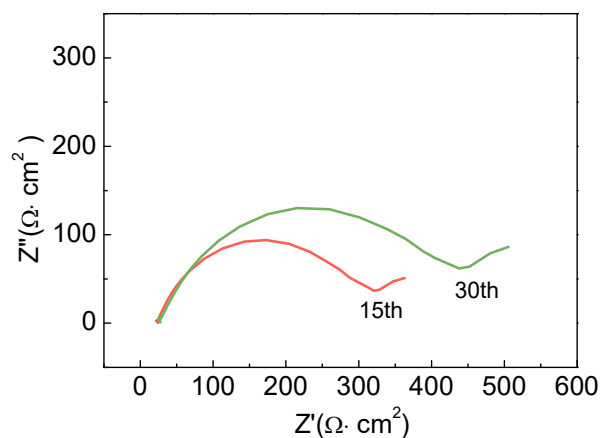


Figure 4-14 Nyquist plot of Li/XPOSS-IL/15/LFP cell after 15 and 30 cycles at 0.1 C, 25 °C, measured at half discharge state.

4.4 Conclusion

In summary, organic-inorganic hybrid electrolytes XPOSS-IL-LiTFSI based on crosslinked imidazolium functionalized POSS cages were synthesized. The presence of imidazolium cations and counter ions within the network structure of the hybrid electrolytes, the amorphous characteristic, and the low glass transition temperature in XPOSS-IL-LiTFSI provide favorable environment for ion conduction. Also, the ionic conductivity of X-POSS-IL-LiTFSI shows significant increase from 5.4×10^{-5} S/cm to 1.4×10^{-4} S/cm at 30 °C by doping with small fraction of EMITFSI. The ionic liquid incorporated X-POSS-IL-LiTFSI exhibited enhanced anodic stability compared with the pure X-POSS-IL-LiTFSI. The prototype lithium battery cells assembled with X-POSS-IL-LiTFSI/EMITFSI demonstrate capability of delivering high specific capacity at both ambient temperature and elevated temperature. We believe this research provides hints on designing new ion containing organic-inorganic hybrid electrolytes towards application on solid-state lithium ion batteries.

Chapter 5

Summary and Suggestions for Future Work

5.1 Summary

The purpose of the research work in this thesis is to develop organic/inorganic hybrid electrolyte with high ionic conductivity and good electrochemical properties for the application in the next generation lithium ion batteries. A series of ionic liquid immobilized organic/inorganic hybrid polymer electrolytes have been successfully synthesized and characterized. They can be classified as: 1) POSS-IL, which has a branched structure with POSS cage core and IL functionalized oligoethylene glycol arms; 2) CPOSS-IL, which has linked POSS-cages and peripheral IL functionalized oligoethylene glycol arms; 3) XPOSS-IL, which was achieved by crosslinking the IL functionalized POSS cage with vinyl group chain end.

First of all, a unique class of organic-inorganic hybrid electrolyte (POSS-IL) based on IL-grafted POSS has been synthesized and studied. The electrolyte exhibits many impressive properties, including non-flammability, high room temperature ion conductivity (4.8×10^{-4} S/cm) and excellent electrochemical stability for Li-metal batteries. Prototype batteries using POSS-IL as electrolyte have been successfully cycled at room temperature with LTO and LFP cathode. The excellent cycling stability of POSS-IL against lithium has been supported by the plating-stripping experiments on a symmetrical cell with Li-metal electrodes. While considerable work remains to be done, that this work is believed to provide a promising structure platform for the development of new solid-state electrolytes for ambient-temperature lithium ion battery.

Dumbbell shaped hybrid electrolyte (CPOSS-IL) derived from POSS-IL was successfully synthesized as an extension of POSS-IL. CPOSS-IL is amorphous and proves good thermal

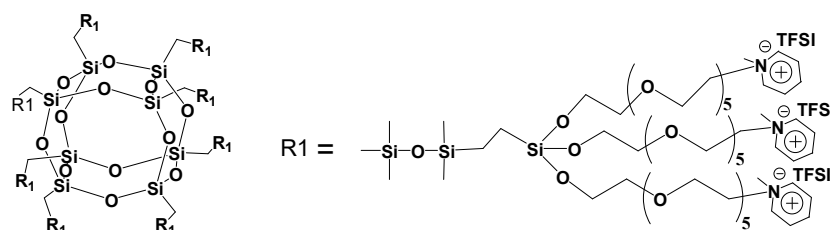
stability and low glass transition temperature favoring fast ion transport. The ionic conductivity of CPOSS-IL-LiTFSI at room temperature is also higher than 10^{-4} S/cm (1.2×10^{-4} S/cm). This also indicates that the grafted ionic liquid molecules do favor the ionic conductivity increase. CPOSS-IL also has good electrochemical stability. Li/CPOSS-IL-LiTFSI/LFP cell can successfully run charge/discharge cycle at 25 °C. This is also confirmed from the stable lithium strip/plate cycling performance. Research work remains to be finished to gain better understanding of the interfacial properties of the batteries. In summary, CPOSS-IL provides a new and promising structure for hybrid electrolytes of room temperature solid state lithium ion battery.

Moreover, by incorporation of reactive C=C double bonds at the chain end of imidazole-based ionic liquid functionalized POSS, XPOSS-IL which has ionic network structure was obtained through free radical reaction of the double bonds. Doping small fraction of EMITFSI in XPOSS-IL increases the ionic conductivity significantly without compromising the electrochemical stability and can be applied as non-flammable electrolytes for room temperature lithium ion battery.

5.2 Suggestion for future work

The content of this thesis work mainly focused on the synthesis and characterization of a series of imidazolium-based ionic liquid grafted hybrid polymer electrolytes. Much work still remains to be done towards further optimization of their chemical structure in order to enhance their properties (e.g., ionic conductivity, electrochemical stability, mechanical property, compatibility, fabrication simplicity, etc.) for practical battery application. At the same time, more attention should be placed on utilizing different characterization methods to gain a comprehensive understanding of the properties of the electrolytes, and also to have a closer look into the electrode/electrolyte interface. Some suggestions are listed below:

- a. Experiments are necessary to answer how the variation of the fraction of grafted the ionic liquid and PEO spacer length will influence the ionic conductivity and electrochemical properties.
- b. Other ionic liquid species besides imidazolium can also be incorporated into the hybrid electrolytes. For example, it has been reported that piperidinium based ionic liquid with TFSI⁻ counter ion demonstrated wider electrochemical stability compared with imidazolium based ionic liquid.²³² It is worthy to try grafting piperidinium ionic liquids to POSS (shown below). Meanwhile, the counter ion could also be varied as well.



- c. Ionic conductive ceramic fillers such as garnet $\text{Li}_7\text{La}_3\text{Zr}_2\text{O}_{12}$ (LLZO)-derived electrolytes and NASICON-type lithium ion conductors $\text{Li}_{1+x}\text{Al}_x\text{Ti}_{2-x}(\text{PO}_4)_3$ (LATP) could be added to the above synthesized polymer electrolytes to tune the ionic conductivity, mechanical strength and electrochemical properties.
- d. During or after the cell operation, the components in the passivation layer on the surface of the electrodes need to be studied using surface characterization techniques such as XPS and SEM.
- e. More studies need to be placed on improving the mechanical integrity of the hybrid electrolytes through molecular design and synthesis and keeping high ionic conductivity and good electrochemical stability.

References

1. Reddy, T., *Handbook of batteries*. McGraw-Hill Pub.: 2002.
2. Abouimrane, A.; Ding, J.; Davidson, I. *J. Power Sources* **2009**, 189, (1), 693-696.
3. Li, Q.; Chen, J.; Fan, L.; Kong, X.; Lu, Y. *Green Energy & Environment* **2016**.
4. Tarascon, J.-M.; Armand, M. *Nature* **2001**, 414, (6861), 359-367.
5. Goodenough, J. B.; Park, K.-S. *J. Am. Chem. Soc.* **2013**, 135, (4), 1167-1176.
6. Scrosati, B.; Garche, J. *J. Power Sources* **2010**, 195, (9), 2419-2430.
7. Khurana, R.; Schaefer, J. L.; Archer, L. A.; Coates, G. W. *J. Am. Chem. Soc.* **2014**, 136, (20), 7395-7402.
8. David, L.; Thomas, B. R., *Handbook of batteries*. McGraw-Hill Professional: 2001.
9. Wu, Y., *Lithium-Ion Batteries: Fundamentals and Applications*. CRC Press: 2015; Vol. 4.
10. Zhao, B.; Ran, R.; Liu, M.; Shao, Z. *Materials Science and Engineering: R: Reports* **2015**, 98, 1-71.
11. Xu, K.; Wang, C. *Nature Energy* **2016**, 1, 16161.
12. Wakihara, M.; Yamamoto, O., *Lithium ion batteries: fundamentals and performance*. John Wiley & Sons: 2008.
13. Xu, K. *Chem. Rev.* **2004**, 104, (10), 4303-4418.
14. Nazri, G.-A.; Pistoia, G., *Lithium batteries: science and technology*. Springer Science & Business Media: 2008.
15. Zhou, D.; Liu, R.; He, Y. B.; Li, F.; Liu, M.; Li, B.; Yang, Q. H.; Cai, Q.; Kang, F. *Adv. Energy Mater.* **2016**.
16. Zhang, P.; Li, M.; Yang, B.; Fang, Y.; Jiang, X.; Veith, G. M.; Sun, X. G.; Dai, S. *Adv. Mater.* **2015**, 27, (48), 8088-8094.
17. Barsoukov, E.; Macdonald, J. R., *Impedance spectroscopy: theory, experiment, and applications*. John Wiley & Sons: 2005.
18. Bard, A. J.; Faulkner, L. R.; Leddy, J.; Zoski, C. G., *Electrochemical methods: fundamentals and applications*. Wiley New York: 1980; Vol. 2.
19. Mabbott, G. A. *J. Chem. Educ* **1983**, 60, (9), 697.
20. Xu, K. *Chem. Rev.* **2014**, 114, (23), 11503-11618.
21. Wang, X.; Liu, Z.; Kong, Q.; Jiang, W.; Yao, J.; Zhang, C.; Cui, G. *Solid State Ionics* **2014**, 262, 747-753.
22. Hallac, B.; Geiculescu, O.; Rajagopal, R.; Creager, S. E.; DesMarteau, D. *Electrochim. Acta* **2008**, 53, (20), 5985-5991.
23. Li, J.; Daniel, C.; Wood, D. *J. Power Sources* **2011**, 196, (5), 2452-2460.
24. Verma, P.; Maire, P.; Novák, P. *Electrochim. Acta* **2010**, 55, (22), 6332-6341.
25. Xue, Z.; He, D.; Xie, X. *J. Mater. Chem. A* **2015**, 3, (38), 19218-19253.
26. Jacoby, M. *Chem. Eng. News* **2013**, 91, 33-37.
27. Meyer, W. H. *Adv. Mater.* **1998**, 10, (6), 439-448.
28. Xue, Z.; He, D.; Xie, X. *J. Mater. Chem. A* **2015**.
29. Sirisoponaporn, C.; Fericola, A.; Scrosati, B. *J. Power Sources* **2009**, 186, (2), 490-495.
30. Osada, I.; de Vries, H.; Scrosati, B.; Passerini, S. *Angew. Chem. Int. Ed.* **2015**.
31. Newman, G.; Francis, R.; Gaines, L.; Rao, B. *J. Electrochem. Soc* **1980**, 127, (9), 2025-2027.

32. Jow, T. R.; Xu, K.; Borodin, O.; Makoto, U., *Electrolytes for lithium and lithium-ion batteries*. Springer: 2014; Vol. 58.
33. Sloop, S. E.; Pugh, J. K.; Wang, S.; Kerr, J.; Kinoshita, K. *Electrochemical and Solid-State Letters* **2001**, 4, (4), A42-A44.
34. Hammami, A.; Raymond, N.; Armand, M. *Nature* **2003**, 424, (6949), 635-636.
35. Ensling, D.; Stjern Dahl, M.; Nyttén, A.; Gustafsson, T.; Thomas, J. O. *Journal of Materials Chemistry* **2009**, 19, (1), 82-88.
36. Webber, A. *J. Electrochem. Soc* **1991**, 138, (9), 2586-2590.
37. Andreev, Y.; Lightfoot, P.; Bruce, P. *Chemical Communications* **1996**, (18), 2169-2170.
38. Croce, F.; Appetecchi, G.; Persi, L.; Scrosati, B. *Nature* **1998**, 394, (6692), 456-458.
39. Fenton, D.; Parker, J.; Wright, P. *Polymer* **1973**, 14, (11), 589.
40. Bouchet, R.; Maria, S.; Meziane, R.; Aboulaich, A.; Lienafa, L.; Bonnet, J.-P.; Phan, T. N.; Bertin, D.; Gimes, D.; Devaux, D. *Nat. Mater.* **2013**, 12, (5), 452-457.
41. Shim, J.; Kim, D.-G.; Kim, H. J.; Lee, J. H.; Lee, J.-C. *ACS Appl. Mater. Interfaces* **2015**, 7, (14), 7690-7701.
42. Lu, Q.; Yang, J.; Lu, W.; Wang, J.; Nuli, Y. *Electrochim. Acta* **2015**, 152, 489-495.
43. Zhang, H.; Kulkarni, S.; Wunder, S. L. *The Journal of Physical Chemistry B* **2007**, 111, (14), 3583-3590.
44. Miranda, D. F.; Versek, C.; Tuominen, M. T.; Russell, T. P.; Watkins, J. J. *Macromolecules* **2013**, 46, (23), 9313-9323.
45. Idris, N. H.; Rahman, M. M.; Wang, J.-Z.; Liu, H.-K. *J. Power Sources* **2012**, 201, 294-300.
46. Villaluenga, I.; Chen, X. C.; Devaux, D.; Hallinan, D. T.; Balsara, N. P. *Macromolecules* **2015**, 48, (2), 358-364.
47. Shin, W.-K.; Yoo, J. H.; Choi, W.; Chung, K. Y.; Jang, S. S.; Kim, D.-W. *J. Mater. Chem. A* **2015**, 3, (23), 12163-12170.
48. Zhang, S. S. *J. Power Sources* **2007**, 164, (1), 351-364.
49. Kalhoff, J.; Eshetu, G. G.; Bresser, D.; Passerini, S. *ChemSusChem* **2015**, 8, (13), 2154-2175.
50. Sequeira, C.; Santos, D., *Polymer electrolytes: fundamentals and applications*. Elsevier: 2010.
51. Song, J.; Wang, Y.; Wan, C. *J. Power Sources* **1999**, 77, (2), 183-197.
52. Zhang, Y.; Lim, C. A.; Cai, W.; Rohan, R.; Xu, G.; Sun, Y.; Cheng, H. *RSC Advances* **2014**, 4, (83), 43857-43864.
53. Wang, S.-H.; Hou, S.-S.; Kuo, P.-L.; Teng, H. *ACS Appl. Mater. Interfaces* **2013**, 5, (17), 8477-8485.
54. Isken, P.; Winter, M.; Passerini, S.; Lex-Balducci, A. *J. Power Sources* **2013**, 225, 157-162.
55. Saikia, D.; Wu, H.-Y.; Pan, Y.-C.; Lin, C.-P.; Huang, K.-P.; Chen, K.-N.; Fey, G. T.; Kao, H.-M. *J. Power Sources* **2011**, 196, (5), 2826-2834.
56. Zhu, Y.; Xiao, S.; Shi, Y.; Yang, Y.; Wu, Y. *J. Mater. Chem. A* **2013**, 1, (26), 7790-7797.
57. Zhang, J.; Sun, B.; Huang, X.; Chen, S.; Wang, G. *Scientific reports* **2014**, 4.
58. Tu, Z.; Lu, Y.; Archer, L. *Small* **2015**, 11, (22), 2631-2635.
59. Stephan, A. M.; Nahm, K. *Polymer* **2006**, 47, (16), 5952-5964.
60. Choi, J.-H.; Lee, C.-H.; Yu, J.-H.; Doh, C.-H.; Lee, S.-M. *J. Power Sources* **2015**, 274, 458-463.
61. Lim, Y. J.; Kim, H. W.; Lee, S. S.; Kim, H. J.; Kim, J. K.; Jung, Y. G.; Kim, Y. *ChemPlusChem* **2015**, 80, (7), 1100-1103.

62. Ferrari, S.; Quartarone, E.; Mustarelli, P.; Magistris, A.; Fagnoni, M.; Protti, S.; Gerbaldi, C.; Spinella, A. *J. Power Sources* **2010**, 195, (2), 559-566.
63. Thangadurai, V.; Narayanan, S.; Pinzaru, D. *Chem. Soc. Rev.* **2014**, 43, (13), 4714-4727.
64. Zhang, P.; Yang, L.; Li, L.; Ding, M.; Wu, Y.; Holze, R. *Journal of membrane science* **2011**, 379, (1), 80-85.
65. Liu, W.; Liu, N.; Sun, J.; Hsu, P.-C.; Li, Y.; Lee, H.-W.; Cui, Y. *Nano Lett.* **2015**, 15, (4), 2740-2745.
66. Fu, K. K.; Gong, Y.; Dai, J.; Gong, A.; Han, X.; Yao, Y.; Wang, C.; Wang, Y.; Chen, Y.; Yan, C. *Proc. Natl. Acad. Sci. USA* **2016**, 113, (26), 7094-7099.
67. Rojas, A. A.; Inceoglu, S.; Mackay, N. G.; Thelen, J. L.; Devaux, D.; Stone, G. M.; Balsara, N. P. *Macromolecules* **2015**, 48, (18), 6589-6595.
68. Sun, X.-G.; Hou, J.; Kerr, J. B. *Electrochim. Acta* **2005**, 50, (5), 1139-1147.
69. Zhu, Y.; Gao, X.; Wang, X.; Hou, Y.; Liu, L.; Wu, Y. *Electrochemistry Communications* **2012**, 22, 29-32.
70. Doyle, R. P.; Chen, X.; Macrae, M.; Srungavarapu, A.; Smith, L. J.; Gopinadhan, M.; Osuji, C. O.; Granados-Focil, S. *Macromolecules* **2014**, 47, (10), 3401-3408.
71. Zhang, Y.; Rohan, R.; Cai, W.; Xu, G.; Sun, Y.; Lin, A.; Cheng, H. *ACS Appl. Mater. Interfaces* **2014**, 6, (20), 17534-17542.
72. Oh, H.; Xu, K.; Yoo, H. D.; Kim, D. S.; Chanthad, C.; Yang, G.; Jin, J.; Ayhan, I. A.; Oh, S. M.; Wang, Q. *Chem. Mater.* **2015**, 28, (1), 188-196.
73. Meziane, R.; Bonnet, J.-P.; Courty, M.; Djellab, K.; Armand, M. *Electrochim. Acta* **2011**, 57, 14-19.
74. Feng, S.; Shi, D.; Liu, F.; Zheng, L.; Nie, J.; Feng, W.; Huang, X.; Armand, M.; Zhou, Z. *Electrochim. Acta* **2013**, 93, 254-263.
75. Inceoglu, S.; Rojas, A. A.; Devaux, D.; Chen, X. C.; Stone, G. M.; Balsara, N. P. *ACS Macro Letters* **2014**, 3, (6), 510-514.
76. Lu, Y.; Tikekar, M.; Mohanty, R.; Hendrickson, K.; Ma, L.; Archer, L. A. *Adv. Energy Mater.* **2015**, 5, (9).
77. Arbizzani, C.; Gabrielli, G.; Mastragostino, M. *J. Power Sources* **2011**, 196, (10), 4801-4805.
78. Qin, B.; Liu, Z.; Zheng, J.; Hu, P.; Ding, G.; Zhang, C.; Zhao, J.; Kong, D.; Cui, G. *J. Mater. Chem. A* **2015**, 3, (15), 7773-7779.
79. Zhu, Y.; Wang, X.; Hou, Y.; Gao, X.; Liu, L.; Wu, Y.; Shimizu, M. *Electrochim. Acta* **2013**, 87, 113-118.
80. Evans, J.; Vincent, C. A.; Bruce, P. G. *Polymer* **1987**, 28, (13), 2324-2328.
81. Wang, Y.; Li, B.; Ji, J.; Eyer, A.; Zhong, W. H. *Adv. Energy Mater.* **2013**, 3, (12), 1557-1562.
82. Daigle, J.-C.; Vijn, A.; Hovington, P.; Gagnon, C.; Hamel-Pâquet, J.; Verreault, S.; Turcotte, N.; Clément, D.; Guerfi, A.; Zaghbi, K. *J. Power Sources* **2015**, 279, 372-383.
83. Muldoon, J.; Bucur, C. B.; Boaretto, N.; Gregory, T.; Di Noto, V. *Polymer Reviews* **2015**, 55, (2), 208-246.
84. Shim, J.; Bae, K. Y.; Kim, H. J.; Lee, J. H.; Kim, D. G.; Yoon, W. Y.; Lee, J. C. *ChemSusChem* **2015**, 8, (24), 4133-4138.
85. He, D.; Kim, D. W.; Park, J. S.; Cho, S. Y.; Kang, Y. *J. Power Sources* **2013**, 244, 170-176.
86. Zhang, D.; Yan, H.; Zhu, Z.; Zhang, H.; Wang, J. *J. Power Sources* **2011**, 196, (23), 10120-10125.
87. Hu, Q.; Osswald, S.; Daniel, R.; Zhu, Y.; Wesel, S.; Ortiz, L.; Sadoway, D. R. *J. Power Sources* **2011**, 196, (13), 5604-5610.

88. Lago, N.; Garcia - Calvo, O.; Lopez del Amo, J. M.; Rojo, T.; Armand, M. *ChemSusChem* **2015**, 8, (18), 3039-3043.
89. Devaux, D.; Glé, D.; Phan, T. N.; Gignes, D.; Giroud, E.; Deschamps, M.; Denoyel, R.; Bouchet, R. *Chem. Mater.* **2015**, 27, (13), 4682-4692.
90. Singh, M.; Odusanya, O.; Wilmes, G. M.; Eitouni, H. B.; Gomez, E. D.; Patel, A. J.; Chen, V. L.; Park, M. J.; Fragouli, P.; Iatrou, H. *Macromolecules* **2007**, 40, (13), 4578-4585.
91. Bouchet, R.; Phan, T.; Beaudoin, E.; Devaux, D.; Davidson, P.; Bertin, D.; Denoyel, R. *Macromolecules* **2014**, 47, (8), 2659-2665.
92. Kaneko, F.; Wada, S.; Nakayama, M.; Wakihara, M.; Koki, J.; Kuroki, S. *Adv. Funct. Mater.* **2009**, 19, (6), 918-925.
93. Kim, D.-G.; Shim, J.; Lee, J. H.; Kwon, S.-J.; Baik, J.-H.; Lee, J.-C. *Polymer* **2013**, 54, (21), 5812-5820.
94. Chinnam, P. R.; Wunder, S. L. *Chemistry of Materials* **2011**, 23, (23), 5111-5121.
95. Pan, Q.; Smith, D. M.; Qi, H.; Wang, S.; Li, C. Y. *Adv. Mater.* **2015**, 27, (39), 5995-6001.
96. Brissot, C.; Rosso, M.; Chazalviel, J.-N.; Lascaud, S. *J. Power Sources* **1999**, 81, 925-929.
97. Monroe, C.; Newman, J. *J. Electrochem. Soc* **2005**, 152, (2), A396-A404.
98. Tanaka, K.; Ishiguro, F.; Chujo, Y. *J. Am. Chem. Soc.* **2010**, 132, (50), 17649-17651.
99. Kim, S.-K.; Kim, D.-G.; Lee, A.; Sohn, H.-S.; Wie, J. J.; Nguyen, N. A.; Mackay, M. E.; Lee, J.-C. *Macromolecules* **2012**, 45, (23), 9347-9356.
100. Maitra, P.; Wunder, S. L. *Electrochemical and solid-state letters* **2004**, 7, (4), A88-A92.
101. Chinnam, P. R.; Zhang, H.; Wunder, S. L. *Electrochim. Acta* **2015**, 170, 191-201.
102. Zhang, H.; Kulkarni, S.; Wunder, S. L. *J. Electrochem. Soc* **2006**, 153, (2), A239-A248.
103. Maitra, P.; Wunder, S. L. *Chem. Mater.* **2002**, 14, (11), 4494-4497.
104. Choi, K. H.; Cho, S. J.; Kim, S. H.; Kwon, Y. H.; Kim, J. Y.; Lee, S. Y. *Advanced Functional Materials* **2014**, 24, (1), 44-52.
105. Villaluenga, I.; Wujcik, K. H.; Tong, W.; Devaux, D.; Wong, D. H.; DeSimone, J. M.; Balsara, N. P. *Proc. Natl. Acad. Sci. USA* **2016**, 113, (1), 52-57.
106. Wong, D. H.; Thelen, J. L.; Fu, Y.; Devaux, D.; Pandya, A. A.; Battaglia, V. S.; Balsara, N. P.; DeSimone, J. M. *Proc. Natl. Acad. Sci. USA* **2014**, 111, (9), 3327-3331.
107. Zhang, J.; Zhao, J.; Yue, L.; Wang, Q.; Chai, J.; Liu, Z.; Zhou, X.; Li, H.; Guo, Y.; Cui, G. *Adv. Energy Mater.* **2015**, 5, (24).
108. Zhang, J.; Zhao, J.; Yue, L.; Wang, Q.; Chai, J.; Liu, Z.; Zhou, X.; Li, H.; Guo, Y.; Cui, G. *Adv. Energy Mater.* **2015**.
109. Fan, L. Z.; Hu, Y. S.; Bhattacharyya, A. J.; Maier, J. *Adv. Funct. Mater.* **2007**, 17, (15), 2800-2807.
110. Zhou, D.; He, Y. B.; Liu, R.; Liu, M.; Du, H.; Li, B.; Cai, Q.; Yang, Q. H.; Kang, F. *Adv. Energy Mater.* **2015**, 5, (15).
111. Ye, Y.-S.; Rick, J.; Hwang, B.-J. *J. Mater. Chem. A* **2013**, 1, (8), 2719-2743.
112. Le Bideau, J.; Viau, L.; Vioux, A. *Chem. Soc. Rev.* **2011**, 40, (2), 907-925.
113. Armand, M.; Endres, F.; MacFarlane, D. R.; Ohno, H.; Scrosati, B. *Nat. Mater.* **2009**, 8, (8), 621-629.
114. Kim, G.-T.; Appetecchi, G. B.; Carewska, M.; Joost, M.; Balducci, A.; Winter, M.; Passerini, S. *J. Power Sources* **2010**, 195, (18), 6130-6137.
115. Zhu, C.; Cheng, H.; Yang, Y. *J. Electrochem. Soc* **2008**, 155, (8), A569-A575.
116. Lewandowski, A.; Świdarska-Mocek, A. *J. Power Sources* **2009**, 194, (2), 601-609.
117. Pitawala, J.; Navarra, M. A.; Scrosati, B.; Jacobsson, P.; Matic, A. *J. Power Sources* **2014**, 245, 830-835.

118. Kim, G.-T.; Jeong, S.; Xue, M.-Z.; Balducci, A.; Winter, M.; Passerini, S.; Alessandrini, F.; Appetecchi, G. *J. Power Sources* **2012**, 199, 239-246.
119. Kim, G.-T.; Appetecchi, G. B.; Alessandrini, F.; Passerini, S. *J. Power Sources* **2007**, 171, (2), 861-869.
120. Sutto, T. E. *J. Electrochem. Soc* **2007**, 154, (10), P101-P107.
121. Shin, J.-H.; Henderson, W. A.; Scaccia, S.; Prosini, P. P.; Passerini, S. *J. Power Sources* **2006**, 156, (2), 560-566.
122. Navarra, M.; Manzi, J.; Lombardo, L.; Panero, S.; Scrosati, B. *ChemSusChem* **2011**, 4, (1), 125-130.
123. Kumar, Y.; Hashmi, S.; Pandey, G. *Solid State Ionics* **2011**, 201, (1), 73-80.
124. Nair, J. R.; Porcarelli, L.; Bella, F.; Gerbaldi, C. *ACS Appl. Mater. Interfaces* **2015**, 7, (23), 12961-12971.
125. Yuan, J.; Mecerreyes, D.; Antonietti, M. *Prog. Polym. Sci.* **2013**, 38, (7), 1009-1036.
126. Zhang, P.; Li, M.; Yang, B.; Fang, Y.; Jiang, X.; Veith, G. M.; Sun, X. G.; Dai, S. *Adv. Mater.* **2015**.
127. Li, M.; Wang, L.; Yang, B.; Du, T.; Zhang, Y. *Electrochim. Acta* **2014**, 123, 296-302.
128. Meek, K. M.; Sharick, S.; Ye, Y.; Winey, K. I.; Elabd, Y. A. *Macromolecules* **2015**, 48, (14), 4850-4862.
129. Sato, T.; Morinaga, T.; Marukane, S.; Narutomi, T.; Igarashi, T.; Kawano, Y.; Ohno, K.; Fukuda, T.; Tsujii, Y. *Adv. Mater.* **2011**, 23, (42), 4868-4872.
130. Li, X.; Zhang, Z.; Li, S.; Yang, L.; Hirano, S.-i. *J. Power Sources* **2016**, 307, 678-683.
131. Porcarelli, L.; Shaplov, A. S.; Salsamendi, M.; Nair, J. R.; Vygodskii, Y. S.; Mecerreyes, D.; Gerbaldi, C. *ACS Appl. Mater. Interfaces* **2016**, 8, (16), 10350-10359.
132. Yin, K.; Zhang, Z.; Li, X.; Yang, L.; Tachibana, K.; Hirano, S.-i. *J. Mater. Chem. A* **2015**, 3, (1), 170-178.
133. Ye, Y.; Elabd, Y. A. *Polymer* **2011**, 52, (5), 1309-1317.
134. Ohno, H.; Yoshizawa, M.; Ogihara, W. *Electrochim. Acta* **2004**, 50, (2), 255-261.
135. Xiao, S.; Lu, X.; Lu, Q. *Macromolecules* **2007**, 40, (22), 7944-7950.
136. Lee, M.; Choi, U. H.; Colby, R. H.; Gibson, H. W. *Chem. Mater.* **2010**, 22, (21), 5814-5822.
137. Mecerreyes, D. *Prog. Polym. Sci.* **2011**, 36, (12), 1629-1648.
138. Osada, I.; de Vries, H.; Scrosati, B.; Passerini, S. *Angew. Chem. Int. Ed.* **2016**, 55, (2), 500-513.
139. Stepniak, I. *J. Power Sources* **2014**, 247, 112-116.
140. Yin, K.; Zhang, Z.; Yang, L.; Hirano, S.-i. *J. Power Sources* **2014**, 258, 150-154.
141. Etacheri, V.; Marom, R.; Elazari, R.; Salitra, G.; Aurbach, D. *Energy Environ. Sci.* **2011**, 4, (9), 3243-3262.
142. Quartarone, E.; Mustarelli, P. *Chem. Soc. Rev.* **2011**, 40, (5), 2525-2540.
143. Devaux, D.; Bouchet, R.; Glé, D.; Denoyel, R. *Solid State Ionics* **2012**, 227, 119-127.
144. Stephan, A. M. *Eur. Polym. J* **2006**, 42, (1), 21-42.
145. MacFarlane, D. R.; Tachikawa, N.; Forsyth, M.; Pringle, J. M.; Howlett, P. C.; Elliott, G. D.; Davis, J. H.; Watanabe, M.; Simon, P.; Angell, C. A. *Energy Environ. Sci.* **2014**, 7, (1), 232-250.
146. Choi, J.-H.; Ye, Y.; Elabd, Y. A.; Winey, K. I. *Macromolecules* **2013**, 46, (13), 5290-5300.
147. Matsumi, N.; Sugai, K.; Miyake, M.; Ohno, H. *Macromolecules* **2006**, 39, (20), 6924-6927.
148. Lu, Y.; Das, S. K.; Moganty, S. S.; Archer, L. A. *Adv. Mater.* **2012**, 24, (32), 4430-4435.

149. Li, Z.; Xia, Q.; Liu, L.; Lei, G.; Xiao, Q.; Gao, D.; Zhou, X. *Electrochim. Acta* **2010**, *56*, (2), 804-809.
150. Kimura, K.; Matsumoto, H.; Hassoun, J.; Panero, S.; Scrosati, B.; Tominaga, Y. *Electrochim. Acta* **2015**.
151. Kim, J.-K.; Matic, A.; Ahn, J.-H.; Jacobsson, P. *J. Power Sources* **2010**, *195*, (22), 7639-7643.
152. Green, M. D.; Long, T. E. *Polymer Reviews* **2009**, *49*, (4), 291-314.
153. Zhang, H.; Liu, C.; Zheng, L.; Feng, W.; Zhou, Z.; Nie, J. *Electrochim. Acta* **2015**, *159*, 93-101.
154. Fisher, A. S.; Khalid, M. B.; Widstrom, M.; Kofinas, P. *J. Power Sources* **2011**, *196*, (22), 9767-9773.
155. Cheng, S.; Zhang, M.; Wu, T.; Hemp, S. T.; Mather, B. D.; Moore, R. B.; Long, T. E. *Journal of Polymer Science Part A: Polymer Chemistry* **2012**, *50*, (1), 166-173.
156. Kolbeck, C.; Killian, M.; Maier, F.; Paape, N.; Wasserscheid, P.; Steinrück, H.-P. *Langmuir* **2008**, *24*, (17), 9500-9507.
157. Nugent, J. L.; Moganty, S. S.; Archer, L. A. *Adv. Mater.* **2010**, *22*, (33), 3677-+.
158. Agarwal, P.; Qi, H. B.; Archer, L. A. *Nano Lett.* **2010**, *10*, (1), 111-115.
159. Young, N. P.; Devaux, D.; Khurana, R.; Coates, G. W.; Balsara, N. P. *Solid State Ionics* **2014**, *263*, 87-94.
160. Duluard, S.; Grondin, J.; Bruneel, J. L.; Pianet, I.; Grélard, A.; Campet, G.; Delville, M. H.; Lassègues, J. C. *J. Raman Spectrosc.* **2008**, *39*, (5), 627-632.
161. Chaurasia, S.; Saroj, A.; Shalu, Singh, V.; Tripathi, A.; Gupta, A.; Verma, Y.; Singh, R. *AIP Advances* **2015**, *5*, (7), 077178.
162. Ibrahim, S.; Yassin, M. M.; Ahmad, R.; Johan, M. R. *Ionics* **2011**, *17*, (5), 399-405.
163. Fang, S.; Yang, L.; Wang, J.; Zhang, H.; Tachibana, K.; Kamijima, K. *J. Power Sources* **2009**, *191*, (2), 619-622.
164. Scrosati, B. *Electrochim. Acta* **2000**, *45*, (15), 2461-2466.
165. Pan, Q.; Zhang, W.; Pan, M.; Zhang, B.; Zeng, D.; Sun, Y.; Cheng, H. *J. Power Sources* **2015**, *283*, 279-288.
166. Zhou, D.; He, Y.-B.; Liu, R.; Liu, M.; Du, H.; Li, B.; Cai, Q.; Yang, Q.-H.; Kang, F. *Adv. Energy Mater.* **2015**, *5*, (15), n/a-n/a.
167. Pan, Q.; Smith, D. M.; Qi, H.; Wang, S.; Li, C. Y. *Advanced Materials* **2015**.
168. Cai, W.; Zhang, Y.; Li, J.; Sun, Y.; Cheng, H. *ChemSusChem* **2014**, *7*, (4), 1063-1067.
169. Rohan, R.; Pareek, K.; Cai, W.; Zhang, Y.; Xu, G.; Chen, Z.; Gao, Z.; Dan, Z.; Cheng, H. *J. Mater. Chem. A* **2015**, *3*, (9), 5132-5139.
170. Zhu, Z.; Hong, M.; Guo, D.; Shi, J.; Tao, Z.; Chen, J. *J. Am. Chem. Soc.* **2014**, *136*, (47), 16461-16464.
171. Barteau, K. P.; Wolffs, M.; Lynd, N. A.; Fredrickson, G. H.; Kramer, E. J.; Hawker, C. J. *Macromolecules* **2013**, *46*, (22), 8988-8994.
172. Saikia, D.; Chen, Y.-H.; Pan, Y.-C.; Fang, J.; Tsai, L.-D.; Fey, G. T.; Kao, H.-M. *Journal of Materials Chemistry* **2011**, *21*, (28), 10542-10551.
173. Mindemark, J.; Sun, B.; Törmä, E.; Brandell, D. **2015**.
174. Shim, J.; Kim, D.-G.; Kim, H. J.; Lee, J. H.; Baik, J.-H.; Lee, J.-C. *J. Mater. Chem. A* **2014**, *2*, (34), 13873-13883.
175. Manthiram, A.; Yu, X.; Wang, S. *Nature Reviews Materials* **2017**, *2*, 16103.
176. Lu, Y.; Tu, Z.; Archer, L. A. *Nat. Mater.* **2014**, *13*, (10), 961-969.
177. Wright, P. V. *Polymer International* **1975**, *7*, (5), 319-327.
178. Armand, M.; Chabagno, J. In *Duclot, Extended Abstract*, Second International Conference on Solid Electrolytes, St. Andrews, Scotland, 1978; 1978.

179. Wang, Q.; Song, W.-L.; Fan, L.-Z.; Song, Y. *Journal of Membrane Science* **2015**, 486, 21-28.
180. Porcarelli, L.; Gerbaldi, C.; Bella, F.; Nair, J. R. *Scientific reports* **2016**, 6.
181. Zhou, W.; Wang, S.; Li, Y.; Xin, S.; Manthiram, A.; Goodenough, J. B. *J. Am. Chem. Soc.* **2016**, 138, (30), 9385-9388.
182. Green, M. D.; Choi, J.-H.; Winey, K. I.; Long, T. E. *Macromolecules* **2012**, 45, (11), 4749-4757.
183. Weber, R. L.; Ye, Y.; Schmitt, A. L.; Banik, S. M.; Elabd, Y. A.; Mahanthappa, M. K. *Macromolecules* **2011**, 44, (14), 5727-5735.
184. Kuo, S.-W.; Chang, F.-C. *Prog. Polym. Sci.* **2011**, 36, (12), 1649-1696.
185. Yang, G.; Chanthad, C.; Oh, H.; Ayhan, I. A.; Wang, Q. *J. Mater. Chem. A* **2017**.
186. Feher, F.; Wyndham, K.; Baldwin, R.; Ziller, J.; Lichtenhan, J. *Chemical Communications* **1999**, (14), 1289-1290.
187. Kuo, P.-L.; Tsao, C.-H.; Hsu, C.-H.; Chen, S.-T.; Hsu, H.-M. *Journal of Membrane Science* **2016**, 499, 462-469.
188. Li, M.; Yang, B.; Wang, L.; Zhang, Y.; Zhang, Z.; Fang, S.; Zhang, Z. *Journal of membrane science* **2013**, 447, 222-227.
189. Rohan, R.; Sun, Y.; Cai, W.; Pareek, K.; Zhang, Y.; Xu, G.; Cheng, H. *J. Mater. Chem. A* **2014**, 2, (9), 2960-2967.
190. Yang, X.; Zhong, Z.; Huang, Y. *International journal of pharmaceutics* **2016**, 508, (1), 51-60.
191. Beyler, C. L.; Hirschler, M. M. *SFPE handbook of fire protection engineering* **2002**, 2, 32.
192. Markovic, E.; Ginic-Markovic, M.; Clarke, S.; Matisons, J.; Hussain, M.; Simon, G. P. *Macromolecules* **2007**, 40, (8), 2694-2701.
193. Zeng, X.-X.; Yin, Y.-X.; Li, N.-W.; Du, W.-C.; Guo, Y.-G.; Wan, L.-J. *J. Am. Chem. Soc.* **2016**, 138, (49), 15825-15828.
194. Lu, Y.; Moganty, S. S.; Schaefer, J. L.; Archer, L. A. *Journal of Materials Chemistry* **2012**, 22, (9), 4066-4072.
195. Abraham, K.; Jiang, Z.; Carroll, B. *Chem. Mater.* **1997**, 9, (9), 1978-1988.
196. Agostini, M.; Rizzi, L. G.; Cesareo, G.; Russo, V.; Hassoun, J. *Advanced Materials Interfaces* **2015**, 2, (8).
197. Balo, L.; Gupta, H.; Singh, V. K.; Singh, R. K. *Electrochim. Acta* **2017**, 230, 123-131.
198. Shin, J.-H.; Henderson, W. A.; Passerini, S. *J. Electrochem. Soc.* **2005**, 152, (5), A978-A983.
199. Yun, Y. S.; Kim, J. H.; Lee, S.-Y.; Shim, E.-G.; Kim, D.-W. *J. Power Sources* **2011**, 196, (16), 6750-6755.
200. Zhang, H.; Han, H.; Cheng, X.; Zheng, L.; Cheng, P.; Feng, W.; Nie, J.; Armand, M.; Huang, X.; Zhou, Z. *J. Power Sources* **2015**, 296, 142-149.
201. Rolland, J.; Brassinne, J.; Bourgeois, J.-P.; Poggi, E.; Vlad, A.; Gohy, J.-F. *J. Mater. Chem. A* **2014**, 2, (30), 11839-11846.
202. Daigle, J.-C.; Asakawa, Y.; Vijn, A.; Hovington, P.; Armand, M.; Zaghib, K. *J. Power Sources* **2016**, 332, 213-221.
203. Leng, Y.; Ge, S.; Marple, D.; Yang, X.-G.; Bauer, C.; Lamp, P.; Wang, C.-Y. *J. Electrochem. Soc.* **2017**, 164, (6), A1037-A1049.
204. Wu, F.; Chen, N.; Chen, R.; Zhu, Q.; Qian, J.; Li, L. *Chem. Mater.* **2016**, 28, (3), 848-856.
205. Hu, J.; Wang, W.; Peng, H.; Guo, M.; Feng, Y.; Xue, Z.; Ye, Y.; Xie, X. *Macromolecules* **2017**, 50, (5), 1970-1980.

206. Mindemark, J.; Sun, B.; Törmä, E.; Brandell, D. *J. Power Sources* **2015**, 298, 166-170.
207. Tan, R.; Gao, R.; Zhao, Y.; Zhang, M.; Xu, J.; Yang, J.; Pan, F. *ACS Appl. Mater. Interfaces* **2016**, 8, (45), 31273-31280.
208. Cheng, X.-B.; Zhang, R.; Zhao, C.-Z.; Zhang, Q. *Chem. Rev.* **2017**, 117, (15), 10403-10473.
209. Wee, A. *World* **2016**.
210. Zhao, C.-Z.; Zhang, X.-Q.; Cheng, X.-B.; Zhang, R.; Xu, R.; Chen, P.-Y.; Peng, H.-J.; Huang, J.-Q.; Zhang, Q. *Proc. Natl. Acad. Sci. USA* **2017**, 114, (42), 11069-11074.
211. Sun, C.; Liu, J.; Gong, Y.; Wilkinson, D. P.; Zhang, J. *Nano Energy* **2017**.
212. Zheng, Q.; Ma, L.; Khurana, R.; Archer, L. A.; Coates, G. W. *Chemical Science* **2016**, 7, (11), 6832-6838.
213. Murata, K.; Izuchi, S.; Yoshihisa, Y. *Electrochim. Acta* **2000**, 45, (8), 1501-1508.
214. Siqueira, L. J.; Ribeiro, M. C. *Journal of Chemical Physics* **2005**, 122, (19), 4911.
215. Zhai, H.; Xu, P.; Ning, M.; Cheng, Q.; Mandal, J.; Yang, Y. *Nano Lett.* **2017**, 17, (5), 3182-3187.
216. Yuan, J.; Antonietti, M. *Polymer* **2011**, 52, (7), 1469-1482.
217. Bonhote, P.; Dias, A.-P.; Papageorgiou, N.; Kalyanasundaram, K.; Grätzel, M. *Inorganic chemistry* **1996**, 35, (5), 1168-1178.
218. Zhou, D.; Liu, R.; Zhang, J.; Qi, X.; He, Y.-B.; Li, B.; Yang, Q.-H.; Hu, Y.-S.; Kang, F. *Nano Energy* **2017**, 33, 45-54.
219. Safa, M.; Chamaani, A.; Chawla, N.; El-Zahab, B. *Electrochim. Acta* **2016**, 213, 587-593.
220. McIntosh, L. D.; Kubo, T.; Lodge, T. P. *Macromolecules* **2014**, 47, (3), 1090-1098.
221. Wu, J.; Ge, Q.; Mather, P. T. *Macromolecules* **2010**, 43, (18), 7637-7649.
222. Lee, A. S. S.; Lee, J. H.; Lee, J.-C.; Hong, S. M.; Hwang, S. S.; Koo, C. M. *J. Mater. Chem. A* **2014**, 2, (5), 1277-1283.
223. Zhang, W.; Müller, A. H. *Prog. Polym. Sci.* **2013**, 38, (8), 1121-1162.
224. Fina, A.; Abbenhuis, H. C.; Tabuani, D.; Camino, G. *Polymer Degradation and Stability* **2006**, 91, (10), 2275-2281.
225. Glodek, T. E.; Boyd, S. E.; McAninch, I. M.; LaScala, J. J. *Composites science and technology* **2008**, 68, (14), 2994-3001.
226. Devaux, D.; Villaluenga, I.; Bhatt, M.; Shah, D.; Chen, X. C.; Thelen, J. L.; DeSimone, J. M.; Balsara, N. P. *Solid State Ionics* **2017**, 310, 71-80.
227. Kubota, K.; Matsumoto, H. *The Journal of Physical Chemistry C* **2013**, 117, (37), 18829-18836.
228. Hagiwara, R.; Ito, Y. *Journal of Fluorine Chemistry* **2000**, 105, (2), 221-227.
229. Costa, L. T.; Sun, B.; Jeschull, F.; Brandell, D. *The Journal of chemical physics* **2015**, 143, (2), 024904.
230. Seki, S.; Kobayashi, Y.; Miyashiro, H.; Ohno, Y.; Usami, A.; Mita, Y.; Kihira, N.; Watanabe, M.; Terada, N. *The Journal of Physical Chemistry B* **2006**, 110, (21), 10228-10230.
231. Nykaza, J. R.; Savage, A. M.; Pan, Q.; Wang, S.; Beyer, F. L.; Tang, M. H.; Li, C. Y.; Elabd, Y. A. *Polymer* **2016**, 101, 311-318.
232. Galiński, M.; Lewandowski, A.; Stepniak, I. *Electrochim. Acta* **2006**, 51, (26), 5567-5580.

VITA

Guang Yang

Guang Yang was born in Zunyi, Guizhou province, P.R. China in 1986. He obtained his Bachelor (2008) and Master (2011) degrees from Northwestern Polytechnical University, Xi'an, China. He was enrolled as a graduate student in department of material science and engineering at The Pennsylvania State University in 2011 Fall. His research project in Professor Qing Wang's research group is synthesis and characterization of polymer electrolyte for the next generation lithium ion battery. He authored or coauthored 15 publications in peer-reviewed journals.

Selected publications:

- **Yang, G.**, Chanthad, C., Hyukkeun, O., Wang, Q. Organic-Inorganic Hybrid Electrolytes from Ionic Liquid-Functionalized Octasilsesquioxane for Lithium Metal Batteries. *Journal of Materials Chemistry A*, 2017;5(34):18012-9
- **Yang, G.**, Oh, H., Chanthad, C., Wang, Q. Dumbell-Shaped Octasilsesquioxanes Functionalized with Ionic Liquids as Hybrid Electrolyte for Lithium Metal Batteries. *Chemistry of Materials* (2017, published on Oct.19)
- **Yang, G.**, Lee, Y.M., Wang, Q. Polymer electrolytes for lithium ion batteries. *Encyclopedia of Polymer Applications (EPA)*, Taylor & Francis. (book chapter, accepted, 2016)
- **Yang, G.**, Chanthad, C, Oh, H., Wang, Q. Hybrid polymer electrolyte containing ionic networks for lithium ion battery. (*in preparation*, 2017)